Geometry effect and scaling method for circulating fluidized riser

Document status and date:
Published: 24/05/2022

Document Version:
Publisher's PDF, also known as Version of Record (includes final page, issue and volume numbers)

Please check the document version of this publication:

• A submitted manuscript is the version of the article upon submission and before peer-review. There can be important differences between the submitted version and the official published version of record. People interested in the research are advised to contact the author for the final version of the publication, or visit the DOI to the publisher's website.
• The final author version and the galley proof are versions of the publication after peer review.
• The final published version features the final layout of the paper including the volume, issue and page numbers.

Link to publication

Download date: 04. Oct. 2023

GEOMETRY EFFECT AND SCALING METHOD FOR CIRCULATING FLUIDIZED RISER

Numerical Study with Discrete Element Method

Lijing Mu

Department of Chemical Engineering and Chemistry

Technische Universiteit Eindhoven

March 2022

PROEFSCHRIFT

ter verkrijging van de graad van doctor aan de
Technische Universiteit Eindhoven, op gezag van de
rector magnificus, prof.dr.ir. F.P.T. Baaijens, voor een
commissie aangewezen door het College voor
Promoties, in het openbaar te verdedigen
op dinsdag 24 mei 2022 om 13:30 uur

door

Lijing Mu

geboren te Shenzhou, China

Dit proefschrift is goedgekeurd door de promotoren en de samenstelling van de promotiecommissie is als volgt:

voorzitter:	prof.dr. F. Gallucci	
1^e promotor:	prof.dr.ir. J.A.M. Kuipers	
2^e promotor:	prof.dr.ir. N.G. Deen	
copromotor(en):	dr. ir. K.A. Buist	
leden:	prof.dr. J. Wang	Institute of Process Engineering, CAS
	prof.dr. S.R.A. Kersten	Universiteit Twente
	prof.dr. C.W.M. van der Geld	
	prof.dr.ir. M. van Sint Annaland	

Dit proefschrift is goedgekeurd door de promotor:

prof.dr.ir. J.A.M. Kuipers

2^e promotor:
prof.dr.ir. N.G. Deen
co-promotor:
dr. ir. K.A. Buist

Nederlandse titel: "Geometrie effect en schalingsmethode voor circulerende gefluidizeerde risers. — Numerieke studie met Discrete Elementen Methode."

Author email: lmu0025@gmail.com

For my parents

Table of contents

Summary

Gas-solid fluidized beds are used in numerous industrial chemical applications, such as drying, coating, granulation, combustion, polymerization and cracking. A lot of effort has been made to better understand the hydrodynamics, the heat transfer processes and impact of different geometries on the performance of fluidized bed reactors. To understand dense gas-solid flows in fluidized beds, the multiscale modeling approach offers a powerful concept that connects the transfer of mass, momentum and heat at various length scales. Computational Fluid Dynamics-Discrete Element Model (CFD-DEM) has been developed as an effective tool to reduce the amount of costly and time-consuming experiments and pilot trials. In this approach, the granular medium is treated as individual objects where relevant attributes of each particle are tracked during the simulation. This thesis focuses on modeling the hydrodynamics and heat transfer of dense gas-solid flows in fluidized bed reactors using CFD-DEM simulations.

The research reported in this thesis started with the development of a new heat transfer model, including a constant heat source term to mimic the heat liberation due to an exothermic chemical reaction. As a first step, the model was validated by comparing the simulation results with semi-analytical solutions from a one-dimensional model. The dimensionless axial temperature profiles of the gas and particle phase, with and without heat production, predicted by CFD-DEM simulations were in good agreement with the semi-analytical data. Subsequently a detailed comparative study of the hydrodynamic and heat transfer behavior has been performed for a pseudo-2D fluidized bed in the bubbling regime, considering the effect of the superficial velocity, different aspect ratios and the heat source term. In the second part of this thesis a circulating fluidized bed system was studied. Circulating fluidized beds consist of a riser, a downcomer, cyclone and a recycling pipe. First, the effect of different inlet and outlet geometries on the gas-solid flow characteristics were studied, including the impact on cluster phenomena prevailing in a pseudo-2D lab-scale circulating fluidized bed riser was. Two different configurations for the particle insertion were considered: a bottom inlet and a side inlet respectively. Secondly, two different outlet configurations were studied: a smooth lateral wall and a curved boundary consisting of fixed particles. To demonstrate

Summary

the reliability of the model to predict the hydrodynamics and cluster characteristics inside risers, the CFD-DEM simulations were successfully compared with experimental data (Varas et al., 2017). This study provided insight regarding the influence of different geometries on riser hydrodynamics. As expected, the inlet configurations have more influence on the flow pattern in the bottom and middle part rather than the exit part of the riser.

In CFD-DEM simulations, an accurate description of the particle-fluid interactions, particle-particle and particle-wall collisions is crucial and are handled in a deterministic manner. Hence, the calculation of the collisions between particles is expensive in terms of calculation time. In this work, a scaling method was developed to speed up the simulation while maintaining the accuracy and efficiency of CFD-DEM simulations. In this model, the equations of motion and the collisional behavior of the particles have been scaled using the following parameters: d, μ, g, k_n, k_t, γ_n, γ_t, while maintaining invariant bed hydrodynamics. A detailed simulation study has been performed for a pseudo-2D gas-solid circulating fluidized bed riser to test the applicability of the adopted scaling method. In addition to the scaling of the hydrodynamic forces an appropriate scaling of the grid is necessary. The effect of the ratio of volume of the computational grid cell to the particle volume and the ratio of the shallow depth of the riser and the particle diameter was quantified as well. A comparison has been made with experimental results reported in literature (Varas et al., 2017), to test the reliability of the new scaling method. The time-averaged solids volume fraction, the velocity distribution and mass flux profiles as well as the cluster phenomena inside the riser were all investigated to demonstrate the correctness of the proposed scaling model.

Finally, a binary system consisting of two types of particles was investigated to fully verify the performance of the new scaling method. The simulation results were compared with experimental data (Mathiesen et al., 2000). It was shown that the scaling method could well capture the hydrodynamics and cluster phenomena of binary systems in a CFB riser.

Nomenclature

Variables

C_p	heat capacity, [J/kg/K]
d	diameter, [m]
e	restitution coefficient, [-]
g	gravitational acceleration constant, [m/s^2]
h	effective interfacial heat transfer coefficient, [W/m/K]
I_p	moment of inertia, [kg $\cdot$ m^2]
k	fluid thermal conductivity, [W/m/K]
k	spring stiffness, [N/m]
m	mass, [kg]
N	number, [-]
Nu	nusselt number, [-]
Pa	pressure, [Pa]
Pr	prandtl number, [-]
q	heat production, [W]
Q	source term for the interphase heat transfer exchange, [W/m^3]
$\mathbf{r}$	position vector, [m]
Re	reynolds number, [-]
$\mathbf{S}_p$	momentum source term, [N/m^3]
t	time, [s]
T	temperature, [K]
$\mathbf{u}_g$	fluid velocity vector, [m/s]
V	volume, [m^3]
$\mathbf{v}_p$	particle velocity vector, [m/s]

Greek symbols

β	drag coefficient, $[\mathrm{kg}/(\mathrm{m}^3 \cdot s)]$	
γ	damping coefficient, [-]	
Δx	width of grid cell, [m]	
Δy	depth of grid cell, [m]	
Δz	height of grid cell, [m]	
ε	gas volume fraction, [-]	
μ	dynamic friction coefficient, [-]	
μ_g	gas phase shear viscosity, $[\mathrm{kg}/(\mathrm{m} \cdot \mathrm{s})]$	
ρ	density, $[\mathrm{kg}/\mathrm{m}^3]$	
σ	standard deviation of particle temperature, [K]	
τ	stress tensor, [Pa]	
Φ	solids volume fraction, [-]	
ω	angular velocity, [1/s]	

Subscripts

cell	computational grid cell	
f	fluid phase	
g	gas phase	
n	normal	
p	particle phase	
s	solids phase	
t	tangential	

Chapter 1

General Introduction

1.1   Gas-solid fluidized beds

Fluidized beds are often applied in industrial unit operations to process large amounts of granular materials. Fluidization is a process where a fluid entering from the bottom of the bed lifts the granular material which attains a fluid-like nature. The fluid can be liquid or gas. When gas is the process fluid it is known as gas-solid fluidization, which is widely used in process industries. The phenomenon of fluidization is based on the principle of a balance between drag force (due to the inflow of gas) and gravity force (due to weight of the solids). At a certain inlet gas velocity, the drag force between gas and particles becomes large enough to balance the weight of the particles. This particular inlet gas velocity is termed the minimum fluidization velocity. The inlet gas velocity is the key factor to characterize fluidization, as shown in Figure 1.1. When increasing the gas velocity beyond the minimum fluidization velocity, the porosity of the bed increases and gas bubbles are formed, in which case the bed is operated as a bubbling fluidized bed. At higher gas velocities, the bed can be further characterized by a slugging regime, and subsequently leads to a turbulent and fast fluidization regime, which prevails in circulating fluidized bed risers. When the gas superficial velocity is sufficiently high, all particles are entrained, leading to very dilute systems with a rather uniform solids distribution throughout the whole system, where the slip velocity (the difference between the gas and the particle velocities) can be assumed to be equal to the particle terminal velocity often referred to as the pneumatic conveying regime. In this work, two typical types of fluidized beds are investigated namely bubbling beds and circulating beds.

1.1.1   Gas-solid bubbling fluidized beds

Fluidized beds working in the bubbling regime feature gas bubbles forming and rising inside the emulsion phase. Bubbling fluidized beds are often encountered in processes involving separation, classification, drying and mixing of particles due to their favourable hydrodynamic and heat transfer characteristics. Many of the important applications of fluidized beds involve highly exothermic or endothermic reactions which give rise to either a high rate of heat removal or heat supply to the system. The gas bubbles collectively affect the overall heat transfer rate and thus affect the overall performance of the fluidized systems. The inlet gas temperature is usually different from the bed temperature, thus the bubble phase is at a different temperature compared to the gas-solid emulsion phase in fluidized beds. Consequently gas-particle heat transfer is of great interest.
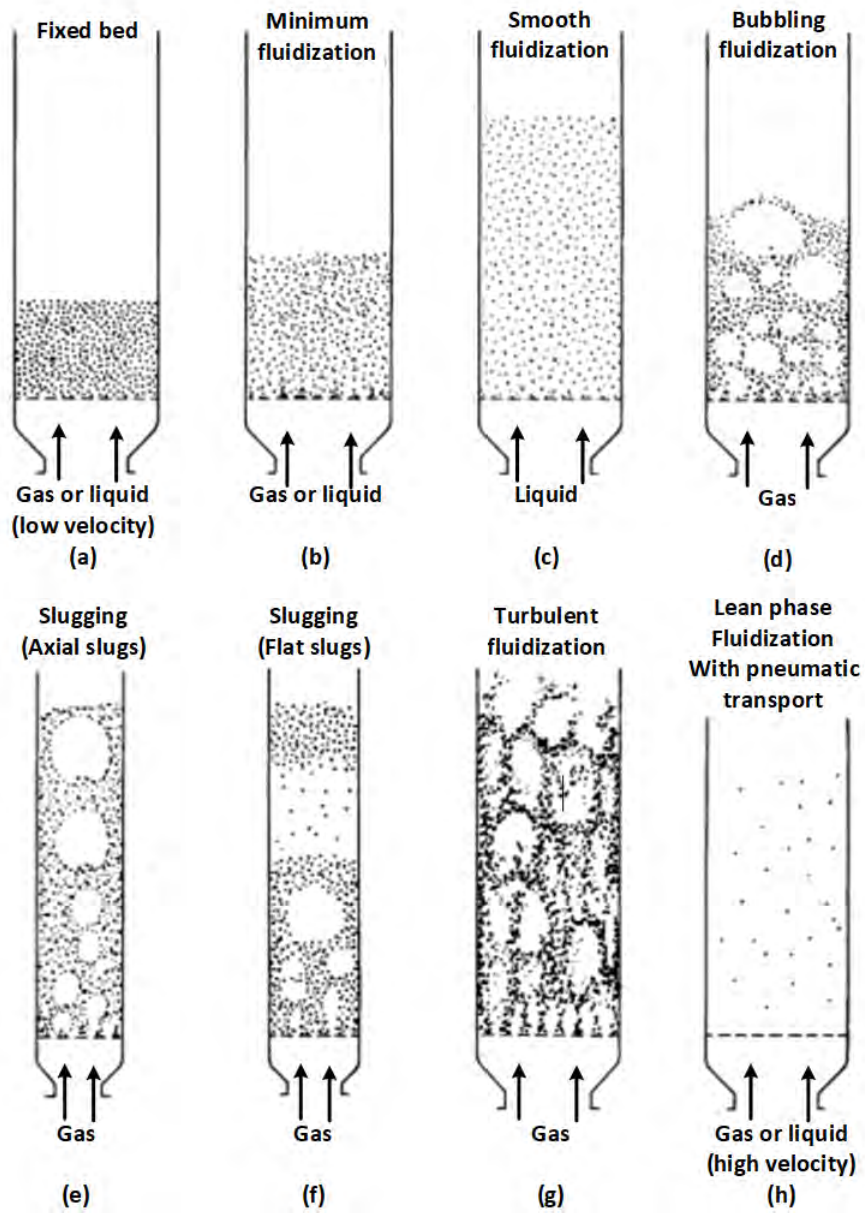
Fig. 1.1 Various forms of contacting of a batch of solids by fluid. (Kunii and Levenspiel, 1991b)

1.1.2 Gas-solid circulating fluidized beds

Gas-solid circulating fluidized beds have a wide range of applications in various industries to carry out chemical processes that require short gas residence times, such as fluid catalytic cracking, biomass, coal gasification, polymerization, drying and granulation (Kunii and Levenspiel, 1991b). Circulating fluidized beds consist of a riser, a downcomer, cyclone and a recycling pipe. Risers are usually operated at high superficial velocities which enhance a large

3

solids carryover. Under fast fluidization conditions, a so-called "core annulus" flow pattern will be most prevalent in the riser systems which is characterized by a dense down-flow close to the walls and a dilute solids up-flow in the core region of the reactor. Under these conditions, clusters form and mostly in the regions close to the walls. Consequently, the flow pattern in a circulating fluidized bed is characterized by a complicated structure with continuous formation and disintegration of clusters of particles. Clusters have a profound impact not only on the riser hydrodynamics, but also on mass and heat transport phenomena. Thus, it is relevant to understand how clustering phenomena are affected by the operating conditions such as gas superficial velocity, solids mass flux.

1.2   Multiphase flow modelling

The design and scale-up of fluidized beds requires accurate models that enable quantification of the performance of reactors. Consequently, numerous studies have been performed on the fundamentals of fluidization. These studies can be divided into two general classes: experimental investigations and computational approaches. Each of these approaches have their own advantages and disadvantages. Computational methods can be relatively cheap, and they can provide some detailed information that is not easily accessible via experimental methods. On the other hand, computational models require validation using experimental data. Thus, these two different approaches are complementary to each other. The work described in this thesis will focus on the usage of computational methods to advance over understanding of the behaviour and characteristics of gas-solid fluidized beds. In recent decades, various computational models have been developed for studying the behaviour of fluidized beds. Depending upon the assumptions in the model, it is possible to apply them from small to large scale systems, shown in Figure 1.2. Among these models, we can refer to Direct Numerical Simulations (DNS), Discrete Element Model (DEM), Two Fluid Model (TFM), Direct Simulation Monte Carlo (DSMC), Discrete Bubble Model (DBM) and two phase model. Here only the most common three are discussed. DNS, at the most detailed level, treats the fluid and particulate phases by considering the Navier-Stokes equation and the Lagrangian equations of motion respectively. DNS fully resolves the flow around the particles and can be used to establish relationships for the drag closures. These drag closures are employed in DPM and TFM simulations. At the largest scale The Two-Fluid Model is based on a Eulerian-Eulerian approach and both the fluid and the solid phases are considered as interpenetrating fluids by a set of generalized Navier-Stokes equations (Kuipers and van Swaaij, 1998).
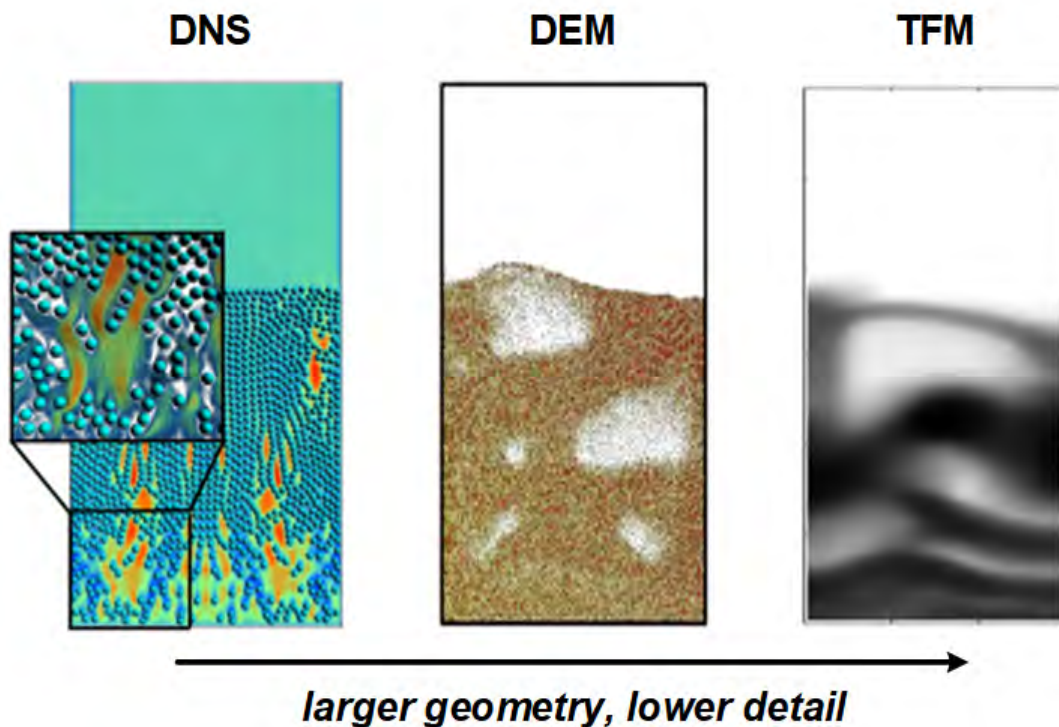
Fig. 1.2 Multiscale modelling schemes for gas-fluidized beds.

In the past decades, CFD-DEM has become a powerful tool for solving industrial-scale problems (Cleary et al., 2003; Džiugys and Peters, 2001; Kuwagi and Horio, 2002). In CFD-DEM the gas phase is treated as a continuum (Eulerian) and the particulate phase as discrete (Lagrangian). Through two-way-coupling both the continuum and particulate phase experience each other through momentum exchange.

The main advantage of the CFD-DEM is its possibility to model highly complex systems using the basic physical properties of individual particles without oversimplifying assumptions. In the meanwhile, particle motion is dictated by particle–fluid interactions, particle–wall interactions, and particle–particle inter-actions.

The main disadvantage of the CFD-DEM technique, in comparison with the above mentioned methods, is related to computational requirements. This limits the number of particles in simulations (Hoomans et al., 2000) and achievable physical time in process simulations. To maintain a stable numerical scheme, the time step must be small enough to allow particle–particle interaction and particle–wall interaction to occur over the duration of several time steps. This limit of the time step is related to the size of the particles, the minimum fluidization velocity and the grid size. Secondly the number of particles affect the number of collision detection evaluations that need to be made. Researchers have developed

several methods to optimize these procedures for vector supercomputers (Schoen, 1989), building special-purpose hardware for performing molecular dynamics simulations (Bakker et al., 1990), designing reconfigurable co-processors for DEM simulation (Schäfer et al., 2004), developing parallel DEM codes (Rapaport, 1991), investigating efficient contact search algorithm (Brosh et al., 2014) and coarse graining techniques. Girardi et al. (2016) performed series of simulations of wet fluidized beds of particles in small periodic domains by using a CFD-DEM approach. The CFD-DEM results are systematically coarse-grained to expose the dependence of the filtered drag coefficient on Eulerian filter size, surface tension forces, liquid loading, and solids loading in wet gas–solid fluidized beds. Coarse graining is achieved by artificially increasing the size of the particles, such that fewer particles need to be represented, which is illustrated in Figure 1.3. This approach requires scaling of the relevant particle-particle and particle-fluid forces counterparts as well as a correct spatial representation, meaning the mapping of particle properties to the fluid mesh and vice-versa.
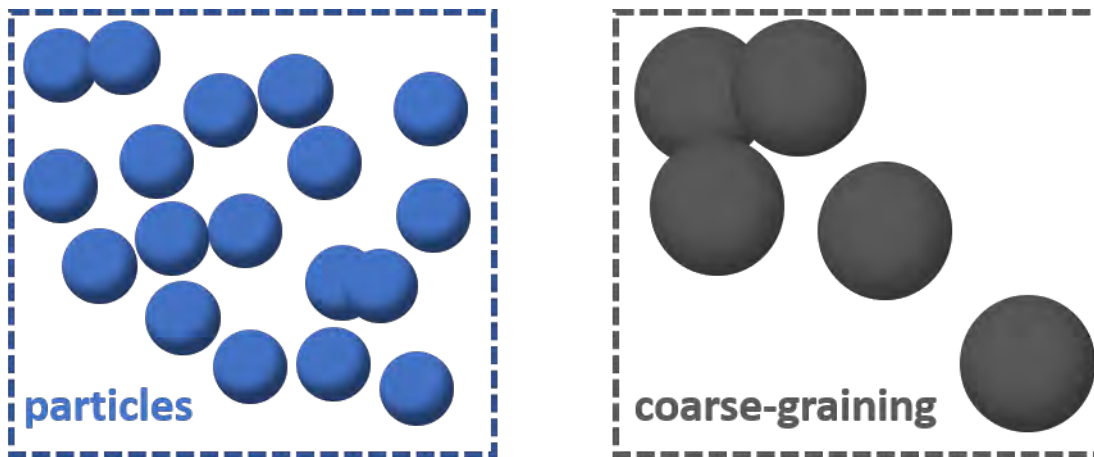
Fig. 1.3 Elementary particles in a given volume (left); Coarse-graining particles in the same volume (right).

1.3 Motivation

The first main objective of this research is to generate more insight into the hydrodynamics and heat transfer characteristics of gas-solid bubbling fluidized beds by employing the granular discrete element model of gas-solid flows. To achieve this, a new heat transfer model is implemented which considers the heat source term. This model system is used to mimic the temperature distributions and heat transfer phenomena due to heterogeneous exothermic reactions prevailing in bubbling gas-fluidized beds. The second goal of this project is to develop an efficient and accurate scaling method based on the CFD-DEM

model to investigate hydrodynamics in CFB risers. The scaling method is compared with experimental data reported in literature to study the hydrodynamics in gas-solid circulating fluidized beds. Furthermore, the hydrodynamics of a binary systems is investigated to study the behaviour and applicability of the scaling method for a bidisperse particle system. Finally, a systematic study on the circulating fluidized bed riser with different geometry configurations is performed by comparing the numerical results with experimental data.

1.4   Thesis outline

The thesis consists of two parts: in part one the heat transfer and hydrodynamics in bubbling fluidized beds is introduced and investigated in detail. Part two describes the hydrodynamic behaviour, including cluster phenomena in circulating fluidized beds, obtained with CFD-DEM and a scaling method.

In Chapter 2, a heat transfer model is introduced by implementing the particle energy equation with constant heat source term. Using this model, the thermal behaviour of a heterogeneous exothermic reaction system was mimicked. The model has been incorporated into the open-source software CFDEM coupling for the modelling of bubbling fluidized beds. For verification, a comparison of the present model with a semi-analytical solution for transient heat transfer in a fixed bed is carried out. Furthermore, the thermal behaviour and hydrodynamics of gas-solid bubbling fluidized beds are studied.

In Chapter 3, some geometric configurations of circulating fluidized bed risers are investigated. Specifically the influence of the solids inlet and outlet configurations as well as the effect of gas superficial velocity on the flow motion in riser reactors is analysed. The DEM simulations are validated by comparing with PIV-DIA experimental data (Varas et al., 2017).

In Chapter 4, a scaling method is proposed for scaling the momentum equation of granular particles to scale down the vast number of solid particles in large industrial systems. Based on this method, the gravity, pressure, drag force, normal and tangential inter-particle contact forces are scaled respectively. The behaviour of the scaling method on hydrodynamics including flow performance and cluster characteristics of circulating fluidized beds is reported. The scaling method is fully validated by scaling the grid size and the riser depth of the riser reactor.

Finally, in Chapter 5, the hydrodynamics of the binary system in a pseudo-2D gas-solid circulating fluidized bed is studied, using CFD-DEM based on our newly developed scaling method. Finally, the scaling model on binary systems is verified by detailed comparison with the experimental results from Mathiesen et al. (2000) for a cylindrical circulating fluidized bed.

Chapter 2

Hydrodynamic and Heat Transfer Study of A Fluidized Bed by Discrete Particle Simulations

[1]

---

[1]This chapter is based on: *L. Mu, K.A. Buist, J.A.M. Kuipers, N.G. Deen. (2020). Hydrodynamic and heat transfer study of a fluidized bed by discrete particle simulations. Processes, 8(4),463.*

Abstract

A numerical simulation study is carried out to study the combined thermal behavior and hydrodynamics of a pseudo 2D fluidized bed using a Computational Fluid Dynamics – Discrete Element Method (CFD-DEM). To mimic the effect of heterogeneous exothermic reactions, a constant heat source was implemented in the particle energy equation. The effect of superficial gas velocity, bed height and heat source distribution was analyzed with the aid of averaged volume fraction and temperature distributions and velocity profiles. The comparison between results from an in-house code and an open-source code reveal similar trends for both state-of-the-art CFD-DEM codes. Moreover, it is found that both the gas superficial velocity and the bed aspect ratio have a profound influence on the fluidization behavior and temperature distributions.

2.1   Introduction

Fluidized beds are encountered in a variety of industrial processes because of their favorable heat transfer characteristics. Many of the important applications of fluidized beds involve highly exothermic or endothermic reactions which give rise to either a high rate of heat removal or heat supply to the system. Fluid catalytic cracking, fluidized bed coal combustion and polymerization for production of polyethylene are some of the well-known processes. Hence, in-depth knowledge of the heat transfer processes in fluidized beds is highly relevant. The hydrodynamics of fluidized beds has been investigated by many researchers. Moreover, extensive studies of heat transfer in fluidized beds have been reported with many supporting theories proposed on the prevailing heat transfer mechanisms, see the work of Basu and Nag (1987); Kunii and Levenspiel (1991a); Zhou et al. (2009, 2010) e.g.

Most of the previous heat transfer research on fluidized beds involved the use of temperature probes placed inside or on the walls of fluidized beds, see the work of Borodulya et al. (1985); Valenzuela and Glicksman (1984). Limtrakul et al. (2004) and Zhou et al. (2004) previously used CFD-DEM to study the hydrodynamics combined with heat transfer in fluidized beds. However, only recently heat transfer extensions to CFD-DEM have been used for bubble to emulsion heat transfer studies in pseudo 2D beds, see Patil et al. (2014).

In this paper, the CFD–DEM approach, a computational fluid dynamics (CFD) model for gas-phase flow combined with a discrete element method (DEM) for particle motion (Deen et al., 2007; Van der Hoef et al., 2008), was used to study the influence of the particle size and the superficial gas velocity on the fluidized bed thermal behavior. CFD-DEM simulations are performed for a pseudo 2D fluidized bed with spherical particles. The thermal energy equation of the particles contains a source term to mimic the heat production due to a heterogeneous exothermic chemical reaction. The simulations are carried out with an open-source package, OpenFOAM-CFDEM-LIGGGHTS, and are compared with results obtained previously by Li et al. (2016) with an in-house CFD-DEM code. The objective of this work is to study the influence of superficial gas velocity, bed aspect ratio and heat production distribution on the hydrodynamics and heat transport in the bed.

2.2 Governing equations

The CFD-DEM model is an Euler-Lagrange model, which was originally developed by Hoomans et al. (1996). In the CFD-DEM the gas phase hydrodynamics is described by the Navier-Stokes equations, and the motion of each particle in the system is calculated from Newton's second law. The volume-averaged conservation equations for gas phase mass and momentum are given by:

$$\frac{\partial (\varepsilon_g \rho_g)}{\partial t} + \nabla \cdot (\varepsilon_g \rho_g \mathbf{u}_g) = 0 \tag{2.1}$$

$$\frac{\partial (\varepsilon_g \rho_g \mathbf{u}_g)}{\partial t} + \nabla \cdot (\varepsilon_g \rho_g \mathbf{u}_g \mathbf{u}_g) = -\varepsilon_g \nabla p_g - \nabla \cdot (\varepsilon_g \tau_g) - \mathbf{S} + \varepsilon_g \rho_g \mathbf{g} \tag{2.2}$$

where $\mathbf{S}$ represents the source term for momentum originating from the particulate phase. In this work, the Beetstra drag force correlation (Beetstra et al., 2007) has been used to calculate the interphase momentum transfer coefficient:

$$\mathbf{S} = \frac{1}{V_{cell}} \sum_{i=0}^{N_p} \frac{\beta V_p}{1 - \varepsilon_g} (\mathbf{u}_g - \mathbf{v}_p) D(\mathbf{r} - \mathbf{r}_p) \tag{2.3}$$

The solid phase is considered to be discrete and consequently the modeling of this phase is based on tracking of individual particles accounting for particle-particle and/or particle-wall encounters. The motion of a single spherical particle with mass m_p and moment of inertia I_p can be described by Newton's equations, for spheres:

$$m_p \frac{d^2 \mathbf{r}_p}{dt^2} = -V_p \nabla p + \frac{\beta V_p}{1 - \varepsilon_g} (\mathbf{u}_g - \mathbf{v}_p) + m_p \mathbf{g} + \mathbf{F}_c \tag{2.4}$$

$$I_p \frac{d\omega_p}{dt} = \tau_p \tag{2.5}$$

where $\mathbf{r}_p$ is the particle position. The forces on the right-hand side of Eq. 2.4 are due to the pressure gradient, drag, gravity and contact forces due to collisions with other particles. For the contact force, a linear spring dashpot model (i.e. Hertz model) is used. τ_p is the torque, and ω_p is the angular velocity.

The thermal energy equation of the gas phase is given by:

$$\frac{\partial (\varepsilon_g \rho_g C_{pg} T_g)}{\partial t} + \nabla \cdot (\varepsilon_g \rho_g \mathbf{u}_g C_{pg} T_g) = \nabla \cdot \left(\varepsilon_g k_g^{eff} \nabla T_g \right) + \mathbf{Q}_p \tag{2.6}$$

13

where $\mathbf{Q}_p$ represents the source term originating from interphase energy transfer whereas k_g^{eff} is the effective thermal conductivity of the gas phase that can be expressed in terms of the microscopic fluid thermal conductivity (k_g) as follows:

$$k_g^{eff} = \frac{1 - \sqrt{1 - \varepsilon_g}}{\varepsilon_g} k_g \tag{2.7}$$

This equation was originally proposed by Syamlal and Gidaspow (1985). The source term due to the heat transfer of the particles to the gas phase can be obtained by summing and distributing the contributions of all particles using a discrete Dirac delta-function D as flows:

$$Q_p = \sum_p h A_p (T_p - T_g) D (\mathbf{r} - \mathbf{r}_p) \tag{2.8}$$

where T_p is the particle temperature, T_g is the temperature of the gas phase at the Eulerian position $\mathbf{r}$ and h is the fluid-particle heat transfer coefficient, obtained from the empirical correlation by Gunn (1978):

$$Nu_p = \left(7 - 10\varepsilon_g + 5\varepsilon_g^2\right)\left(1 + 0.7Re_p^{0.2}Pr^{0.33}\right) + \left(1.33 - 2.40\varepsilon_g + 1.20\varepsilon_g^2\right)Re_p^{0.7}Pr^{0.33} \tag{2.9}$$

$$Nu_p = \frac{hd_p}{k_g}, Re_p = \frac{\varepsilon_g\rho_g|\mathbf{u}_g - \mathbf{v}_p|d_p}{\mu_g}, Pr = \frac{\mu_g C_{pg}}{k_g} \tag{2.10}$$

where Re_p and Pr are the particle Reynolds number and Prandtl number. The thermal energy equation for each particle phase is given by:

$$m_p C_{pp} \frac{dT_p}{dt} = h A_p (T_g - T_p) + \dot{q} V_p \tag{2.11}$$

where $\dot{q}$ is the heat production rate due to exothermal intra-particle chemical conversion.

2.3 Model verification

In this section, two cases respectively without and with heat source term were conducted to verify the heat transfer implementation. The test system is taken as a fixed bed with initially cold particles (273K) that is heated up by a hot gas flow (373K) that passes through the bed uniformly from the bottom of the bed. The particles were uniformly arranged in a block structure and maintained stationary, which is a similar geometry as used by Van Sint Annaland et al. (2005), Patil et al. (2014) and Li et al. (2016). In the CFD-DEM verification simulations, the physical properties of the particles and the gas are listed in Table 2.1. The geometrical characteristics of the bed have been summarized in Table 2.2.

Table 2.1 Particle and gas phase properties in the fixed bed verification.

Gas density $\left(\mathrm{kg/m^3}\right)$, ρ_g	1000
Inlet gas temperature (K), $\mathbf{T}_{g,0}$	373
Gas viscosity (Pa·s), μ_g	1.0×10^{-3}
Gas heat capacity (J/kg/K), C_{pg}	4187
Gas thermal conductivity (W/m/K), k_g	0.5
Particle diameter (m), d_p	3.95×10^{-3}
Particle density $\left(\mathrm{kg/m^3}\right)$, ρ_p	8400
Initial temperature of gas and particles (K)	273
Particle heat capacity (J/kg/K), C_{pp}	385

Table 2.2 Settings for DEM simulations of the fixed bed.

Width of the bed (m)	0.1
Depth of the bed (m)	0.1
Initial particle bed height (m)	0.5
Particle number	$78,125\,(25 \times 25 \times 125)$
$\Delta x = \Delta y = \Delta z\,(\mathrm{m})$	0.004
Time step of particle phase (s)	0.0001
Time step of gas phase (s)	0.002

The simulation results were verified by comparing them with results from a semi-analytical model. The latter is based on a one dimensional convection equation with interphase heat transfer between the gas and solid phase. For the 1-D model, the gas and particle phase energy balances are given by:

$$\varepsilon_g \rho_g C_{pg} \frac{\partial T_{g,z}}{\partial t} = -\varepsilon_g \rho_g u_{g,z} C_{pg} \frac{\partial T_{g,z}}{\partial z} + h a_s \left(T_{p,z} - T_{g,z}\right) \tag{2.12}$$

$$(1 - \varepsilon_g) \rho_g C_{pp} = h a_s \left(T_{g,z} - T_{p,z} \right) \tag{2.13}$$

where a_s is the specific interfacial area given by $a_s = 6 \frac{(1 - \varepsilon_g)}{d_p}$. The details of the analytical solution of Eqs. 2.12 and 2.13 can be found in Bird et al. (2001). Dimensionless axial temperature profiles of both phases without heat production are shown in Figure 2.1. In the plot, the simulation results are compared with the semi-analytical data from the 1D model. Figure 2.2 shows simulation results in the case with heat production.

It is found that the results of both models (both without and with heat production) agree very well. Hence, we conclude that the heat transfer model is correctly implemented in the 3D CFD-DEM model and can be used for heat transfer studies of fluidized beds.
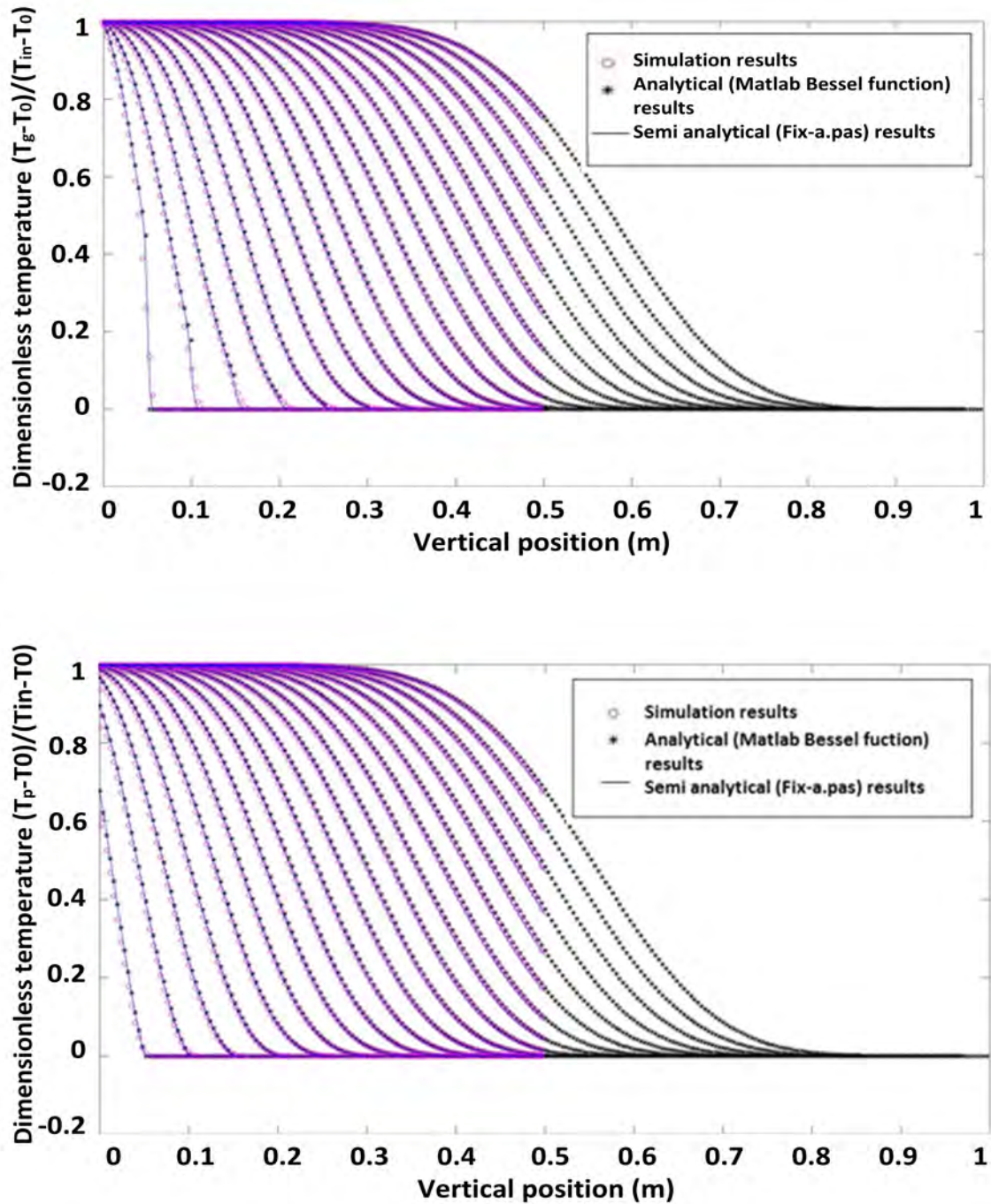
Fig. 2.1 Dimensionless axial gas and particle temperature profiles without heat production.
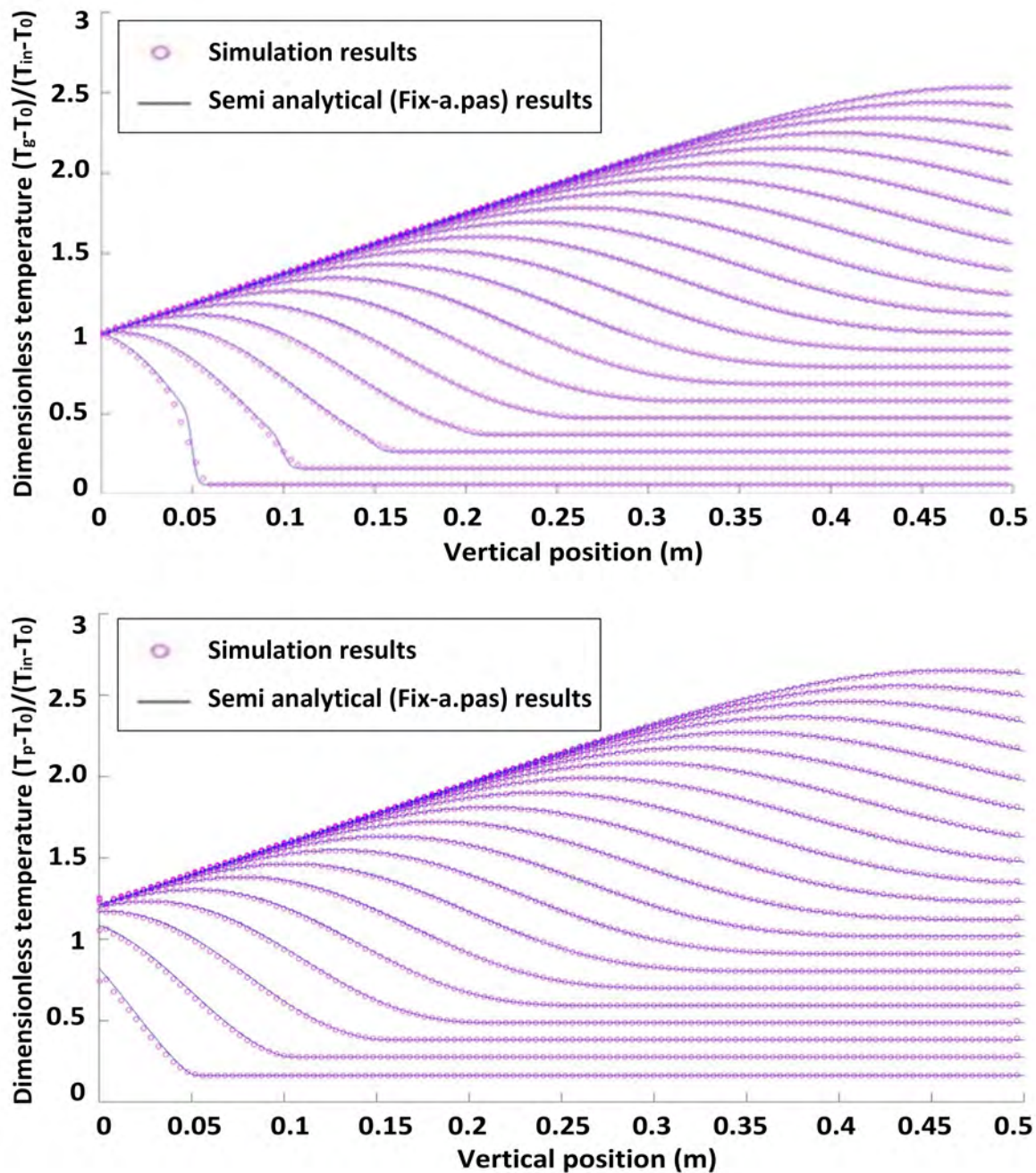
Fig. 2.2 Dimensionless axial gas and particle temperature profiles with heat production.

2.4 Simulation settings

A series of fluidization simulations were performed using the OpenFOAM-CFDEM-LIGGGHTS package (we will refer to this package as CFDEM from here) of a pseudo-2D fluidized bed, which is schematically presented in Figure 2.3. Details of the geometry are shown in Table 2.4. The simulations were carried out with particles of 0.995 mm in diameter, which are classified as Geldart D type particles. Simulations were performed for initial bed heights of 0.04 m (aspect ratio 0.5), 0.08 m (aspect ratio 1) and 0.16m (aspect ratio 2). The number of particles in the system amounted respectively 37,225, 74,450 and 148,900. Free slip boundary conditions were applied to the front and back wall, and no slip boundary conditions for the left and right walls. Table 2.1 summarizes the basic properties of the gas and particles that were used in the simulations.
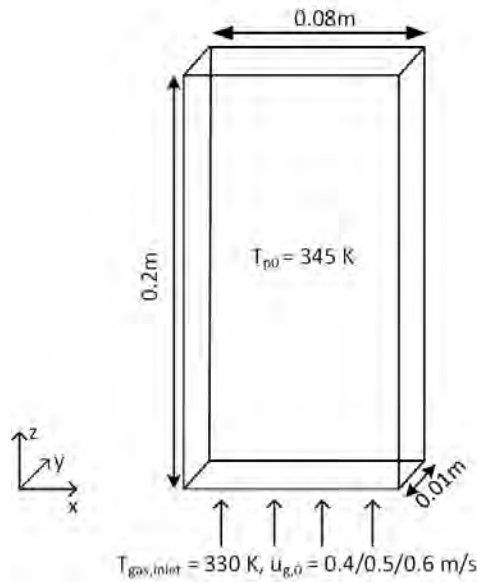
Fig. 2.3 Schematic overview of pseudo-2D fluidized bed.

Simulations were performed for several gas superficial velocities, namely 0.4 m/s, 0.5 m/s, 0.6 m/s (u_{mf} = 0.262 m/s). The particles are initialized at a temperature of 345 K, and stacked on a cubic lattice at the bottom of the bed, after which a constant gas stream with $T_{g,0}$ = 330 K is supplied through the gas supply at the bottom of the bed. Each particle has a constant heat source of 0.0209 W/m/K, which is the same as used by Li et al. (2016). All simulations were performed for 10 s.

Table 2.3 Gas and particle phase properties in the fluidization simulations.

Gas density (kg/m^3),ρ_g	1.49
Inlet gas temperature (K), $T_{g,0}$	330
Gas viscosity (Pa·s), μ_g	1.0×10^{-5}
Gas heat capacity (J/kg/K), C_{pg}	1670
Gas thermal conductivity (W/m/K), k_g	2.09×10^{-2}
Particle diameter (m), d_p	9.95×10^{-4}
Particle density (kg/m^3),ρ_p	667
Particle heat capacity (J/kg/K), C_{pp}	1670
Normal coefficient of restitution (particle-particle), e	0.6
Youngs Modulus	5.0×10^5
Possion ratio	0.45

Table 2.4 Settings for DEM simulations of the pseudo-2D fluidized bed.

Width of the bed (m)	0.08
Depth of the bed (m)	0.01
Initial particle bed height (m)	0.04/ 0.08/ 0.16
Particle number	37 225/ 74 450/ 148 900
$\Delta x = \Delta y = \Delta z$ (m)	0.0025
Time step of particle phase (s)	1.0×10^{-5}
Time step of gas phase (s)	2.0×10^{-4}

2.5 Results

2.5.1 Effect of superficial velocity and aspect ratio on bed hydrodynamic behavior

Figure 2.4 shows snapshots of the typical volume fraction distribution under conditions for each of the three simulated aspect ratios and superficial gas velocities. From these snapshots it can be observed that bubbles become bigger with increasing gas superficial velocity. From animations, it was observed that bubbles move more chaotically when the superficial gas velocity increases. This effect becomes more apparent with increasing H_0/W.
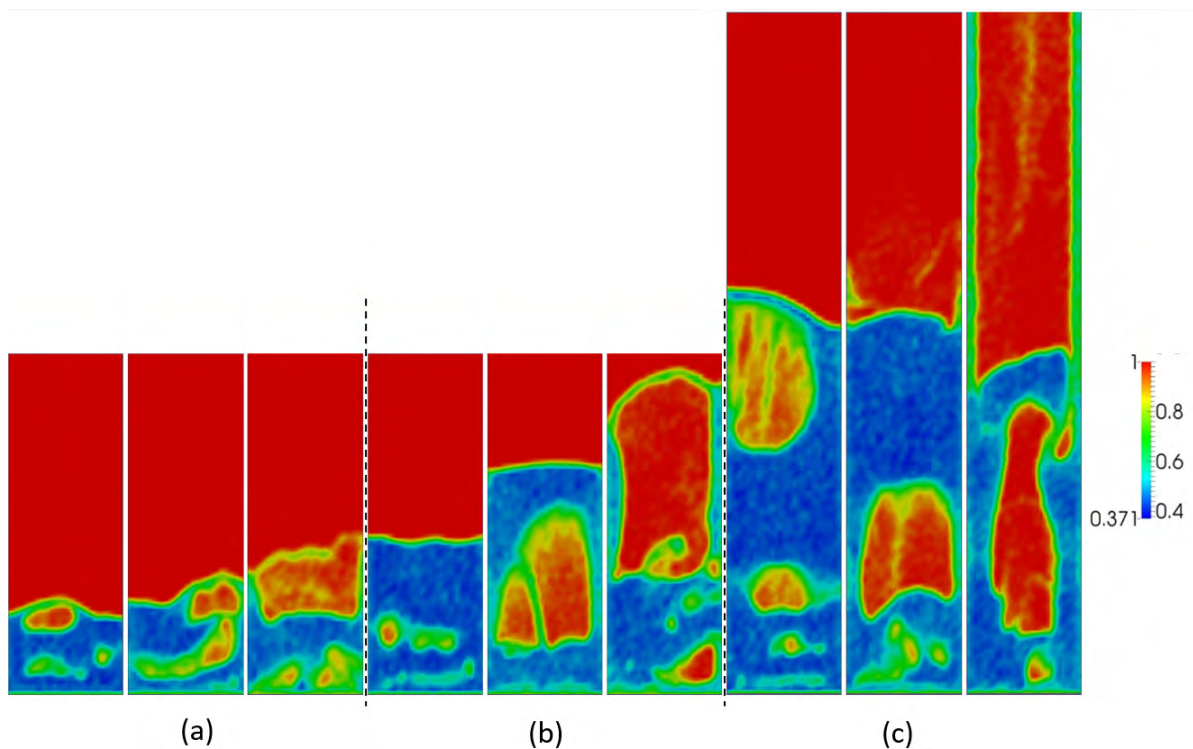
Fig. 2.4 Snapshots of instantaneous voidage patterns for varying aspect ratio: (a) $H_0/W = 0.5$, (b) $H_0/W = 1$, (c) $H_0/W = 2$; and different superficial gas velocity: 0.4, 0.5 and 0.6 m/s (from left to right).

To quantify the effect of the gas superficial velocity and initial bed height on the bubble behavior, the temporally and spatially averaged gas porosity was obtained from the last 8 s of simulation data. In Figure 2.5 we present a comparison between the results obtained from an in-house CFD-DEM code and the open-source CFDEM package. The overall mean bed voidage increases more or less linearly with increasing u_0, which is seen for both codes. But the values of the averaged voidage under high gas superficial velocities from the in-house

code are lower than those from the open-source package. This might be because of the different drag model used in these two series of simulations: the drag model in Li et al. (2016) is the Ergun equation (Ergun, 1952) for the dense regime and the Wen & Yu equation (Wen and Yu, 1966) for the dilute regime, whereas in this work the drag correlation of Beetstra et al. (Beetstra et al., 2007) is used. When the superficial gas velocity increases, the differences of averaged voidage between different aspect ratios increase, which is in line with the observations from Figure 2.4.
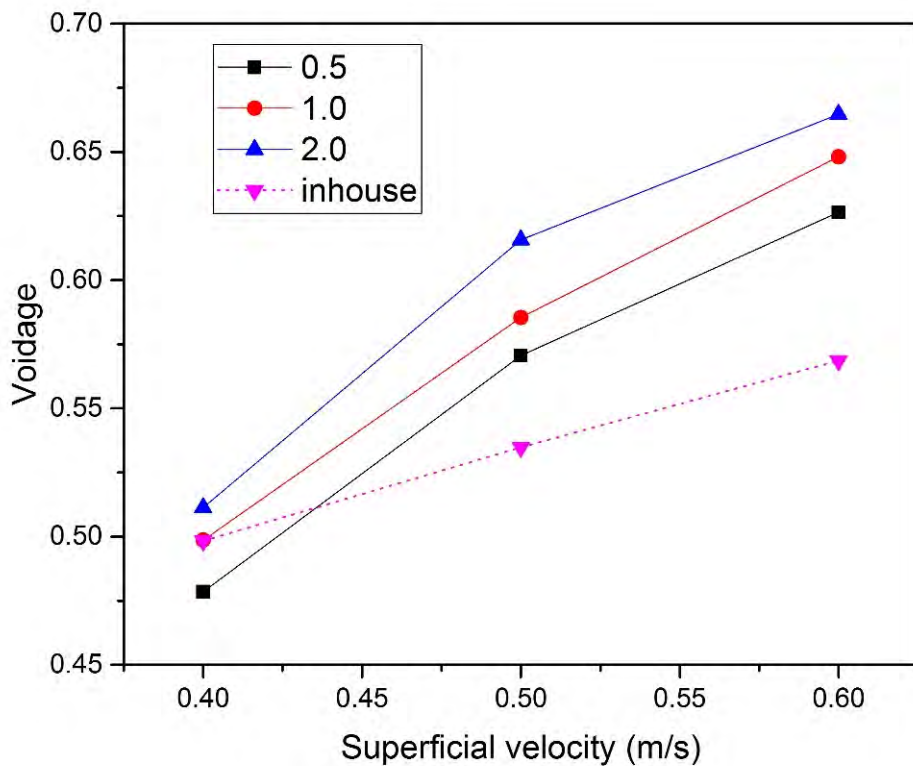
Fig. 2.5 Temporally and spatially averaged bed voidage as a function of superficial velocity and aspect ratio.

To quantify the effect of $u_{g,0}$ and H_0/W on the solids motion, the temporally and spatially averaged particle velocity was obtained from the last 8 s of simulation data. The time-averaged vertical particle velocities at $z = H_0$ as a function of superficial gas velocity and aspect ratio are depicted in Figure 2.6. It can be seen that the particle velocity is affected by the superficial gas velocity as follows: both the up-flow in the core and the down-flow in the annulus are enhanced. This can be attributed to enhanced bubble action. The bed hydrodynamics is also influenced by the aspect ratio, as indicated by the altered shape of the

time-averaged vertical velocity. When the initial bed height increases, the up-flow in the core region becomes larger. This reveals that a higher aspect ratio promotes intensified upward solids motion. We made a comparison at $H_0/W = 1.0$ between the results obtained from the open-source CFDEM package and an in-house CFD-DEM code. They both show the same tendency of vertical particle motion. But the vertical particle velocity has a more uniform distribution from the open-source package under low superficial gas velocities condition.

2.5.2 Effect of superficial velocity and aspect ratio on heat transfer behavior

In this part we will focus on the effect of the gas superficial velocity and bed aspect ratio on the gas-particle heat transfer behavior. Figure 2.7 shows snapshots of the particle temperature at different gas superficial velocity and aspect ratios. With increasing superficial velocity, it is obvious that the particle temperature is more homogeneous. This can be explained by the fact that the particles become better mixed and the heat transfer rate between gas and particles is more intense. The whole bed temperature increases with increasing aspect ratio, which can be explained that with increasing H_0/W the bed mass increases and hence also the associated overall heat source in the bed.

To characterize the bed thermal behavior the temporal and spatial averaged particle temperature was calculated, along with the standard deviation in the particle temperature. Figure 2.8 shows the standard deviation (defined in Equation 2.14) of the particle temperature as a function of the superficial velocity and bed aspect ratio. As can be seen, when the gas superficial velocity increases, the temperature standard deviation decreases in all cases. This can be explained by the fact that at higher u_0 the bed is better mixed and hence becomes more isothermal. Moreover, at higher aspect ratios the relative influence of entrance effects is reduced and particles become better mixed, which further reduces the standard deviation of the particle temperature.

$$\sigma = \sqrt{\frac{1}{N_p} \sum_{i=1}^{N_p} \left(T_{p,i} - \overline{T}_p\right)^2} \tag{2.14}$$

To quantify the effect of $u_{g,0}$ and H_0/W on the thermal behavior, the probability density function (PDF) of the temperature was calculated. The temperature of all particles was made dimensionless by dividing the difference between the particle and inlet gas temperature $(T_p - T_{g,0})$ by the difference between the melting point of particle $(T_{p,m} = 380 \text{ K})$ and the inlet gas temperature $(T_{p,m} - T_{g,0})$. Using this definition dimensionless temperatures of 0 and 1 correspond to a particle temperature equal to respectively the inlet gas temperature
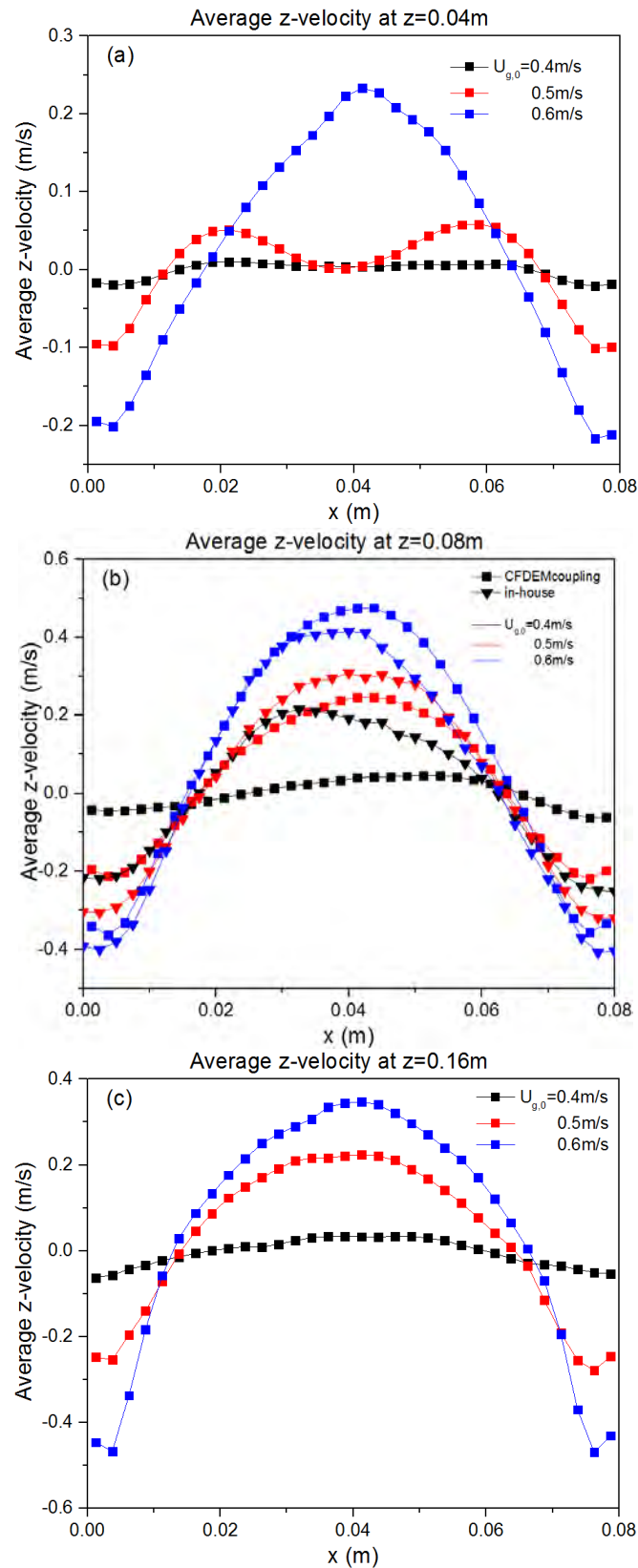
Fig. 2.6 Profiles at different height of time-averaged vertical particle velocity for varying aspect ratio: (a) $H_0/W = 0.5$, (b) $H_0/W = 1.0$, (c) $H_0/W = 2.0$. Note that all profiles are shown at $z = H_0$.

24
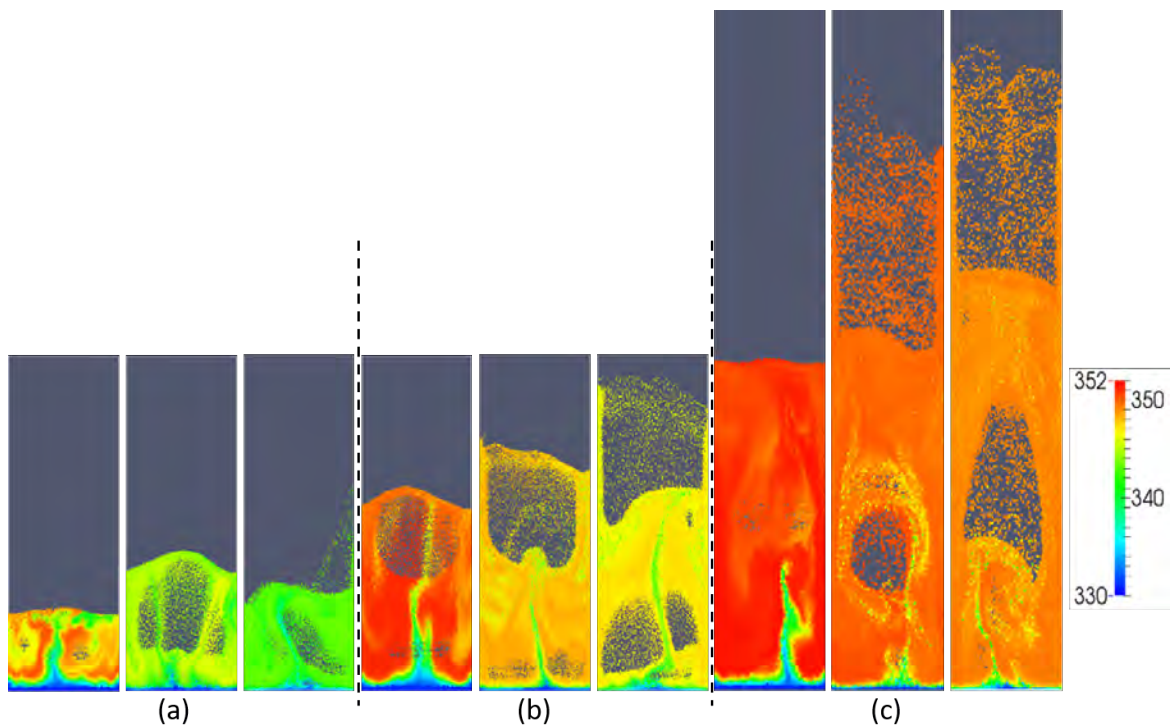
Fig. 2.7 Snapshots of particle temperature as a function of aspect ratio: (a) $H_0/W = 0.5$, (b) $H_0/W = 1$, (c) $H_0/W = 2$; and different superficial gas velocity: 0.4, 0.5 and 0.6 m/s (from left to right).

and the melting point of the solid material. The PDF of the particle temperature was created by dividing the temperature range starting from the inlet temperature of the gas (the lowest temperature in the system) to the melting point of particle (the highest temperature) into 25 equal size bins and counting the number of particles in each of the temperature bins during a period of 0.25-2 s. By increasing $u_{g,0}$, a profound change in the particle temperature PDF can be observed in Figure 2.9. The mean value of the temperature decreases with increasing $u_{g,0}$. It means that increasing superficial gas velocity will remove more reaction heat from particles. When the aspect ratio increases, the mean value of particle dimensionless temperature increases and the dimensionless temperature exceeds 1 at $H_0/W = 2.0$. This can be explained by the fact that at higher initial bed height, there are more particles and consequently a stronger heat source in the bed, which will further increase the equilibrium temperature and particle dimensionless temperature. We also made a comparison at $H_0/W = 1.0$ between the results obtained from an in-house CFD-DEM code and the open-source CFDEM package. Both of these two results show the same tendency and particle temperature distribution.
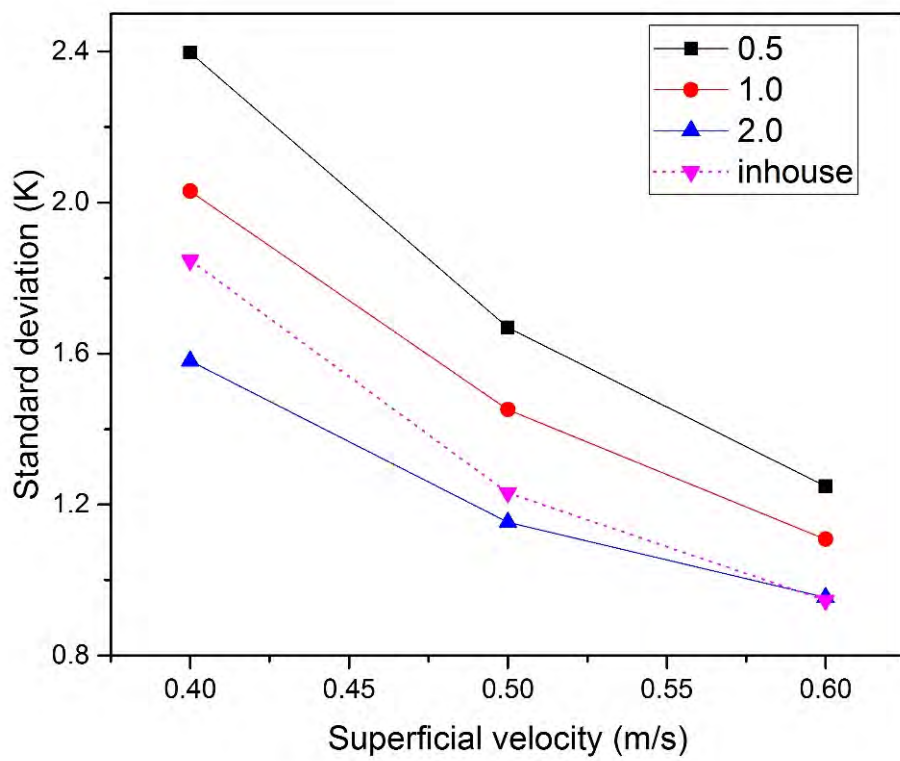
Fig. 2.8 Particle temperature standard deviation as a function of $u_{g,0}$ and H_0/W.
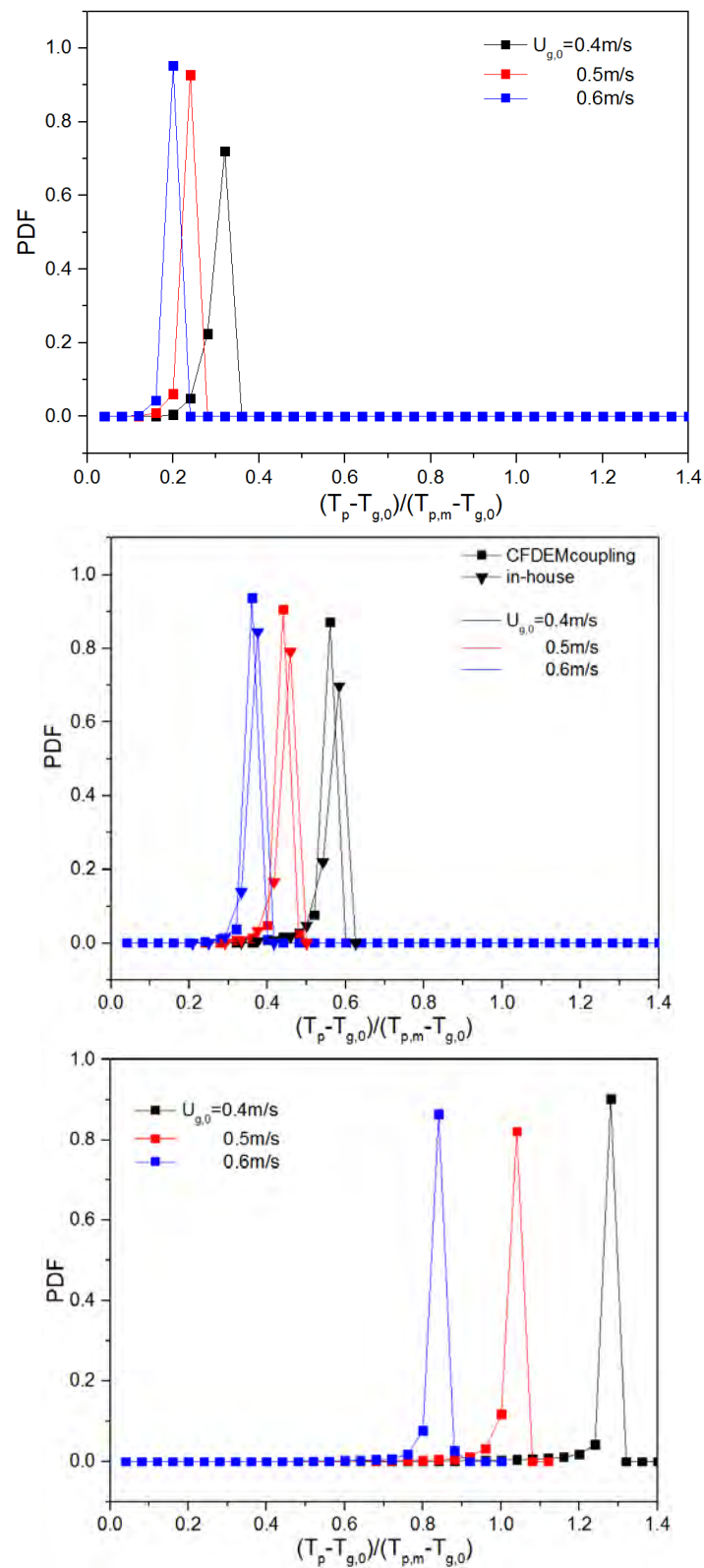
Fig. 2.9 Dimensionless particle temperature PDF for varying aspect ratio: 0.5, 1 and 2 (top to bottom) and different gas superficial velocity.

Fig. 2.10 Snapshots of gas temperature as a function of aspect ratio: (a) $H_0/W=0.5$, (b) $H_0/W=1$, (c) $H_0/W=2$; and different superficial gas velocity: 0.4, 0.5 and 0.6 m/s (from left to right).

2.5.3 Effect of heat source term on heat transfer behavior

In the previous sections, it was assumed that all particles have a uniform heat production. Under realistic conditions though, the heat production will depend on the exact amount of catalyst material in each particle, the degree of deactivation and differences in mass transfer limitations. To investigate the effect of differences in heat production, we define a case with an extreme distribution in heat production properties: 98% "inactive" particles were set to have no heat production, whereas the remaining 2% "active" particles were set to have a heat production 50 times higher than a particle in a bed with a uniform heat production. In this way, both the uniform and non-uniform bed will have the same total heat production.

As can be seen from the snapshots in Figure 2.10, all particles mix well in the bed. Due to the very high heat transfer coefficient, the heat transfer from the active particles to the gas and from the gas to the inactive particles is very efficient.

The mean temperature attains an equilibrium state after 10 s. The steady state bed averaged gas temperature can be derived analytically assuming ideal mixing of both gas and particles. The thus obtained equilibrium temperatures of the gas phase and the inactive (1) and active (2) particles are given by:

$$T_g^x = T_g^{in} + \frac{(\dot{q}_1 X + \dot{q}_2 (1-X)) H_B (1-\varepsilon_g)}{\rho_g C_{pg} u_{g,z}}$$

(2.15)

28

$$T_{p1}^x = T_g^{in} + \frac{(\dot{q}_1 X + \dot{q}_2(1-X))H_B(1-\varepsilon_g)}{\rho_g C_{pg} u_{g,z}} + \frac{\dot{q}_1(1-\varepsilon_g)}{ha_s} \qquad (2.16)$$

$$T_{p2}^x = T_g^{in} + \frac{(\dot{q}_1 X + \dot{q}_2(1-X))H_B(1-\varepsilon_g)}{\rho_g C_{pg} u_{g,z}} + \frac{\dot{q}_2(1-\varepsilon_g)}{ha_s} \qquad (2.17)$$

where X is the percentage of "inactive" particles. The terms on the right hand respectively represent the gas inlet temperature, the adiabatic temperature rise and the temperature difference between gas and particles. Due to the very effective heat transfer, the relatively small temperature difference between "active" and "inactive" particles is an important factor because in reality many types of particles with different activities would be present in the bed simultaneously. The equilibrium temperature of gas and two types of particles with different heat production under different conditions are listed in Table 2.5.

Table 2.5 Equilibrium temperature of the gas phase (T_g) and the active/inactive particles (T_{p1}/T_{p2}).

$H_0/W/u_{g,0}$	Non-uniform cases				Uniform cases	
	T_g	T_{p1}	T_{p2}	$(T_{p1} - T_{p2})/(T_{p1} - T_{g,in})$	T_g	T_p
0.5/0.4	346	346	367	-1.28	346	346
0.5/0.5	343	343	362	-1.5	343	343
0.5/0.6	341	341	359	-1.7	341	341
1.0/0.4	362	362	383	-0.64	362	363
1.0/0.5	356	356	375	-0.75	356	356
1.0/0.6	351	351	370	-0.85	351	352
2.0/0.4	394	394	415	-0.32	394	395
2.0/0.5	381	381	401	-0.37	381	382
2.0/0.6	373	373	391	-0.42	373	373

From the snapshots of gas and particle temperature in Figure 2.10, the gas temperature and the distribution of particles with and without heat source term are shown respectively. Beyond the entrance region, the gas temperature shown in Figure 2.10 is practically homogeneous

and approximately equal to temperature of the inactive particles, as shown in Figure 2.11. This matches well with the equilibrium temperatures given in Table 2.5. Furthermore Figure 2.11 shows the "active" particles distributed through the bed uniformly. As expected from the equilibrium temperatures there is an obvious temperature difference between "inactive" and "active" particles.
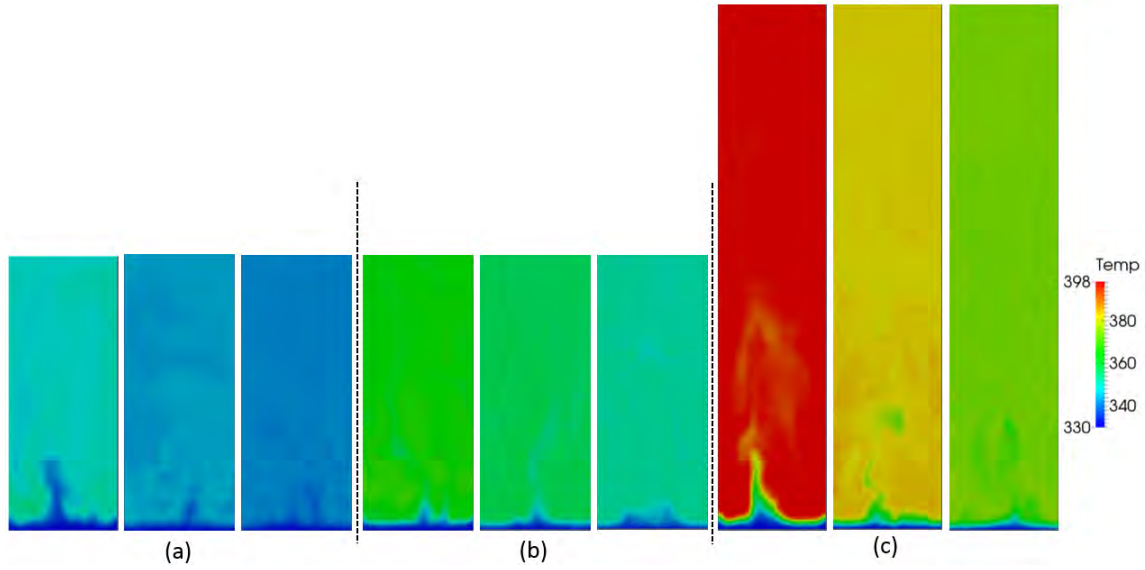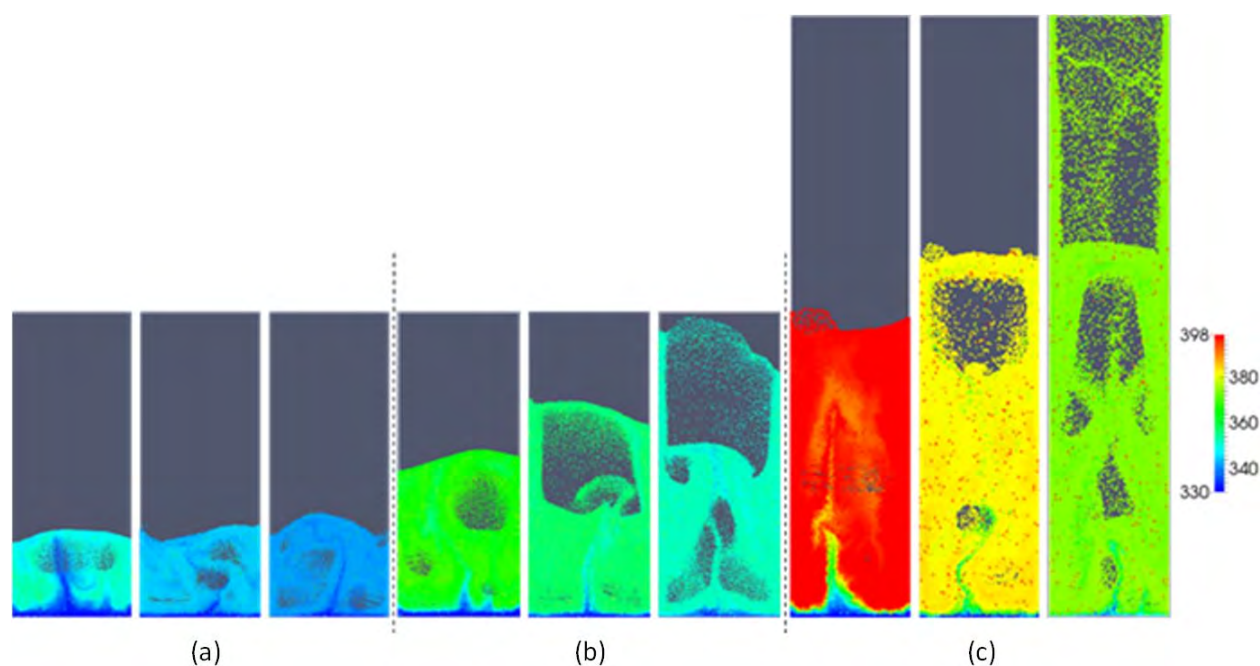

Fig. 2.11 Snapshots of two type particle temperature as a function of aspect ratio: (a) $H_0/W=0.5$, (b) $H_0/W=1$, (c) $H_0/W=2$; and different superficial gas velocity: 0.4, 0.5 and 0.6 m/s (from left to right).

Figure 2.12 shows the Probability Density Function of the particle temperatures, which was created by dividing the temperature range starting from the inlet temperature of the gas (the lowest temperature in the system) up to the melting point of particle (the highest temperature) into 50 equal size bins and counting the number of particles in each of the bins during a period of 10 - 20 s. The equilibrium temperatures of the (in)active particles are included for reference.

By comparing the temperature PDF's in Figure 2.9 (uniform heating) and the left column of Figure 2.12 (non-uniform heating), we can see that in both cases the temperature distribution is more uniform at lower superficial velocity. In the case of the non-uniform heating, a small extra peak appears associated with the small number of (very) active particles.

To inspect the behavior of the active particles, separate PDF's were obtained for both the inactive and active particles only (see respectively the middle and right column of Figure 2.12). With lower superficial velocity and lower H_0/W, inlet effects are dominant, leading to
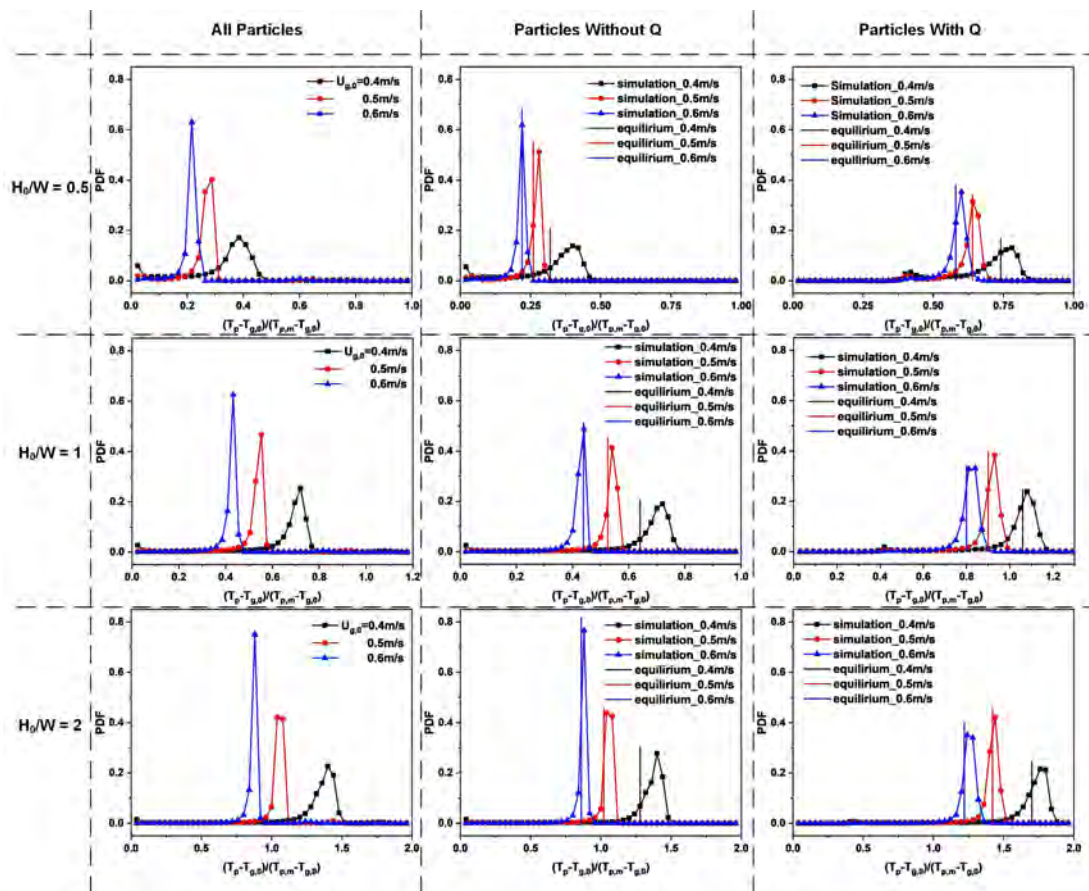
Fig. 2.12 Dimensionless temperature PDF of all particles, inactivity particles and activity particles for different gas superficial velocities and varying aspect ratio: 0.5, 1 and 2.

long tails towards low temperatures for both particles classes. From the comparison between simulation results and equilibrium temperature we observe that there still are differences, and the differences become larger at lower superficial velocity. This is due to the fact that the assumption of a thermally ideally mixed bed is not valid. This also illustrates the added value of fluidized bed CFD-DEM simulations for the inspection of hot and cold zones in the bed.

2.6   Conclusions

In this chapter, CFD-DEM simulations of a non-isothermal gas-fluidized bed were presented. A heat source was incorporated in the particle phase thermal energy equation to mimic the heat liberation due to chemical conversion.

The influence of the gas superficial velocity and bed aspect ratio on the hydrodynamics and thermal behavior of a pseudo 2D fluidized bed have been analyzed. With increasing superficial velocity and initial bed height the overall mean bed voidage increases more or less linearly. The standard deviation of particle temperature provides quantitative information on the particle temperature distribution. At higher aspect ratio and with increasing $u_{g,0}$, the particles become better mixed, reducing the standard deviation. The open-source package simulation data has the same tendency as in the in-house CFD-DEM code simulation results of Li et al. (2016). Furthermore, the time-averaged particle velocity profiles strongly depend on $u_{g,0}$ and H_0/W. Enhanced particle circulation with increasing superficial velocity is observed, whereas more particles are transported upwards in the central region for increasing initial bed heights. The fluidized bed is more isothermal when the superficial gas velocity and aspect ratio increase. The diversity of particles with and without heat production also has an apparent effect on heat transfer behavior. Due to the very good heat transfer characteristics it is seen that the heat transfer from very active particles via the gas phase to the non-active particles is very effective. The gas and particle temperatures predicted by CFDEM simulations agree reasonably well with the equilibrium temperatures.

Chapter 3

CFD-DEM Simulations of Riser Geometry Effect and Cluster Phenomena

[1]

Abstract

In this paper the influence of the inlet and outlet configurations of a pseudo-2D fluidized riser on the hydrodynamics (i.e. flow pattern and cluster characteristics) are studied. A detailed comparison between experimental data and full 3D CFD-DEM simulation results is performed. Solids volume fraction and mass flux are characterized and particle clusters are detected in our CFD-DEM simulations and compared to experimental data. It is shown that a correct representation of the outlet is very important for a correct simulation of the solids holdup in the top section of the riser. The core-annulus flow behavior is generally well predicted by the model and cluster characteristics such as cluster occurance and velocity are also in good agreement with experimental data. Finally, an outlook is given for the future use of CFD-DEM simulation approaches to study riser flows.

3.1 Introduction

Circulating fluidized beds (CFB) are extensively employed in a large variety of chemical and process industries that require short gas residence times (Geldart and Rhodes, 1986; Hartge et al., 1988; Horio and Kuroki, 1994; Niewland et al., 1994; Yerushalmi, 1985). These systems consist of a riser where usually the main reactions take place, a cyclone, a downcomer and a return leg. Risers are usually operated at high superficial velocities yielding a fast fluidization regime. In most CFBs, the solids are fed from the return leg to the riser and interact with the gas phase while flowing upwards. The non-uniform solids distribution has a strong effect on the quality of the gas-solids contact and consequently on riser reactor performance. Understanding and prediction of the complex hydrodynamic behavior is of importance for the proper design of CFBs. Considering the broad range of applications of CFBs, numerous experimental and computational investigations have been carried out (Benyahia, 2012; Hua et al., 2014; Li et al., 2014; Wang et al., 2017). Experimental investigations clearly demonstrated an inhomogeneous solids distribution in both the axial and radial directions (Miller and Gidaspow, 1992). These systems typically exhibit a so-called "core-annulus" flow pattern, which is characterized by dilute solids up-flow in the core of the riser, and a dense down-flow along the walls. Due to the loss of energy during particle-particle collisions, the involved particles tend to form clusters, mainly close to the walls. It is known that these clusters have an impact on the solids residence time distribution and profoundly influence not only the riser hydrodynamics, but also the mass and heat transport characteristics (van der Ham et al., 1994). Thus it is relevant to know how the clustering phenomena and hydrodynamics are affected by e.g. gas superficial velocity and the inlet and outlet configuration.

To this end, the hydrodynamics in riser flows has been widely investigated over the past decades using a number of different models (Gidaspow et al., 2004; Kadyrov et al., 2019; Kuang et al., 2020; Muhammad et al., 2019; Rashid et al., 2020; Wu et al., 2021; Zhu et al., 2020). The contact efficiency between the gas and solids phase has been shown to significantly influence the performance of riser reactors Guenther and Breault (2007). Thus, an accurate representation of clustering properties is believed to be essential to accurately predict the overall conversion rates of chemical processes (Sundaresan, 2013). Clusters have been detected by means of optical probes in riser flows (Manyele et al., 2002; Sharma et al., 2000) using the cluster criteria of Soong et al. (Soong et al., 1993). However, the detection of structures such as clusters is not straightforward and limited to local and sectional measurements. To characterize clusters, whole-field solids volume fraction information is required, which is very hard to gather experimentally in particular using probes.

Riser inlet and outlet configurations have been investigated as well and were shown to have an influence on the gas-solids flow pattern. The particle velocity distributions have been obtained from solids velocity measurements in the bottom and outlet sections of a riser (Pantzali et al., 2015, 2016). The particle flow is observed to be highly disturbed due to the asymmetrical position of both the gas and the Y-shaped solids inlet line (Pantzali et al., 2015). The influence of the Y-shape solids inlet line on the mean radial particle velocity is observed to quickly decay after which the riser flow can be considered as fully developed. The Y-shaped solids inlet line induces both radial and axial particle velocity fluctuations of the same order as the corresponding mean radial and axial particle velocity components. Again, the effect rapidly decays in the radial direction. As the gas-solid flow is approaching the riser outlet deceleration occurs because the flow is forced to change its main direction near the exit of the riser (Pantzali et al., 2016). The influence of a solids side inlet on the flow pattern in a dilute riser was investigated experimentally in a cold-flow pilot riser (De Wilde et al., 2007). In the vicinity of the solids inlet, radial gas–solids mixing is hindered and bypassing of the solids jet occurs, resulting in steep velocity gradients and off-center maxima in the velocity field. Higher gas flow rates and lower solids fluxes allow bypassing to occur in the plane of the solids inlet via the side opposite the solids inlet. Additionally, seven different outlet configurations have been selected to quantify the internal solids circulation (Van der Meer et al., 2000). If the outlet consists of a smooth bend, the internal recirculation becomes more pronounced with increasing radius and can become even more intense than in abrupt T-outlets. The effects of T- and the L-outlet configurations on dilute riser flow have been studied experimentally and computationally (Heynderickx et al., 2011). The position and shape of the outlet vortex, solids hold-up and axial and radial particle velocities near the outlet openings were hardly affected. Despite all studies reported in literature, the effect of inlet and outlet configurations on the hydrodynamic behavior and cluster characteristics is still not clear, such as cluster solids volume fraction and mass flux, cluster occurance and velocity, etc.

For studying clusters a number of numerical simulation techniques have been developed. Tsuo and Gidaspow (Tsuo and Gidaspow, 1990) used a traditional (constant viscosity) two-fluid model (TFM) to study the formation of clusters. The TFM is widely used to simulate gas–solid flows due to its relatively modest computational cost. However, it is reported in literature (Passalacqua et al., 2010) that the application of this model for dilute gas–solid flows is not adequate. For dilute gas–solid flow, when applying TFM, a grid-independent solution can only be obtained at a very (unpractically) fine grid (Passalacqua and Fox, 2011). Efforts were thus made to develop new hydrodynamic models and corresponding solution techniques that facilitate the study of dilute gas–solid flows. Based on the results reported

in literature (Deen et al., 2007), it is evident that the computational fluid dynamics-discrete element method (CFD-DEM) is a very powerful tool to study the details of flow phenomena prevailing in fluidized beds. The CFD-DEM describes the gas phase as a continuum, whereas each of the individual particles is treated as a discrete entity. This model accounts for the gas-particle and particle-particle interactions and has proven to be very useful to generate closure information required in more coarse-grained models.

The objective of this work is to study the influence of different particle inlet and outlet configurations on riser hydrodynamics associated cluster characteristics, by performing a thorough comparison with experimental data and full 3D simulation results. We employ two CFD-DEM codes: an open-source package OpenFOAM-CFDEM-LIGGGHTS and an in-house CFD-DEM code. The riser flow structure is characterized by utilizing cluster detection algorithms. In this paper, a full comparison between two series of simulation results will be performed to discuss which CFD-DEM code produces a better performance to characterize the hydrodynamic behavior and cluster properties under different operating conditions. The hydrodynamic behavior at different gas superficial velocities is analyzed in terms of axial and cross-sectional profiles of time-averaged solids volume fraction and mass flux. Furthermore, a description of cluster related parameters will be reported. The pros and cons of the outlet and inlet configuration are discussed by comparing their outcomes with full-field experimental data (Varas et al., 2017).

3.2   Numerical method

The CFD-DEM was originally developed simultaneously by Tsuji et al. (1993) and Hoomans et al. (1996). In CFD-DEM the gas phase is described by the volume-averaged Navier-Stokes equations. The continuity equation for the gas phase is given by:

$$\frac{\partial \left(\varepsilon_g \rho_g \right)}{\partial t} + \nabla \cdot \left(\varepsilon_g \rho_g \mathbf{u}_g \right) = 0 \tag{3.1}$$

whereas the momentum equation of the gas phase is given by:

$$\frac{\partial \left(\varepsilon_g \rho_g \mathbf{u}_g \right)}{\partial t} + \nabla \cdot \left(\varepsilon_g \rho_g \mathbf{u}_g \mathbf{u}_g \right) = -\varepsilon_g \nabla P_g - \nabla \cdot \left(\varepsilon_g \tau_g \right) - \mathbf{S}_p + \varepsilon_g \rho_g \mathbf{g} \tag{3.2}$$

where $\mathbf{S}_p$ represents the sink term for momentum transfer between the gas and particle phase:

$$\mathbf{S}_p = \frac{1}{V_{cell}} \sum_{i=0}^{N_p} \frac{\beta V_p}{1 - \varepsilon_g} \left(\mathbf{u}_g - \mathbf{v}_p \right) D \left(\mathbf{r} - \mathbf{r}_p \right) \tag{3.3}$$

where the function D is the distribution function used to distribute the force exerted by the particles on the gas phase in the Eulerian grid cell with volume V_{cell}. The inter-phase momentum transfer coefficient β is evaluated by the Beetstra drag model (Beetstra et al., 2007):

$$F_{drag} = \frac{\beta d_p^2}{\mu} = 10 \frac{1 - \varepsilon_g}{\varepsilon_g^2} + \varepsilon_g^2 \left(1 + 1.5 \sqrt{1 - \varepsilon_g} \right) + \frac{0.413 \text{Re}}{24 \varepsilon_g^2} \frac{\left(\frac{1}{\varepsilon_g} + 3 \varepsilon_g \left(1 - \varepsilon_g \right) + 8.4 \text{Re}^{-0.343} \right)}{\left(1 + 10^{3\left(1 - \varepsilon_g \right)} \text{Re}^{-\frac{1}{2}\left(1 + 4\left(1 - \varepsilon_g \right) \right)} \right)} \tag{3.4}$$

where $\text{Re} = \varepsilon_g \rho_g |\mathbf{u}_g - \mathbf{v}_p| d_p / \mu_g$ is the particle Reynolds number.

The solids phase is described by solving Newton's second law for each particle in the system:

$$m_p \frac{d^2 \mathbf{r}_p}{dt^2} = -V_p \nabla p + \frac{\beta V_p}{1 - \varepsilon_g} \left(\mathbf{u}_g - \mathbf{v}_p \right) + m_p \mathbf{g} + \mathbf{F}_c \tag{3.5}$$

$$I_p \frac{d\omega_p}{dt} = \tau_p \tag{3.6}$$

In these equations τ_p represents the torque and I_p the moment of inertia, which for spherical particles with radius R_p is equal to $I_p = \frac{2}{5} m_p R_p^2$. The particle collisional forces are deterministically computed by means of a soft sphere linear spring-dashpot model that was

firstly proposed by Cundall (Cundall and Strack, 1979). The torque follows from the cross product of the tangent of the collision and the tangential force, multiplied the radius of the particle. The tangential force is the minimum of the tangential spring force and the sliding limit which is a friction factor times the normal force.

3.3   Simulation conditions

The dimensions of the simulation domain correspond to the experimental pseudo-2D riser plus the lateral outlet, which amount to $1.57 \times 0.07 \times 0.006$ meters as shown in Figure 3.1(a). In the experimental riser the outlet of the system is connected to a cyclone, where the gas-solid separation takes place. Glass beads were fed from a storage vessel via a dosage slit with a 70×6 mm opening at an axial position of 70 mm above the gas distributor of the riser. Figure 3.1(b) is a schematic representation of the riser, which is 70 mm in width and 1.5 m long. The top section is a 90-degree, quarter circle bend.

At the initial state there are 50,000 particles packed at the bottom of the riser reactor. Gas is uniformly injected from the riser bottom and new particles are inserted to the reactor at a constant solids mass flux. Both the gas and particles travel through the riser, reach the lateral top region and are removed from the system.
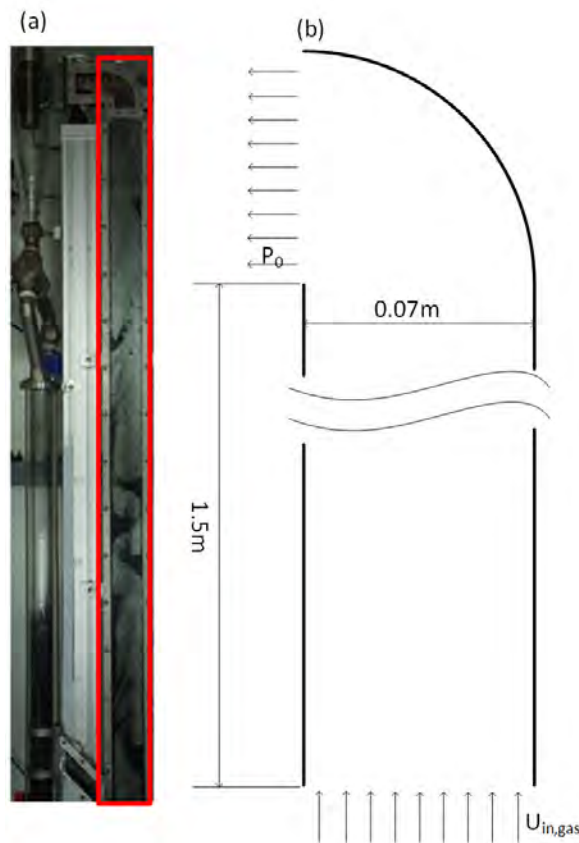
Fig. 3.1 (a) Snapshot of experimental setup; the riser section is indicated by the red box (Varas et al., 2017). (b) Schematic of the pseudo-2D riser in CFD-DEM model.

The insertion of particles was only accepted when there was no particle overlap. The simulations were performed for the fast fluidization regime at several gas superficial velocities
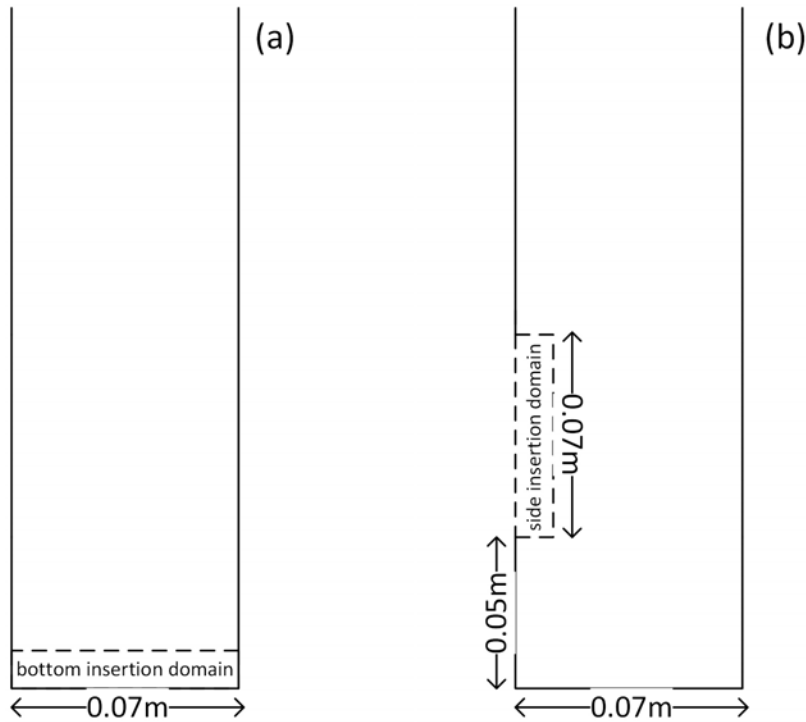
Fig. 3.2 Inlet configuration of the riser: bottom inlet (a), side inlet (b).

$U_{g,in}$ = 5.55, 5.95, 6.35, 6.74 m/s and a fixed solids mass flux of 32 kg/m^2/s. Note that with a fixed solids flux, the total solids holdup in the riser changes depending on experimental conditions and in the simulations on the definition of inlet and outlet geometry. The particles were inserted employing two different geometries: bottom inlet (Figure 3.2a) and side inlet (Figure 3.2b). The side inlet geometry corresponds to the experiments, while for the bottom inlet geometry the particles were inserted at random positions of the bottom X-Y plane of the simulation domain at a very low velocity (0.01 m/s). The particles that reach the lateral outlet leave the simulation domain.

At all walls, no-slip boundary conditions were applied. With a prescribed inflow axial velocity equal to $U_{g,in}$, gas was supplied at the bottom of the domain. The left side of the domain was subdivided into two regions: for the top-left outflow region of 0.07 m the pressure P_0 is prescribed and at the bottom left side the boundary condition is applied separately depending on the applied particle insertion configuration as illustrated in Figure 3.2. When a bottom-inlet configuration was used for the particles, the lower left side of the domain was described as a wall, i.e. by no-slip boundary conditions. When a side inlet configuration was used, free-slip boundary conditions were applied at the particle insertion opening, while outside this region no-slip conditions were applied. For the lateral outlet of the riser two different geometries will be considered: a smooth lateral wall (Figure 3.3a) and a rough
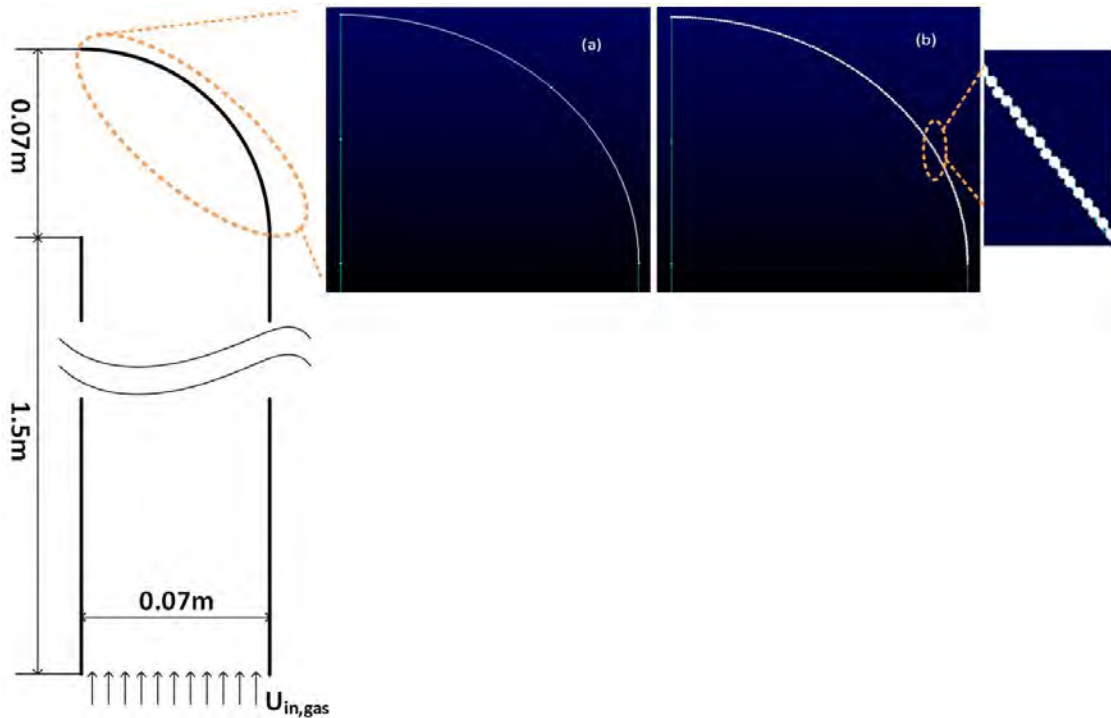
Fig. 3.3 Outlet configuration of the riser: smooth outlet (a), rough outlet (b).

lateral wall (Figure 3.3b). The smooth geometry corresponds with the experimental lateral outlet and no-slip boundary conditions were applied. The rough geometry is described with a fixed curved wall made of particles placed at the top of the simulation domain. This mimics the lateral curved outlet of the experimental unit.

According to studies of Wang et al. (2009) the grid size should be 2-4 particle diameter to obtain quantitative agreement between TFM and DPM results. The mesh size (in the width and height directions) is set around 3 times the particle diameter. The mesh number is chosen to be four in the depth direction, two cells to account for the boundaries and two to describe the gas flow, because one cell was not enough to capture the gas-particle flow. More details about the simulation and experimental settings and physical parameters used are specified in Table 3.1.

The total simulation time was 20 seconds. In the post-processing the first 10 seconds were discarded to exclude start-up effects. Beyond 10 seconds, a pseudo steady state was attained. Simulation data were collected each 0.01 seconds.

3.3.1   Numerical setup

Because two different numerical codes are used it is prudent to discuss the differences here. These differences consist of differences in numerical schemes for solving the volume

Table 3.1 Experimental (Varas et al., 2017) and simulation settings

	Exp.	Side Inlet	Bottom Inlet	Oulet
Gas density (kg/m^3)	1.2	1.2	1.2	1.2
Gas viscosity (kg/m·s)	1.8×10^{-5}	1.8×10^{-5}	1.8×10^{-5}	1.8×10^{-5}
Particle density (kg/m^3)	2500	2500	2500	2500
Particle diameter (mm)	0.8-0.9	0.85	0.85	0.85±0.05
Normal coefficient of restitution (particle-particle)	-	0.96	0.96	0.96
Normal coefficient of restitution (particle-wall)	-	0.86	0.86	0.86
Tangential coefficient of restitution	-	0.33	0.33	0.33
Friction coefficient	-	0.15	0.15	0.15
Normal spring stiffness (N/m)	-	1600	1600	1600
Solids mass flux (kg/m^2/s)	32	32	32	32
Solids inlet velocity horizontal(m/s)	-	0.00717	0	0
Solids inlet velocity vertical(m/s)	-	-0.00717	0.01	0.01
Width of the riser (m)	0.07	0.007	0.07	0.07
Depth of the riser (m)	0.006	0.006	0.006	0.006
Height of the riser (m)	1.57	1.57	1.57	1.57
Cell size (m^3)	-	0.0025×0.0015 ×0.0025	0.0025×0.0015 ×0.0025	0.0025×0.0015 ×0.0025

averaged Navier-Stokes equation and Newtons equations and the interpolation schemes for solids volume fraction. The settings for the physical parameters used in above equations are the same which holds for the numerical timesteps for the CFD and DEM parts, which are respectively 10^{-4} and 10^{-5} s.

The details of the numerical solution methods for the in-house code can be found in Patil et al. (2014). This method is a semi-implicit solution method. The CFDEM code follows the description provided by Goniva et al. (2012). Newtons equations for the particle phase are solved using a simple first order explicit integration. This in contrast to the Crank Nicolson scheme that is used in the CFDEM code. Both the differences in numerical solution are

estimated to have little effect on the results. Mostly since the tolerances in the two codes are similar. For the collisions the accuracy is dependent on a combination of timestep, integration scheme and spring-stiffness. At the given parameters these are not expected to give reason to differences in results.

The most prominent difference is in the scheme for the communication between the two phases of the void fraction. In the in-house code this is handled using an interpolation scheme using a smoothed dirac delta function. Whereas in CFDEM this is handled with a subdivision method for each particle. The accuracy of both of these methods is related to the choice of cell size relative to the particle diameter, which in these simulations is the same.

3.3.2 Cluster detection

The pseudo-2D fast fluidized riser is characterized by a dense bottom zone and a dilute region at the top, leading to solids fluctuations along the riser domain. Both in experiments and simulations clusters are defined as connected regions with local solids fractions larger than 0.2 everywhere that have a minimum area of 60 mm^2 and a dense core with at least one grid with local solids fraction larger than 0.4 (Carlos Varas et al., 2016). The area of 60 mm^2 corresponds to an equivalent circle diameter of 8 mm. The detection of clusters was performed by post-processing simulation data by means of a Matlab script. We have chosen to maintain the same definitions to stay as close as possible to the original methodology as in the experiments. Cluster frequency or occurance is therefore also defined as the number of clusters found in a single image at any given time instant.

Clusters can be observed in Figure 3.4. Green ellipses correspond to clusters moving upwards, while red ones move downwards. It is noted that dense clusters are formed close to the wall and tend to fall down, while dilute strands of particles tend to move upwards.
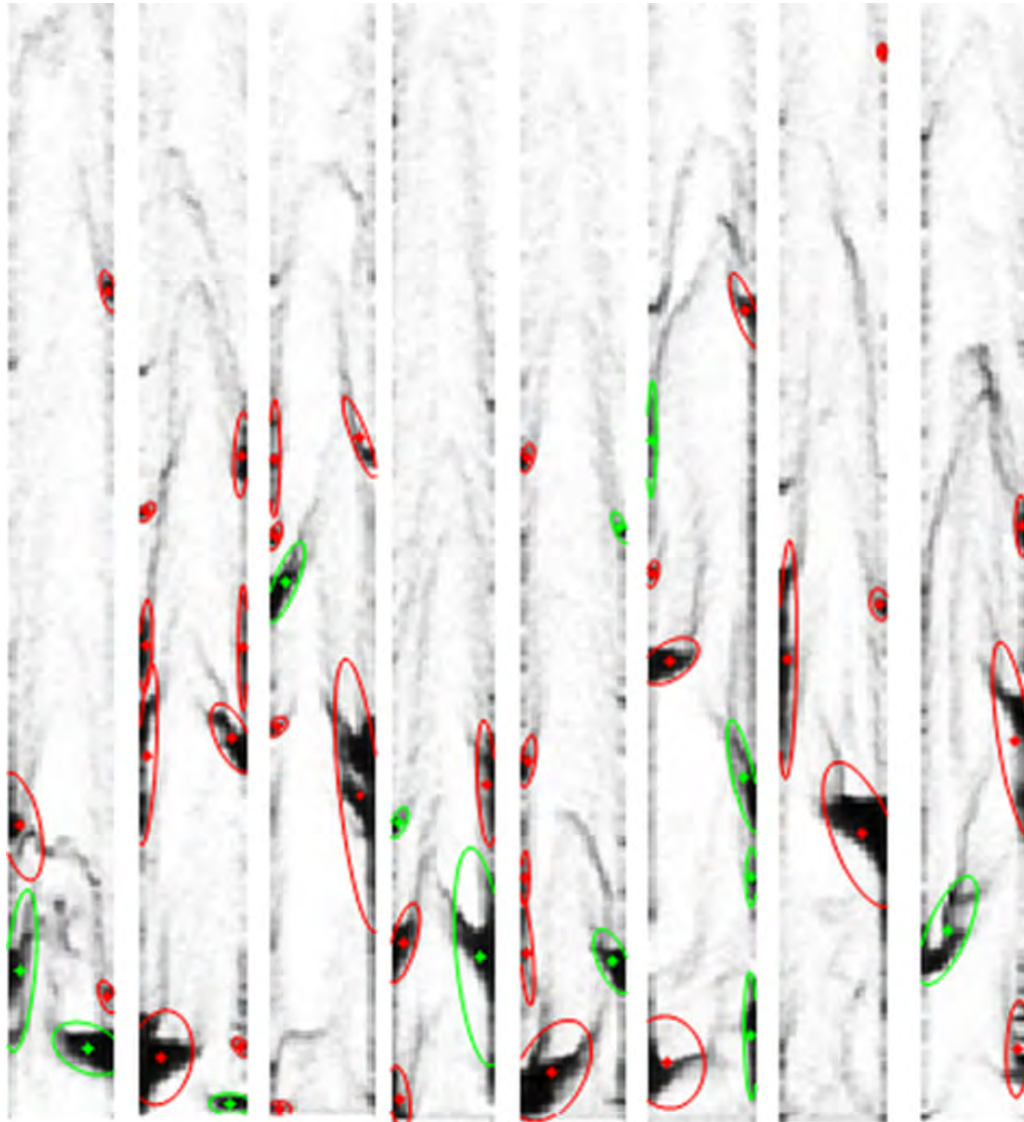
Fig. 3.4 Snapshots of the detected clusters from solids fraction field of CFD-DEM simulations at different times. Here, the bottom half of the riser is shown where the clusters are most prevalent.

3.4 Results and discussion

3.4.1 Effect of inlet configuration

In this subsection we display an example of full-field simulation data for two different inlet configurations. Figure 3.5(a) shows snapshots of the void fraction of the whole riser. Snapshots of particle axial velocities corresponding to the bottom inlet and side inlet configurations are shown in Figure 3.5 (b) and (c) respectively. The different inlet configurations influence the collisions between particles and between particles and the wall. For the side inlet configuration there are more particles in the bottom region leading to more collisions, which implies that the effect of the inlet configuration matters.
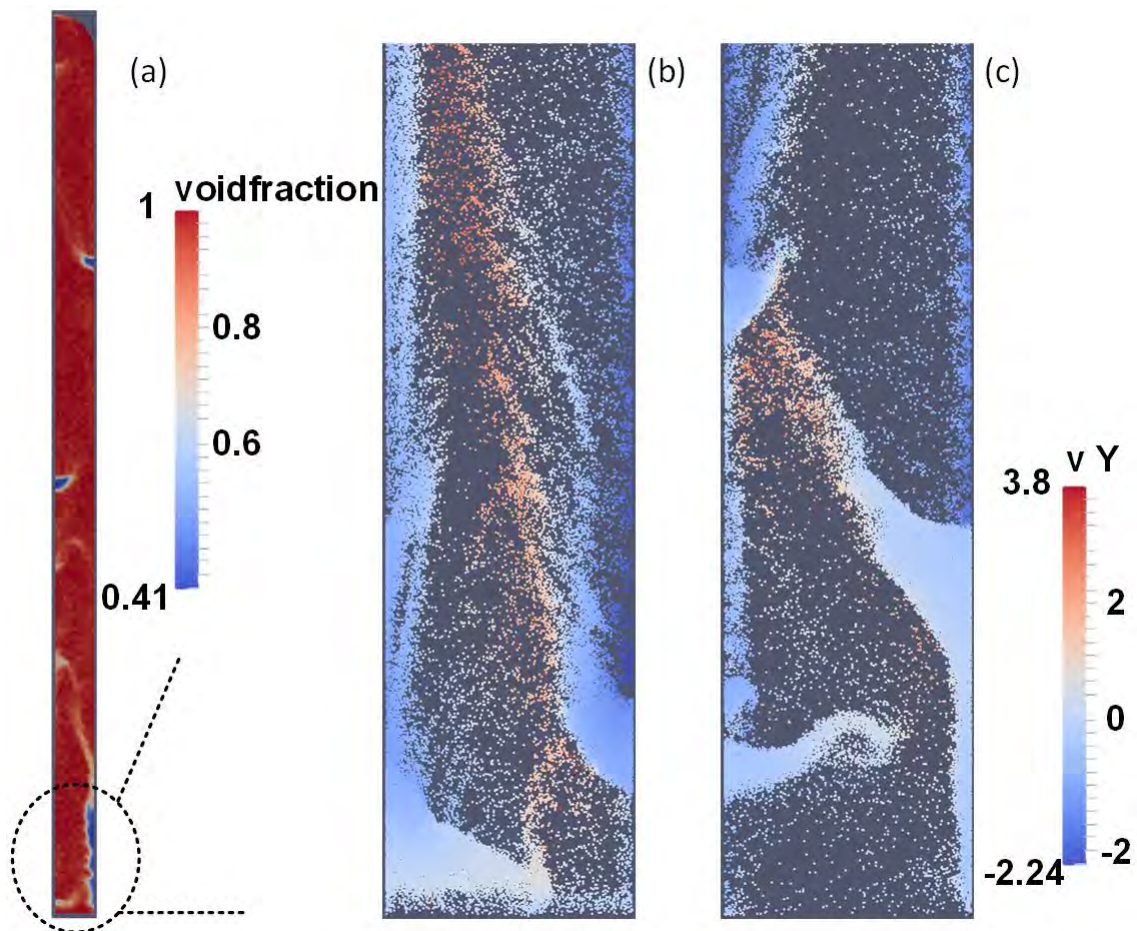
Fig. 3.5 Snapshots of solids distribution: total riser (a), bottom inlet (b), side inlet (c).

Axial profiles of time-averaged solids volume fraction are obtained from our CFD-DEM simulations at different superficial velocities and are compared with experimental data as well as simulation data obtained from our in-house code. From Figure 3.6 it can be seen that
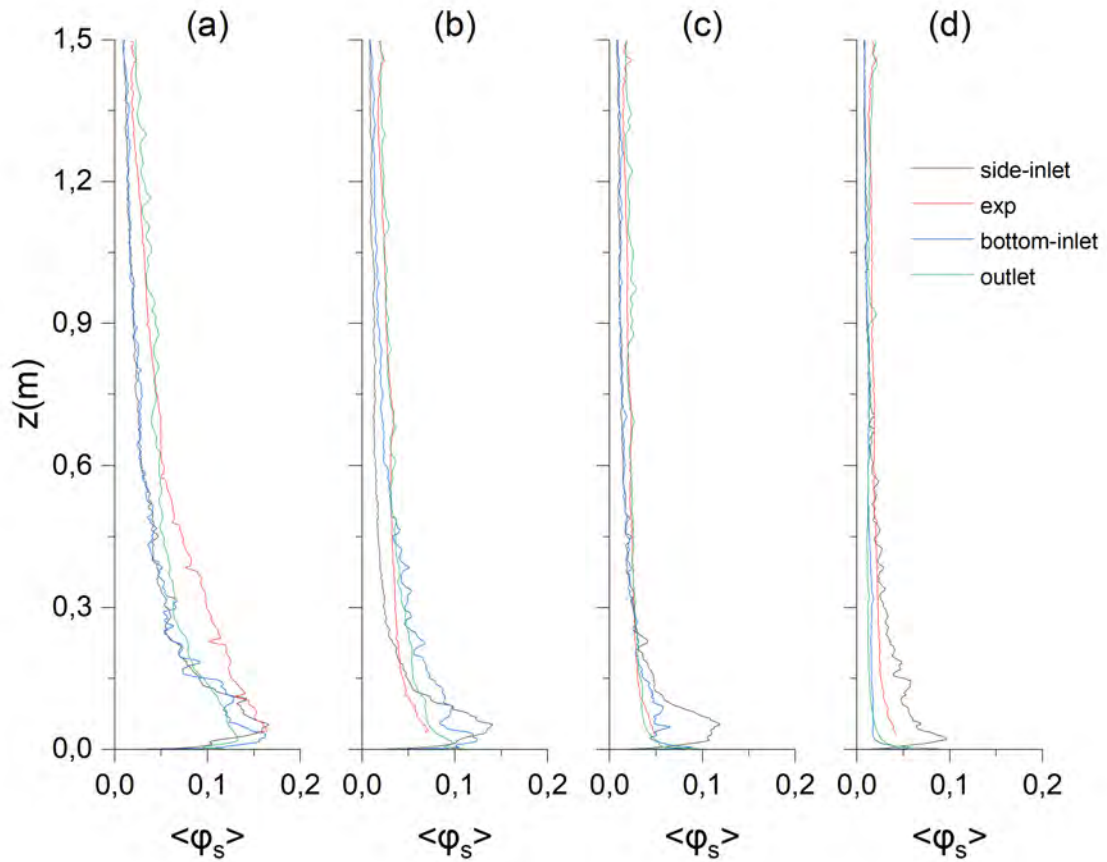
Fig. 3.6 Axial profiles of time- and laterally -averaged solids holdup. (a) $U_{g,in}$=5.55 m/s, (b) $U_{g,in}$=5.95 m/s, (c) $U_{g,in}$=6.35 m/s, (d) $U_{g,in}$=6.74 m/s.

all four sets of data possess the same features namely that the riser reactor has dense regions at the bottom and dilute zones at the top. At higher gas superficial velocities, a much denser bottom region is observed for the simulation with side inlet in comparison to the experiments and the simulation with bottom inlet.

Note that in all simulations the particle insertion velocity is maintained at a constant value of 0.01 m/s. In reality, the introduction of the particles in the riser system is abrupt where the particle insertion velocity would be affected by changes in superficial gas velocity. At high $U_{g,in}$ the pressure at the riser side would be high and consequently less particles would enter with a lower velocity. In the simulations the particle insertion velocity is constant, resulting in more collisions between particles at higher gas superficial velocity and consequently more particles residing in the dense region.

Fig. 3.7 Cross-sectional profiles of time-averaged solids volume fraction at three lower heights: Height=0.1 m, 0.3 m, 0.5 m (left to right) and different superficial gas velocity: $U_{g,in}$=5.55 m/s, 5.95 m/s, 6.35 m/s, 6.74 m/s (from top to bottom).

Fig. 3.8 Cross-sectional profiles of time-averaged solids mass flux at three lower heights: Height=0.1 m, 0.3 m, 0.5 m (left to right) and different superficial gas velocity: $U_{g,in}$=5.55 m/s, 5.95 m/s, 6.35 m/s, 6.74 m/s (from top to bottom).

To complete the validation of the CFD-DEM model for different inlet configurations, in Figure 3.7, the cross-sectional profiles of solids volume fraction at the three lower axial positions (Height = 0.1, 0.3, 0.5 m) are compared at four different superficial gas velocities. It can be seen that for all four operating conditions the solids volume fraction attains the typical U-shaped profile. The (average) solids volume fraction decreases significantly with increasing axial coordinate, which corresponds to the fact that the bottom region of the riser is much denser than the top section as evident from Figure 3.6. The U-shaped profiles possess a more symmetric solids holdup profile at lower $U_{g,in}$. A further increase of the inlet gas velocity to 6.74 m/s, shown in the last row of Figure 3.8, results in a higher solids volume fraction in the annular region for the side inlet in comparison with the other three sets of experimental and simulation results. This most likely is due to the fact that the lateral particle insertion velocity was kept constant at the different operating conditions.

At lower $U_{g,in}$, all three sets of simulation results show a strong solids down-flow in the annular region at lower axial coordinates in the vicinity of the region with the side inlet. At a higher gas superficial velocity of 6.74 m/s, only the system with the side inlet configuration exhibits strong down-flow close to the left wall which is in accordance with our observations.

As can be seen in Figure 3.9, the riser system becomes quite dilute at these high axial positions. The open-source simulation produces lower solids volume fractions in comparison with the experimental data and results obtained from the in-house code. This is in accordance with the observations from Figure 3.6. This difference is unexpected because the governing equations and the closures for the fluid-particle and particle-particle interaction are essentially the same.

3.4.2 Effect of outlet configuration

The effect of surface roughness of the outlet top wall, respectively shown in Figure 3.2 (a) and (b), will be reported in this section. Note that the OpenFOAM-LIGGGHTS has a smooth outlet, whereas our in-house code has a surface roughness.

Cross-sectional profiles of the time-averaged solids mass flux are shown in Figure 3.10. At low gas velocity, the four sets of experimental and simulation profiles are in reasonable overall agreement. However, the simulation results obtained for the outlet condition, exhibit more asymmetric profiles in comparison with the other three sets of results. The asymmetric behavior becomes more noticeable at high gas velocities. When the superficial gas velocity increases, the CFD-DEM open-source simulation results exhibit lower and more symmetric profiles in comparison with the experimental profiles. Furthermore, the two inlet conditions show relatively larger deviations at higher superficial gas velocities, while the outlet condition seems to overestimate the solids mass flux for low superficial gas velocities and higher in the
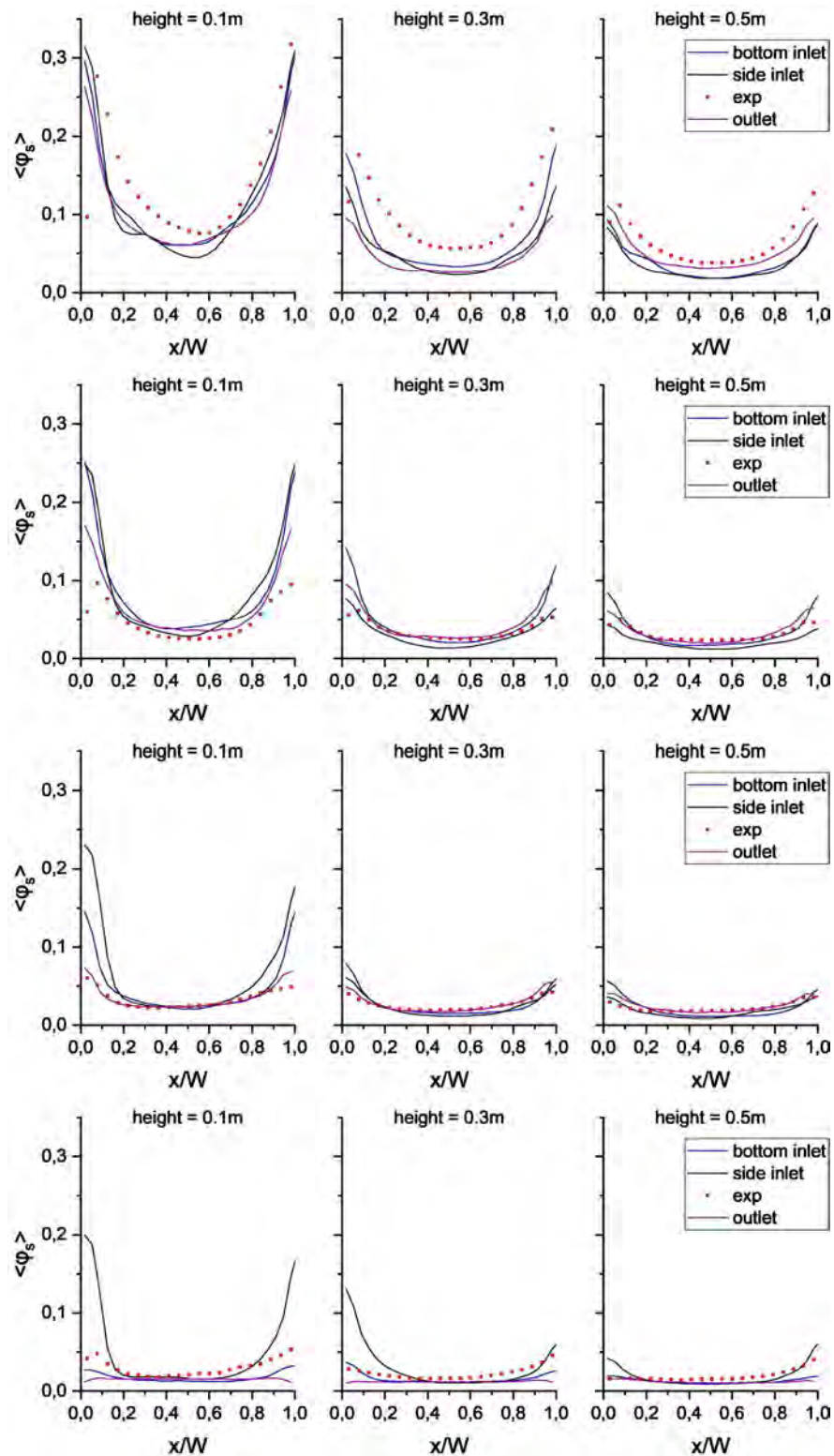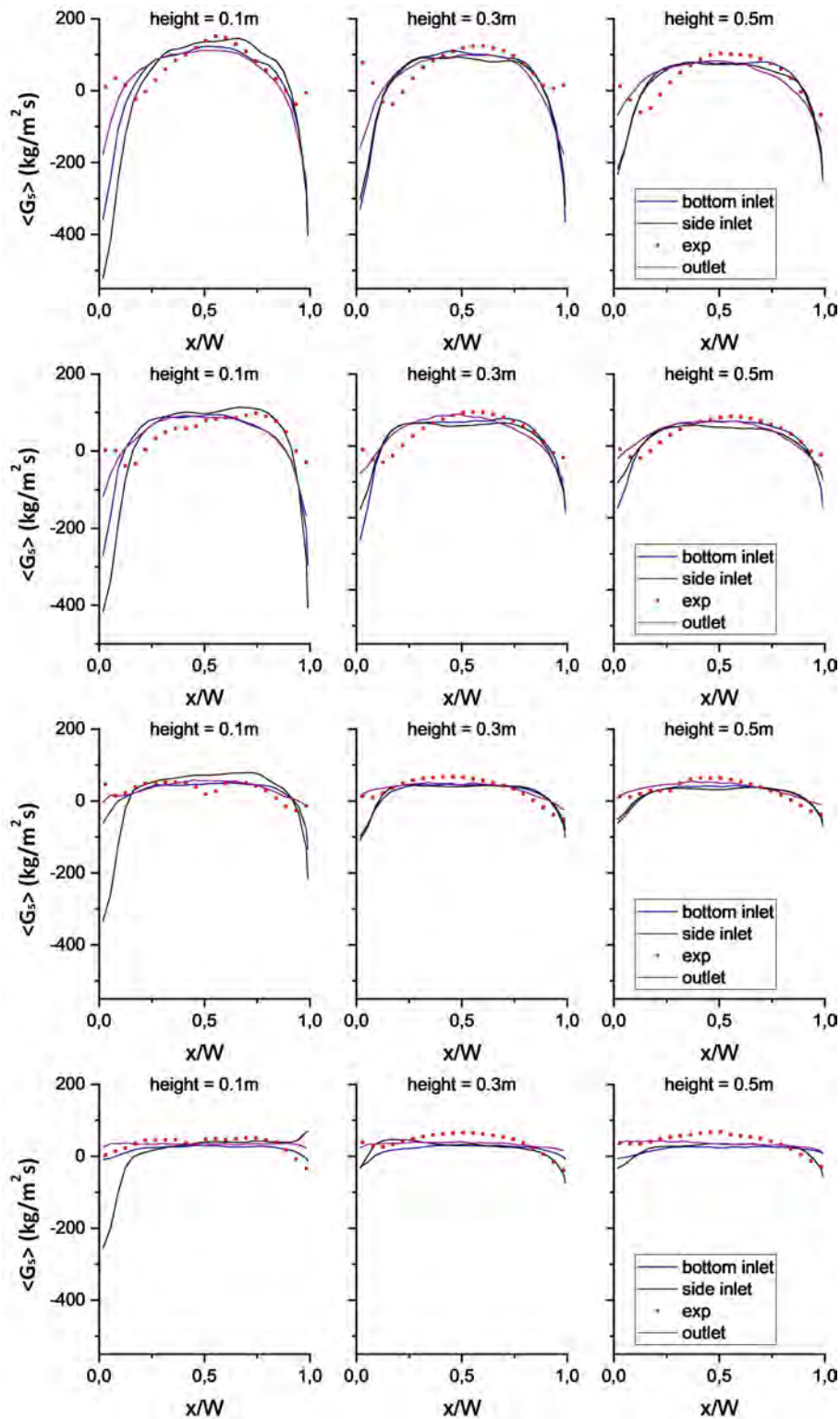
Fig. 3.9 Cross-sectional profiles of time-averaged solids volume fraction at three higher heights: Height=1.0 m, 1.2 m, 1.4 m (left to right) and different superficial gas velocity: $U_{g,in}$=5.55 m/s, 5.95 m/s, 6.35 m/s, 6.74 m/s (from top to bottom).

riser. In both cases the maximum difference can be up to more than 50% of the maximum flux.

From Figure 3.9 and 3.10 it can be seen that no obvious difference exists between side and bottom inlet results. We conclude that different inlet configurations do not have a significant influence on the hydrodynamics in the top region of the riser, which matches our expectations.

3.4.3   Cluster analysis

Clusters were detected in the entire riser region according to the method explained in the previous section. The main focus will be on the predictive capability of the cluster characterisitics between the different inlet and outlet conditions. The cluster-related properties are reported for qualitative analysis.

In Figure 3.11, we perform the core-wake cluster detection and quantify the cluster frequency of occurance. All the experimental data and simulation results show that clusters are mostly located close to the walls irrespective of the gas superficial velocity. This matches the so-called core-annulus flow pattern in risers. The cluster frequency is highly influenced by the superficial gas velocity with larger amount of clustering at lower superficial gas velocity. This can be explained by the fact that the average holdup increases significantly with increased dissipative particle-particle collisions promoting clustering. At $U_{g,in} = 5.55$ m/s, it is found that in comparison with the computational results, clustering is more pronounced in the experiments. However at a superficial gas velocity of 6.35 m/s, the cluster frequency of occurance obtained from the experiment is much smaller than its counterpart obtained from the simulations.

The fluidized bed reactor is governed by an excess amount of gas on top of minimum fluidization (u_{mf}). Any excess gas on top of that usually goes into bubbles, which is the bubbling bed regime, up to 2-5 times u_{mf}. After that particles are carried further and further until a riser regime emerges and eventually pneumatic conveying is reached. The latter is governed by the terminal settling velocity (Schiller-Neumann). For the particles in this study, the minimum fluidization velocity is 0.52 m/s and the terminal velocity is 6.71 m/s. This means that at the highest background velocity the system is at or around the terminal velocity. The particles in that system are highly suspended and less likely to form clusters as is also clear from the experiments.

In the simulations the amount of drag is governed by the drag correlation, in this case the so-called Beetstra drag correlation. These drag correlations cover the entire range of velocities and solids fractions but are known to have some difficulty near minimum fluidization and near high Re numbers and low solids fractions (high porosity). In short near the terminal
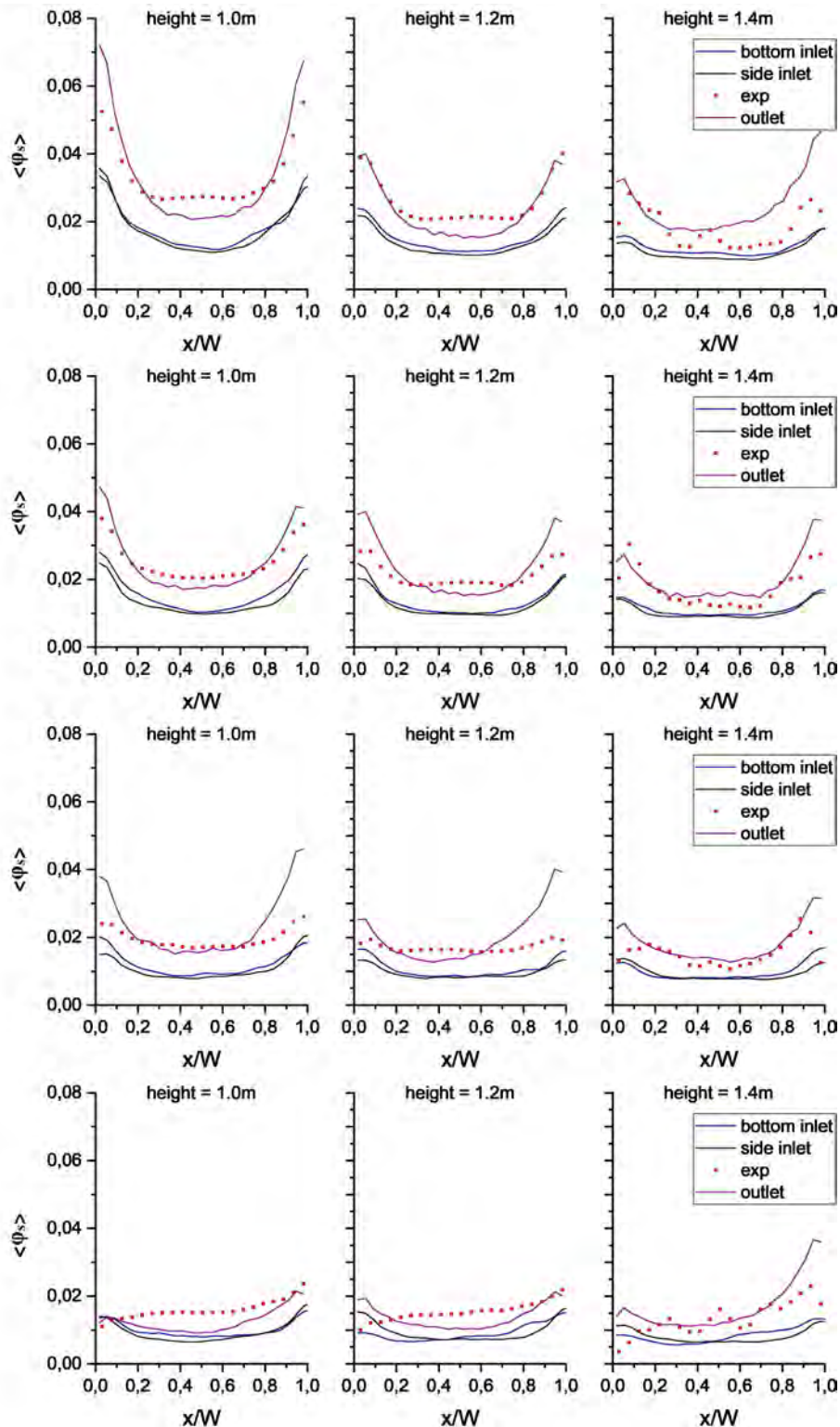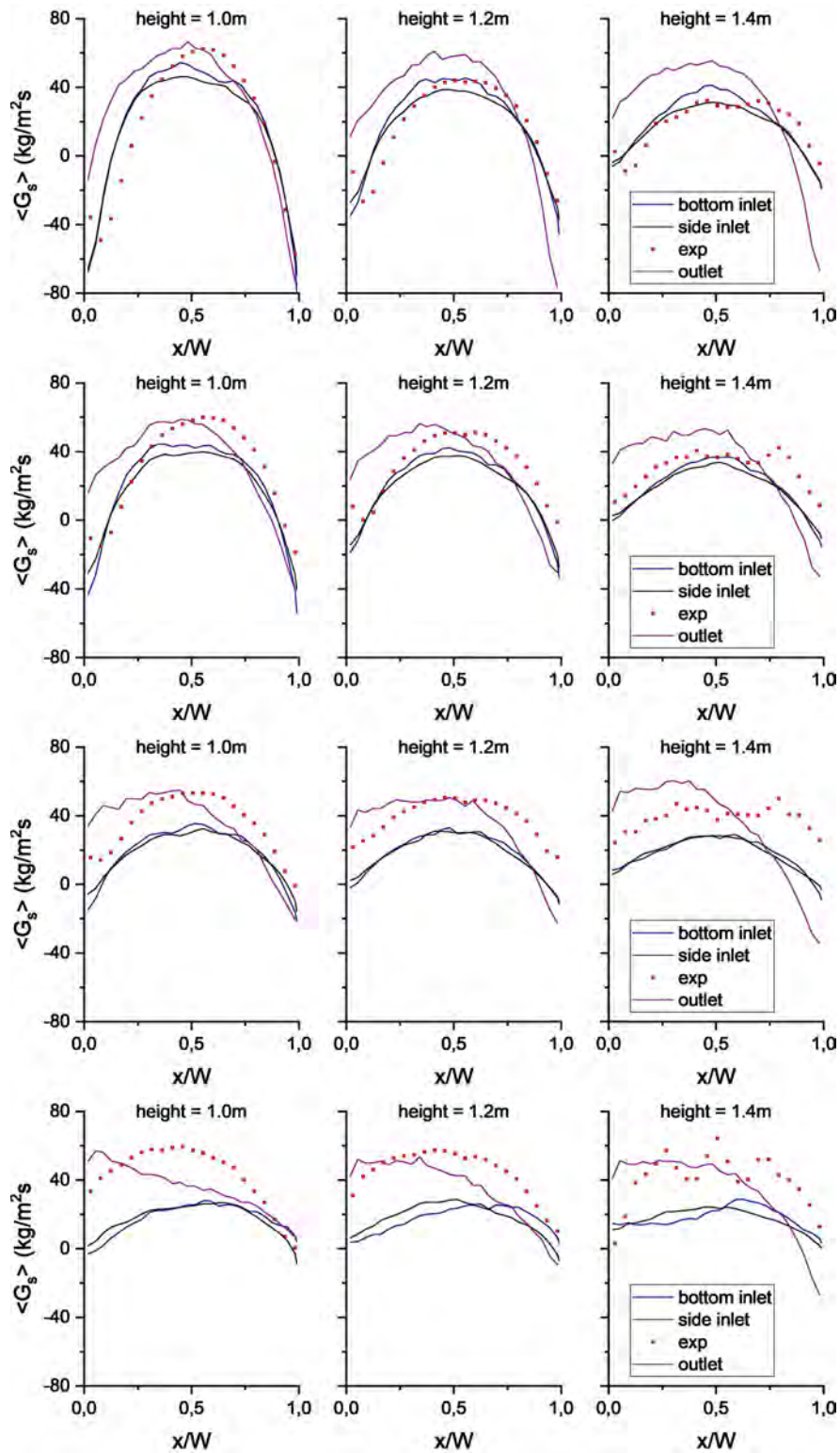
Fig. 3.10 Cross-sectional profiles of time-averaged solids mass flux at three higher heights: Height=1.0 m, 1.2 m, 1.4 m (left to right) and different superficial gas velocity: $U_{g,in}$=5.55 m/s, 5.95 m/s, 6.35 m/s, 6.74 m/s (from top to bottom).

velocity these drag correlations are not always performing very well, which means that such a transition from riser to more pneumatic conveying can be difficult to predict exactly.
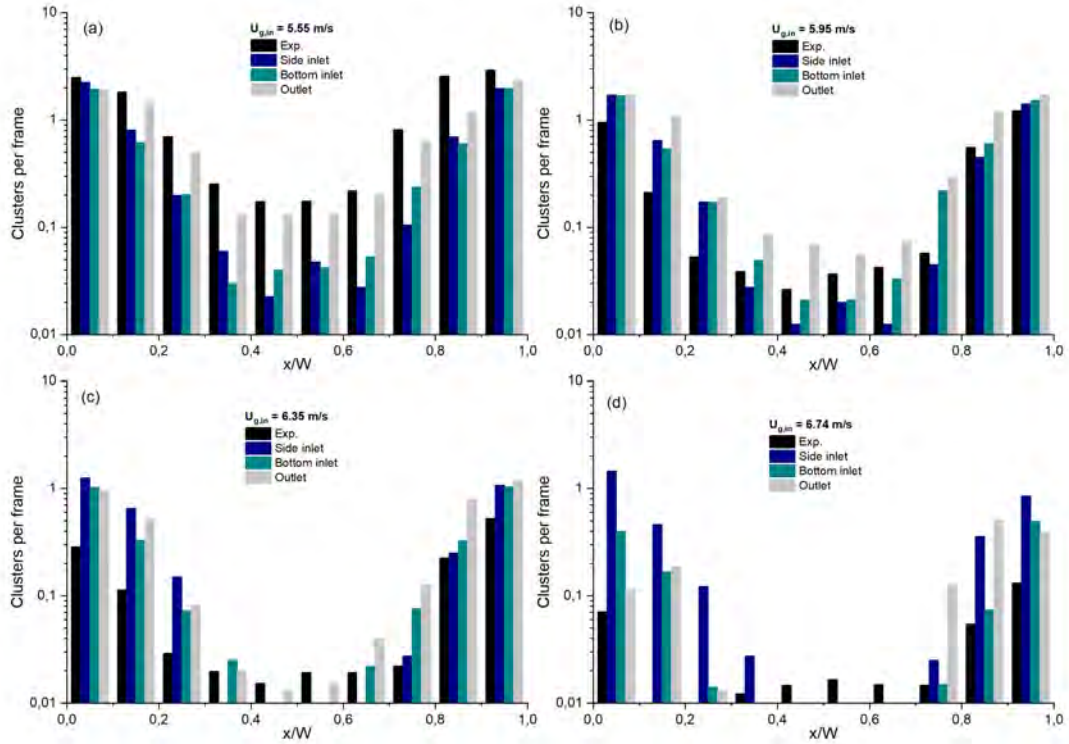
Fig. 3.11 Cluster occurance as function of background superficial gas velocity, for the experiments, side-inlet, bottom-inlet and outlet conditions.

Subsequently the cluster analysis will be carried out in more detail for a relatively low gas superficial velocity $U_{g,in}$ = 5.95 m/s.

First the mean solids volume fraction of each cluster is computed for the corresponding cells which are occupied by the identified cluster. Therefore the averaged cluster interal solids holdup is calculated from the following expression:

$$\varphi_{cluster} = \frac{\sum \varphi_s}{\sum N_{cells,occupied}} \tag{3.7}$$

In Figure 3.12, the experimental and computed cluster solids volume fraction are plotted versus the cluster centroid locations in the horizontal direction. As can be seen, there are more clusters close to the walls, whist the dilute cluster distribution in the core region can not be ignored.

Better agreement between experiments and simulation data is obtained from the in-house code, which uses the rought outlet conditions, close to the walls whereas the open source code produces better agreement with the experiments in the center of the riser. The cluster

formation is characterized by collisions between particles moving upwards and downwards. Solids velocities are high in the center of the riser, hence cluster prevalence in this region is relatively low and should be taken into account to quantify cluster characteristics. All simulation results show that dense clusters have a tendency to move to the center region of the riser, whereas the clusters are uniformly distributed close to the walls according to experimental observations. This might be caused by the fact that the central region, where particles are moving upwards (Figure 2.12), is narrower in comparison with the one observed in the experiments (Varas et al., 2017). Clusters originate from collisions between particles moving upwards and downwards, which implies that dense clusters are formed in regions where most of the particle collisions occur.
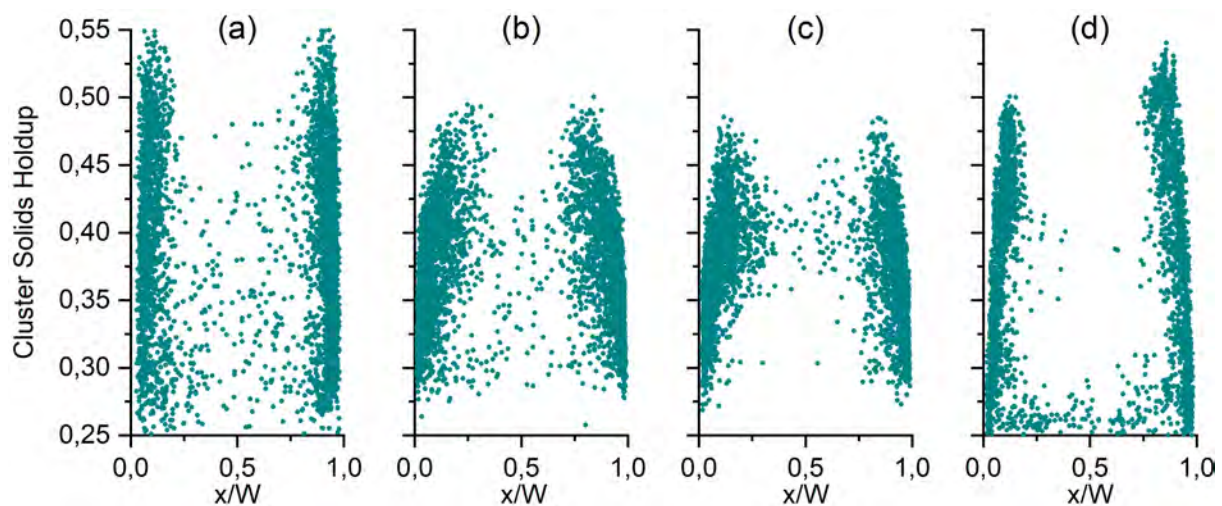
Fig. 3.12 Cluster solids holdup vs centroid location: (a) experiment, (b) side inlet, (c) bottom inlet, (d) outlet. $U_{g,in}$=5.95 m/s.

In Figure 3.13 a couple of snapshots are presented showing the distributions of particle velocities in the axial direction. It is clear that particles are traveling downwards in the annular region and upwards in the core of the riser. The particle motion features one upward moving cluster in the core region and two downwards moving clusters close to the left wall, one near the top of the image and one near the bottom. Figure 3.14 shows the experimental and simulated cluster velocity distribution at a superficial gas velocity $U_{g,in}$ = 5.95 m/s. The typical core-annulus flow is seen here, with mostly downflowing clusters near the wall, and only upflowing clusters in the center. The description of cluster motion for the simulations with the side inlet show a good cooorespondence with experimental data, with mainly downwards moving clusters close to the walls whilst clusters in the core region are moving upwards. These observations are in accordance with Figure 3.12. It can also be seen that cluster velocity profiles shown in Figure 3.14 (c) and (d) possess a more symmetric

distribution. This is explained by the more uniform upward motion from the bottom of the riser with the bottom inlet. The result reveals that the open-source package has a better performance with respect to prediction of cluster velocities, considering the narrow cluster velocity distribution presented in Figure 3.14(d). In addition, different particle insertion configurations have a strong impact on the cluster velocity distribution.
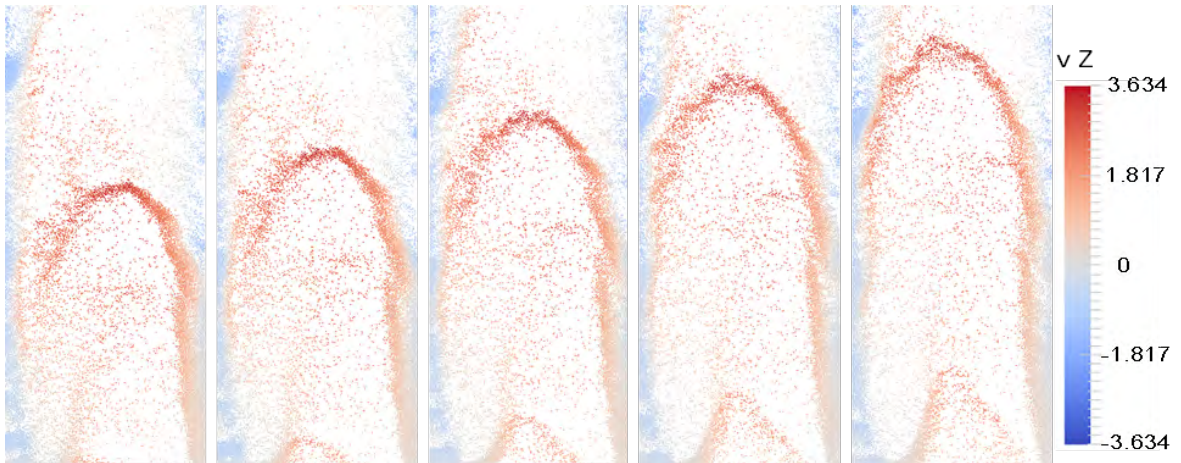
Fig. 3.13 Snapshot gradations of upward and downward moving patterns of clusters. $U_{g,in}$=5.95 m/s.
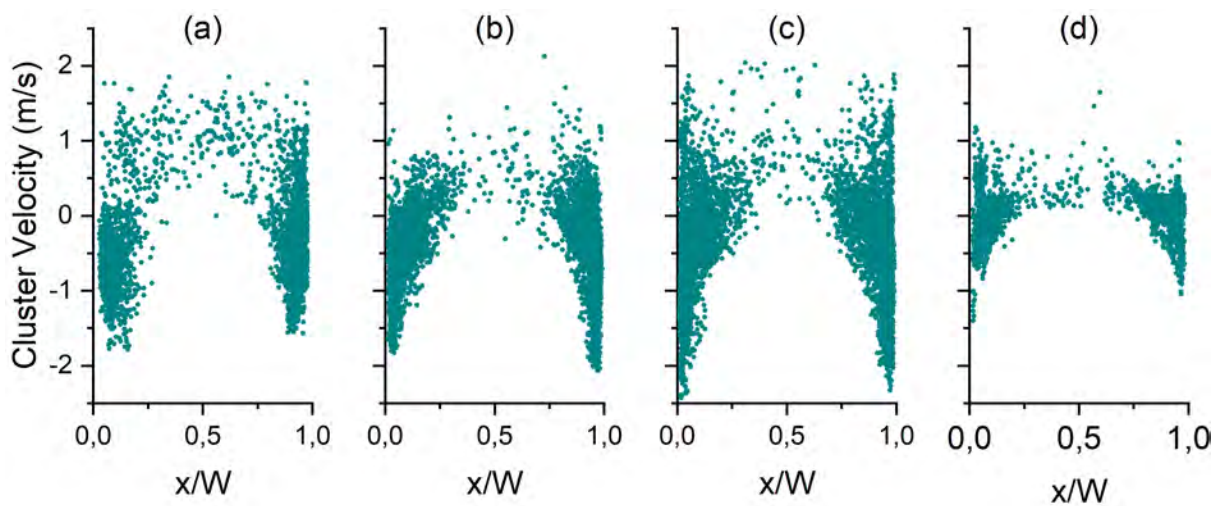
Fig. 3.14 Cluster velocity: (a) experiment, (b) side inlet, (c) bottom inlet, (d) outlet. $U_{g,in}$=5.95 m/s.

3.5 Conclusion and recommendation

In this work, the influence of solids inlet and lateral top configurations and gas superficial velocity on the hydrodynamic behavior and cluster phenomena is investigated computationally in a cold-flow pseudo-2D fluidized riser. A comparison between experimental data and full 3D simulation results obtained from two different CFD-DEM codes is presented.

The axial profiles of solids volume fraction provide quantitative information on the particle distribution. The riser reactor has dense regions at the bottom and dilute regions at the top. With increasing gas superficial velocity, a much denser bottom region is achieved from side inlet simulation data in comparison to experimental and bottom inlet simulation results. Firstly, at three low axial locations the cross-sectional solids volume fraction and mass flux are presented to quantify the impact of particle insertion on flow pattern evolution. The time-averaged solids volume fraction is significantly higher at low axial coordinates. A U-shaped solids volume fraction profile is found and higher solids volume fraction in the annular region is observed at high inlet gas velocities with side inlet. The time-averaged solids mass flux strongly depends on gas superficial velocity. At low superficial velocities, the solids motion is characterized by a relatively high solids up-flow in the core region of the riser and a very high down-flow close to the riser walls. The mass flux decreased with increasing superficial velocity. Secondly, two different lateral top boundaries are investigated by examining the flow structure at three axial positions near the exit of the riser. Although the riser system becomes quite dilute at these regions, a relatively low cross-sectional solids volume fraction is observed from the two sets of simulations with differing inlet conditions, whereas the profiles obtained from the simulation with a coarse outlet condition seem to correspond better with the experimental data. For the rough lateral outlet configuration, the solids mass flux is asymmetric and the behavior becomes more pronounced with increasing superficial gas velocities and high axial positions. Differences in solids volume fraction and mass flux for the side and bottom inlet are negligible near the outlet and there we conclude that different inlet configurations do not have a significant influence on the flow pattern near the riser exit.

Furthermore, cluster properties such as frequency of occurrence, average solids volume fraction and velocity were chosen for cluster characterization. All experimental and computational results exhibit the same tendency namely that more clusters exist close to the walls. The cluster frequency of occurance is significantly influenced by the superficial gas velocity. With increasing superficial velocity, there are less clusters formed in the riser. Most clusters are generated close to the walls, whilst presence of clusters in the core region should not be ignored. Clusters are moving predominantly upwards in the central region and downwards in the annular region. Side inlet simulation results show a good correspondence

with experimental data with respect to the description of cluster motion. The cluster velocity is more symmetrical in the case where particles are introduced at the bottom of the riser.

Chapter 4

Scaling Method of CFD-DEM Simulations for Gas-Solid Flows in Risers

[1]

Abstract

In this chapter a scaling method is proposed for scaling down the prohibitively large number of particles in CFD-DEM simulations for modeling large systems such as circulating fluidized beds. Both the gas and the particle properties are scaled in this method, and a detailed comparison among alternative mapping strategies is performed by scaling both the computational grid size and the riser depth. A series of CFD-DEM simulations has been performed for a pseudo-2D CFB riser to enable a detailed comparison with experimental data. By applying the scaling method, the hydrodynamic flow behavior could be well predicted and cluster characteristics, such as cluster velocity and cluster holdups agreed well with the experimental data. For a full validation of the scaling method, four mapping conditions with different ratios of the grid size and particle volume and of modified ratio of riser depth to particle size were analyzed. The results show that in addition to hydrodynamic scaling of the particle and fluid properties, scaling of the dimensions for the interphase mapping is also necessary.

4.1 Introduction

Gas-solid fluidization in riser reactors has received substantial interest as it is widely encountered in numerous industrial processes such as base chemical production, biomass gasification and catalytic cracking (Gómez-Barea and Leckner, 2010; Khan et al., 2014; Shah et al., 2016). The performance of risers has been extensively investigated over the past decades to acquire an in-depth insight of their hydrodynamics (Geldart and Rhodes, 1986; Horio and Kuroki, 1994; Tsuo and Gidaspow, 1990). Risers are usually operated at high superficial velocities under fast fluidization conditions. These systems exhibit a so called "core annulus" flow structure, which is characterized by a dilute solids up-flow in the core of the riser, and a dense down-flow close to the walls (Bolton and Davidson, 1988; Geldart and Rhodes, 1986; Hartge et al., 1988; Horio and Kuroki, 1994; Tsuo and Gidaspow, 1990). The dense regions typically contain particle clusters, where the gas permeability is reduced, which negatively impacts the performance of risers as a chemical reactor. CFD-DEM simulations have the major advantage of having very good predictive capabilities. However in most circulating fluidized beds, the number of particles is in the order of $10^9 - 10^{12}$ which is the biggest bottleneck of these simulations. Such particle numbers would quickly lead to prohibitively long simulation times (months-years). Considering the computational cost, it is desirable to develop an appropriate scaling method to substantially reduce the number of particles by increasing the particle size whilst maintaining the capability to capture main flow features.

For gas-solid flows, Andrews and O'Rourke (1996) proposed the so-called "Multi-Phase Particle-In-Cell" (MP-PIC) approach, which is a parcel-approach and has been widely applied to granular flows (O'Rourke and Snider, 2010; O'Rourke et al., 2009; Snider, 2001). Instead of tracking collisions between particles directly, the MP-PIC employs a simple "particle pressure" model to prevent particles from becoming closely-packed. Patankar and Joseph (2001) explored an Euler-Lagrangian numerical simulation (LNS) scheme for particulate flow, and showed that the parcel approach is able to capture the basic flow features. But this scheme is strictly applicable when collisions do not play a dominant role in the flow behavior, meaning dilute flow. Sakai and Koshizuka (2009) developed a coarse-grained model, which considers the drag force and the contact force. Their model could simulate the 3D plug flow in a horizontal pipeline system accurately but is limited to systems with a small number of calculated particles. The similar particle assembly (SPA) model proposed for large-scale discrete element method simulation was validated in the work of Mokhtar et al. (2012). In their model, particles with similar physical or chemical properties are represented by a single particle. The influence of coarse graining was studied in literature (Bierwisch et al., 2009) and revealed that bulk volume fractions are independent of grain size provided the underlying

forces scale quadratically with the grain diameter. Note that the latter study was restricted to dilute granular systems where only binary collisions occur. Whether the scaling is still valid in the intermediate to dense regimes is not clear. Alternatively, filtered two-fluid models (TFM) have been constructed for coarse-grid simulation (Gao et al., 2018; Milioli et al., 2013; Parmentier et al., 2012; Schneiderbauer and Pirker, 2014). Gao et al. (2018) conducted a comparative evaluation of several model settings to assess the effect of mesoscale solid stress in a coarse-grid TFM simulation of gas-solid fluidized beds of Geldart A particles over a broad range of fluidization regimes.

Various researchers have explored proper scaling rules for DEM simulations (Link et al., 2009; Radl et al., 2011, 2012; Sutkar et al., 2013). To keep the contact forces constant, Radl et al. (2011) derived a scaling law for a linear-spring dashpot interaction model that enables tracking of clouds of particles through DEM-based simulation of scaled pseudo-particles. However this work did not consider the gas phase. A sophisticated filtered drag model was established in literature (Radl et al., 2012) for use in coarse-grid Euler-Lagrange simulations, highlighting the significant effect of particle clustering on the average slip velocity between particles and fluid and indicated how this clustering can be accounted for in unresolved EL-based simulations. The unclosed terms in the filtered model could also be constructed through a filtering operation of fine-grid resolved CFD-DEM simulations (Ozel et al., 2016, 2017).Ozel et al. (2017) performed Euler-Lagrange simulations of gas-solid flows in periodic domains to study the effective drag force model to be used in coarse-grained EL and filtered EE models. A dynamic scale-similarity approach was used to model the drift velocity but the predictability of that model is not entirely satisfactory. One scaling law that could apply for the flow regime was constructed by Glicksman et al. (1994) by keeping the key dimensionless parameters constant, including the ratio of the inertial and viscous forces. This scaling law could be extended to model bed-to-wall heat transfer. But additional scaling parameters were still required. The clustering of particles in circulating fluidized beds continues to be a fundamental issue in gas-particle hydrodynamics and has been found to be significant in risers (Guenther and Breault, 2007; O'Brien and Syamlal, 1993). A lot of effort has been dedicated to the characterization and quantification of clusters Cocco et al. (2010); Lackermeier et al. (2001); Shaffer et al. (2013). However, discussions about how to scale cluster phenomena is still lacking.

The objective of this chapter is to obtain an appropriate scaling method to scale down the vast number of solid particles in large systems. We employ the CFD-DEM code (OpenFOAM-CFDEM-LIGGGHTS) to obtain computational data of a pseudo-2D riser reactor, and perform a full comparison with experimental data (Varas et al., 2017) to study the hydrodynamics and associated cluster characteristics. The axial and horizontal profiles of time-averaged solids

volume fraction and solids mass flux are analyzed to study the hydrodynamic behavior. The solids holdup and spatial velocity distribution of clusters are discussed to study the cluster phenomena. The present chapter is organized as follows: in Section 4.2 we present the mathematical model, collision model and scaling method. The fluid and particle parameters and mapping conditions are described in Section 4.3. In Section 4.4, the scaled results are presented. Finally, the main conclusions are summarized in Section 4.5.

4.2 Numerical methodology

4.2.1 Description of the gas phase

The gas flow is modeled by the volume-averaged Navier-Stokes equations:

$$\frac{\partial \left(\varepsilon_g \rho_g \right)}{\partial t} + \nabla \cdot \left(\varepsilon_g \rho_g \mathbf{u}_g \right) = 0 \tag{4.1}$$

$$\frac{\partial \left(\varepsilon_g \rho_g \mathbf{u}_g \right)}{\partial t} + \nabla \cdot \left(\varepsilon_g \rho_g \mathbf{u}_g \mathbf{u}_g \right) = -\varepsilon_g \nabla P_g - \nabla \cdot \left(\varepsilon_g \tau_g \right) - \mathbf{S}_p + \varepsilon_g \rho_g \mathbf{g} \tag{4.2}$$

where the source therm $\mathbf{S}_p$ is defined as:

$$\mathbf{S}_p = \frac{1}{\Delta V} \sum_{i=0}^{N_p} \frac{\beta V_p}{1 - \varepsilon_g} \left(\mathbf{u}_g - \mathbf{v}_p \right) \delta \left(\mathbf{r} - \mathbf{r}_p \right) dV \tag{4.3}$$

where ΔV is the volume of the computational cell. The distribution-function δ distributes the reaction force of the particles exerted on the gas phase to the velocity nodes on the Eulerian grid. To calculate the interphase momentum exchange coefficient β we employed the Beetstra drag model (Beetstra et al., 2007):

$$F_{drag} = \frac{\beta d_p{}^2}{\mu} = 10\frac{1 - \varepsilon_g}{\varepsilon_g{}^2} + \varepsilon_g{}^2 \left(1 + 1.5\sqrt{1 - \varepsilon_g} \right) + \frac{0.413\mathrm{Re}_p}{24\varepsilon_g{}^2} \left(\frac{\left(\frac{1}{\varepsilon_g} + 3\varepsilon_g \left(1 - \varepsilon_g \right) + 8.4\mathrm{Re}_p^{-0.343} \right)}{\left(1 + 10^{3(1-\varepsilon_g)}\mathrm{Re}_p^{-\frac{1}{2}\left(1 + 4\left(1 - \varepsilon_g \right) \right)} \right)} \right) \tag{4.4}$$

with:

$$\mathrm{Re}_p = \frac{\varepsilon_g \rho_g |\mathbf{u}_g - \mathbf{v}_p| d_p}{\mu_g} \tag{4.5}$$

where Re_p is the particle Reynolds number.

4.2.2 Description of the particle phase

The soft-sphere Discrete Particle Model (DPM) used in this work was firstly proposed by Cundall and Strack (1979) and first employed in a gas-fluidized system by Tsuji et al. (1993). The particle behavior is governed by Newtonian equations of motion:

$$m_p \frac{d\mathbf{v}_p}{dt} = -V_p \nabla P + \frac{\beta V_p}{1 - \varepsilon_g} \left(\mathbf{u}_g - \mathbf{v}_p \right) + m_p \mathbf{g} + \sum_{j \neq 1} \left(\mathbf{F}_{n,ij} + \mathbf{F}_{t,ij} \right) \tag{4.6}$$

$$I_p \frac{d\omega_p}{dt} = \tau_p \tag{4.7}$$

where τ_p represents the torque and I_p the moment of inertia.

4.2.3 Collision parameters

Particles interact with their nearest neighbors via contact forces. The particle collisional forces are computed by means of the linear spring-dashpot soft sphere model (Cundall and Strack, 1979). To solve Eqs. 4.6 and 4.7, five parameters need to be specified: normal and tangential spring stiffness k_n and k_t, normal and tangential damping coefficient η_n and η_t, and the friction coefficient μ_g. In this model, the normal component of the contact force between two particles i and j can be calculated by

$$\mathbf{F}_{ij,n} = -k_n \delta_n \mathbf{n}_{ij} - \eta_n \mathbf{v}_{ij,n} \tag{4.8}$$

By combing this force expression with Newton's equation of motion we obtain:

$$m_{eff} \frac{d^2 \delta_n}{dt^2} = -k_n \delta_n - \eta_n \frac{d\delta_n}{dt} \tag{4.9}$$

where k_n is the normal spring stiffness, η_n the normal damping coefficient, δ_n the overlap of the two particles involved in the collision and m_{eff} the reduced mass of normal linear spring-dashpot system.

The damping coefficient is determined by:

$$\eta_n = 2\sqrt{k_n m_{eff}} \tag{4.10}$$

A similar procedure can be applied to the tangential spring-dashpot system. So the tangential damping coefficient is defined as:

$$\eta_t = \frac{-2 \ln e_t \sqrt{m'_{eff} k_t}}{\sqrt{\pi^2 + ln^2 e_t}} \quad (e_t \neq 0) \tag{4.11}$$

where m'_{eff} is the reduced mass of the tangential spring-dashpot system. The definitions of these two reduced masses are as follows:

$$m_{eff} = \frac{m_a m_b}{m_a + m_b} \tag{4.12}$$

$$m'_{eff} = \frac{2}{7} m_{eff} \tag{4.13}$$

The relation between the normal and tangential spring stiffness is given by:

$$\frac{k_t}{k_n} = \frac{2}{7} \frac{\pi^2 + (\ln e_t)^2}{\pi^2 + (\ln e_n)^2} \tag{4.14}$$

where e_n and e_t are the normal and tangential coefficient of restitution respectively, which are empirically determined. k_n is chosen such that the maximum overlap between two colliding particles in the simulation is smaller than 1% of the particle radius.

4.2.4   Scaling method

In order to reduce the number of discrete particles, the equations of motion and the collisional behavior of the particles will be scaled. The scaling rules presented in this section are chosen such that the particle size can be scaled in order to reduce the number of simulated particles drastically, whilst maintaining the same hydrodynamic behavior. The starting point of the analysis is the force balance of the particles. Here we consider the vertical component (z) of the force balance introduced earlier in Eq. 4.6. For the sake of the discussion, we will write it in a compact form, i.e. without complete expression of all forces:

$$m\frac{dv_z}{dt} = F_{g,z} + f_{p,z} + F_{D,z} + \sum_{j \neq 1} \left(F_{n,z,ij} + F_{t,z,ij} \right) \tag{4.15}$$

where the terms on the right hand side respectively represent forces due to gravity, far field pressure, drag and normal and tangential inter-particle contact. For simplicity we will subsequently drop the sub-script z in the subsequent equations.

The combined gravity and far field pressure forces can be described by:

$$F_g + F_p = V_p g \left(\rho_s - \rho_f \right) \tag{4.16}$$

Eq. 4.15 can be re-rewritten by dividing all terms by F_g:

$$\frac{1}{g}\frac{dv}{dt} = \underbrace{\frac{F_g + F_p}{F_g}}_{I} + \underbrace{\frac{F_D}{F_g}}_{II} + \underbrace{\frac{F_n}{F_g}}_{III} \left(1 + \underbrace{\frac{F_t}{F_n}}_{IV} \right) \tag{4.17}$$

In order to obtain the same hydrodynamic behavior each of the four dimensionless groups on the right hand side should be kept constant. This means that if we change the particle diameter (while keeping the overall solids volume the same), other parameters should be changed in such a manner that the respective dimensionless groups remain constant. We will now consider each of the four terms (groups) indicated in Eq. 4.17.

The ratio of buoyancy and gravity force (group *I*)

The first group implies that the ratio between the pressure and gravity forces should remain constant. This ratio can be simplified as:

$$\frac{F_g + F_p}{F_g} = \frac{V_p g \left(\rho_s - \rho_f\right)}{V_p g \rho_s}$$

$$N_p = \frac{\rho_s - \rho_f}{\rho_s} = 1 - \frac{\rho_f}{\rho_s}$$

(4.18)

The ratio of drag and gravity force (group *II*)

The second group implies that the ratio between the drag force and net gravity force should remain constant. This ratio can be expressed in terms of the particle Reynolds number Re, the Archimedes number Ar and the local void fraction ε:

$$\frac{F_D}{F_g} = \frac{\rho_s - \rho_f}{\rho_s} \frac{\text{Re}}{Ar} f(|\text{Re}|, \varepsilon) = \frac{1}{N_{Ar}} f(|\text{Re}|, \varepsilon),$$

$$\text{Re} = \frac{\varepsilon \rho_f u_{rel} d}{\mu}, Ar = \frac{d^3 \left(\rho_s - \rho_f\right) \rho_f g}{\mu^2}, N_{Ar} = \frac{d^2 \rho_s g}{\varepsilon \mu u_{rel}}.$$

(4.19)

when Re, ε and N_{Ar} are kept constant, the proper scaling would be obtained.

The ratio of normal contact force and gravity force (group *III*)

The third group implies that the ratio between the normal contact force and the gravity force remains constant. The normal contact force depends on the particle-particle overlap during contact and can be expressed as a combination of a linear spring-dashpot (Hooke model) (Hoomans et al., 1996):

$$\frac{F_n}{F_g} = \frac{k_n}{\rho_s V_p g} \delta_n + \frac{\gamma_n}{\rho_s V_p g} \dot{\delta}_n$$

$$= \frac{k_n d}{\rho_s V_s g} \frac{\delta_n}{d} + \frac{\gamma_n v_0}{\rho_s V_p g} \frac{\dot{\delta}_n}{v_0}$$

$$= N_{kn} \frac{\delta_n}{d} + N_{\gamma n} \frac{\dot{\delta}_n}{v_0}$$

(4.20)

where δ_n and $\dot{\delta}_n$ respectively are the overlap between the particles and the rate of change of the overlap, which are respectively normalized with the particle diameter d and the impact

velocity v_0. The contact parameters k_n and γ_n respectively represent the normal spring stiffness and damping coefficient, which are contained in the dimensionless groups N_{kn} and $N_{\gamma n}$. It is desirable that the overlap scales with the particle diameter and that the change in overlap scales with the impact velocity. These two criteria imply that the dimensionless groups N_{kn} and $N_{\gamma n}$ should be kept constant in the scaling.

The ratio of normal and tangential contact forces (group *IV*)

The fourth group implied that the ratio between the normal and tangential contact forces remains constant. This depends on the applied contact model, but is usually guaranteed, as both forces depend on the particle diameter and mass in the same way.

Scaling rules

The following dimensionless group should be kept constant when scaling the particle diameter:

$$\frac{\rho_f}{\rho_s}, \mathrm{Re} = \frac{\varepsilon \rho_f u_{rel} d}{\mu}, Ar = \frac{d^3 \left(\rho_s - \rho_f\right) \rho_f g}{\mu^2}, N_{kn} = \frac{K_n}{\rho_s d^2 g}, N_{\gamma n} = \frac{\gamma_n v_0}{\rho_s d^3 g}. \tag{4.21}$$

Note that alternatively the Reynolds number can be replaced by the Froude number:

$$\frac{\rho_f}{\rho_s}, Fr = \frac{\left(\rho_s - \rho_f\right)}{\rho_f} \frac{\mathrm{Re}^2}{\varepsilon^2 Ar} = \frac{u_{rel}^2}{gd}, Ar = \frac{d^3 \left(\rho_s - \rho_f\right) \rho_f g}{\mu^2}, N_{kn} = \frac{K_n}{\rho_s d^2 g}, N_{\gamma n} = \frac{\gamma_n v_0}{\rho_s d^3 g}. \tag{4.22}$$

The five groups can be rewritten in a more practical form as follows:

$$N_\rho = \frac{\rho_s - \rho_f}{\rho_s}, \mathrm{Re} = \frac{\varepsilon \rho_f u_{rel} d}{\mu}, N_{Ar} = \frac{d^2 \rho_s g}{\varepsilon \mu u_{rel}}, N_{kn} = \frac{K_n}{\rho_s d^2 g}, N_{\gamma n} = \frac{\gamma_n v_0}{\rho_s d^3 g}. \tag{4.23}$$

In this work the following parameters will be kept unscaled: u_{rel}, ε, v_0, ρ_s, ρ_f, while the seven remaining parameters will be changed to ensure proper scaling: d, μ, g, k_n, k_t, γ_n, γ_t.

Let us now consider system 0 that we want to scale to obtain system 1. Our goal is to obtain larger particles, so we introduce a scaling parameter K, changing the diameter by this scaling factor K and simultaneously changing the total number of particles by a factor K^{-3}.

All dimensionless groups under summarized Eq. 4.23 should be kept constant, accordingly we obtain:

$$d_1 = Kd_0, \mu_1 = K\mu_0, g_1 = \frac{g_0}{K}, K_{n1} = Kk_{n0}, K_{t1} = Kk_{t0}, \gamma_{n1} = K^2\gamma_{n0}, \gamma_{t1} = K^2\gamma_{t0}. \quad (4.24)$$

4.3 Simulation conditions

4.3.1 Simulation setup

To test the derived scaling rules, a pseudo-2D riser reactor with dimensions $1570 \times 70 \times 6$mm (height $\times$ width $\times$ depth) was simulated in our study. This riser was defined to serve as the base case for the series of CFD-DEM simulations. In the riser reactor (see Figure 4.1a), solid particles and gas flow co-currently upwards to the top of the riser, where the gas and particles are separated: gas will leave the system whilst particles are fed back into the riser from the bottom inlet region. Note that during insertion particle overlap was not accepted. No-slip boundary conditions were applied at all vertical walls.

The particles are initially placed in a random position in the bottom section of the riser up to a height of 0.25 m. In the base case, there are 50,000 particles positioned in this domain, where the gas superficial velocity was set at 5.55 m/s for the base case. This is high enough to ensure proper particle circulation in the CFB system, yet it is low enough to produce clusters. The (unresolved) gas-solid interactions were represented by the Beetstra drag force correlation (Beetstra et al., 2007), whereas the collision parameters corresponds to properties of glass beads previously reported by Hoomans et al. (1996). Further details of simulation settings of the base case are specified in Table 4.1 (column K = 1).

4.3.2 Simulation settings (the base group and scaling groups: K1; K2; K3)

To test the scaling, variations were made with respect to the base case, using three different scaling factors, i.e. K = 0.8, 1.25 and 2. The scaled parameters were scaled according to Eq. 4.24 and are listed in Table 4.1 along with the other key parameters.

A very important aspect to realize when scaling the particle size, is that the ratio between the particle size and other important spatial scales changes. In particular this involves the ratio of volumes of the computational grid cell and the particle ($\Delta V/V_p$, see Eq. 4.3) and the ratio of the shallow depth of the riser and the particle diameter (d_p/D). To check the importance of these two parameters, four scenarios of the scaled simulations were considered:

  - Condition a, base case, i.e. no scaling of grid size or riser depth,

  - Condition b, scaling of grid size and no scaling of riser depth,

  - Condition c, no scaling of grid size, but scaling of riser depth,

  - Condition d, scaling both grid size and riser depth.
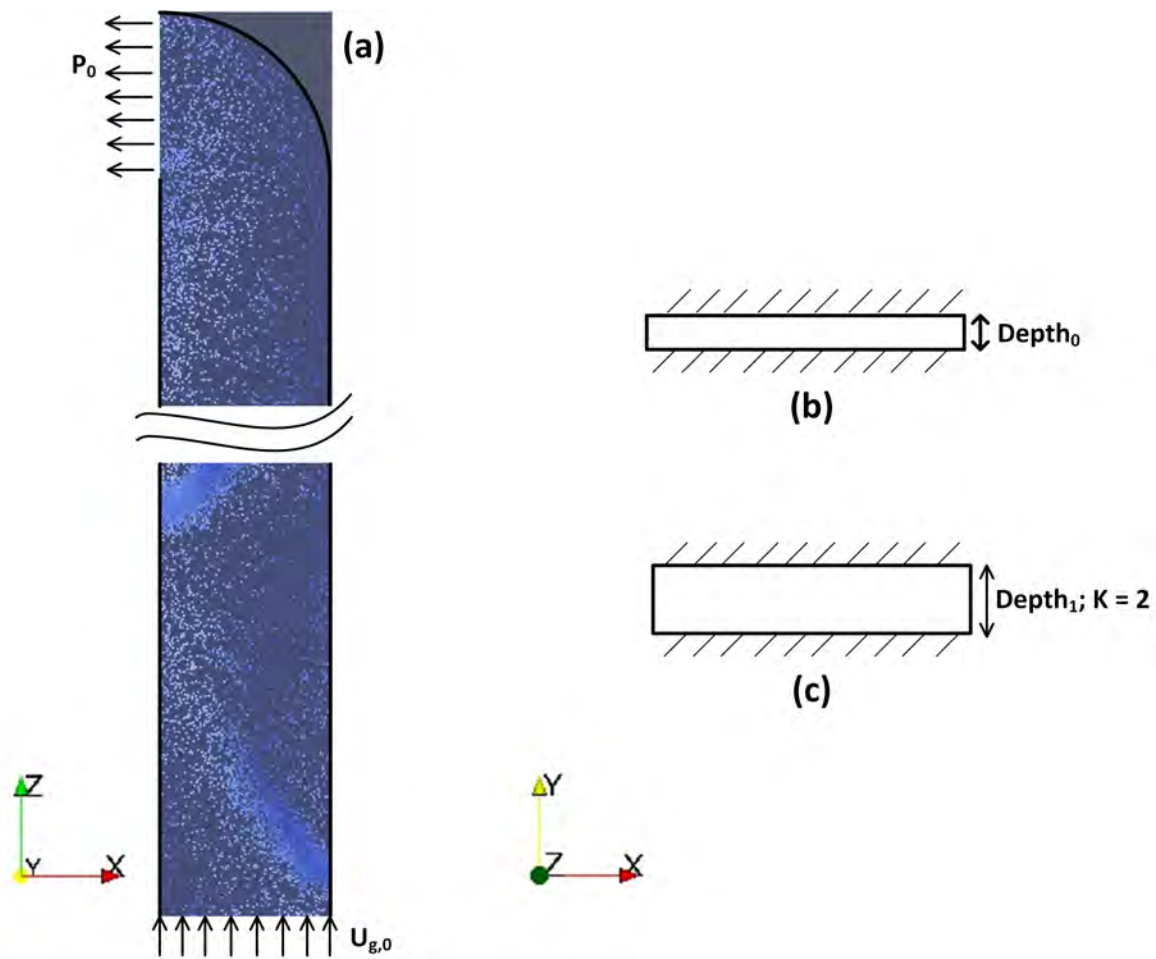
Fig. 4.1 (a) Schematic drawing of the pseudo-2D riser system. (b) base case from top view. (c) case with scaled depth from top view.

In Figure 4.1b and 4.1c the top views of the base case (Condition a) and cases of scaled riser depth (Conditions c and d) are shown respectively. The scaled diameter is $D_1 = KD_0$, where D_0 is the (unscaled) experimental riser depth. The scaled mapping parameters are specified in Table 4.2. Considering the fact that the grid number must be integer, in conditions b and d the volume ratio $\Delta V / V_p$ is kept almost constant. For all simulations, the last 10 s of the total 20 s were post-processed to obtain the time-averaged data. The computational cost was found to scale roughly linearly with the number of particles and computational cells.

Table 4.1 Numerical parameters used in the simulations. The scaled parameters are indicated in boldface.

Parameter	Unit	K=0.8	K=1	K=1.25	K=2
Particle diameter, d_p	mm	**0.68**	**0.85**	**1.06**	**1.70**
Particle density, ρ_p	kg/m^3	2500	2500	2500	2500
Solids voidfraction, ε_s	-	2.55%	2.55%	2.55%	2.55%
Particle number, N_p	-	97 656	50 000	25 600	6250
Gas density, ρ_g	kg/m^3	1.2	1.2	1.2	1.2
Gas viscosity, μ_g	kg/ms	**$1.44 \cdot 10^{-5}$**	**$1.8 \cdot 10^{-5}$**	**$2.25 \cdot 10^{-5}$**	**$3.6 \cdot 10^{-5}$**
Gravity, g	m/s^2	**12.26**	**9.81**	**7.848**	**4.905**
Gas velocity, v_g	m/s	5.55	5.55	5.55	5.55
Normal coefficient of restitution (p-p), e_n	-	0.96	0.96	0.96	0.96
Normal coefficient of restitution (p-w), e_n	-	0.86	0.86	0.86	0.86
Tangential coefficient of restitution e_t	-	0.33	0.33	0.33	0.33
Friction coefficient, μ	-	0.15	0.15	0.15	0.15
Normal spring stiffness, k_n	N/m	**1280**	**1600**	**2000**	**3200**
Tangential spring stiffness (p-p), k_t	N/m	**411.2**	**514**	**642.5**	**1028**
Tangential spring stiffness (p-w), k_t	N/m	**410**.36	**512**.95	**641**.2	**1025**.9

Table 4.2 Ratio in four different mapping cases. The parameters that are kept (almost) constant are indicated in boldface.

		K = 0.8	**K = 1**	**K = 1.25**	**K = 2**
$\Delta V/V_p$	a	57.0	29.2	14.9	3.6
	b	**30.4**	**29.2**	**29.9**	**29.2**
	c	60.8	29.2	14.9	3.6
	d	**29.2**	**29.2**	**29.9**	**29.2**
D/d_p	a	8.82	7.06	5.65	3.53
	b	8.82	7.06	5.65	3.53
	c	**7.06**	**7.06**	**7.06**	**7.06**
	d	**7.06**	**7.06**	**7.06**	**7.06**
$N_p(N_{cell})$	a	97 656 (67 200)	50 000 (67 200)	25 600 (67 200)	6 250 (67 200)
	b	97 656 (126 000)	50 000 (67 200)	25 600 (33 600)	6 250 (8 400)
	c	78 125 (50 400)	50 000 (67 200)	32 000 (84 000)	12 500 (134 400)
	d	78 125 (105 000)	50 000 (67 200)	32 000 (42 000)	12 500 (16 800)

4.4   Results and discussion

In this section the simulation results are presented, where first the overall flow patterns will be discussed. Subsequently, the solids volume fraction and mass flux distributions will be analyzed respectively, by making a comparison between simulation results and experimental data from literature (Varas et al., 2017). Finally, cluster characteristics will be discussed.

4.4.1   Overall flow patterns

In this sub-section a group of full-field configurations will be shown to study the gas-particle flow behavior. Figure 4.2 shows snapshots of gas void fraction while applying four scaling factors to the base case (Condition a). It is noted that in the vertical direction there is similar tendency of gas volume fraction revealing a dense region close to the riser inlet and more dilute middle and top regions. This distribution can be explained by the nature of particle motion in circulating fluidized beds; particles are fed to the system at the bottom of the riser, resulting in more collisions between particles and consequently more particles residing in this region. In the horizontal direction, a so called "core-annulus" flow pattern prevails, which has as dilute core and dense annular regions. In the dense region particle clusters are observed with complex mutual interactions.

Figure 4.3 shows a zoomed in section of the riser, which shows the cluster behavior in more detail. Clusters are formed in all four scaling scenarios, and appear to exhibit the same motion, moving downwards along the wall and upwards in the core region. When increasing the scaling factor K, it is noted that there are fewer particles with a larger diameter in the riser, which matches the definition of the scaling method. Clusters could be observed for all scaling scenarios but there appear to be less and smaller clusters with higher values of the scaling factors.

4.4.2   Time-averaged solid volume fraction distribution

The axial profiles of time-averaged solids volume fraction are shown in Figure 4.4. Every figure contains experimental data (Varas et al., 2017) and four sets of simulation results representing different scaling approaches. It is noted that both experimental and simulation results show the same tendency in the sense that dense regions exist in the bottom of the riser while the system becomes more dilute with increasing axial direction. This matches the observations from Figure 4.2. In Figure 4.4, each sub-figure represents a mapping condition. Even though they all maintain the same range and tendency, sub-figures (b) and (d) show a
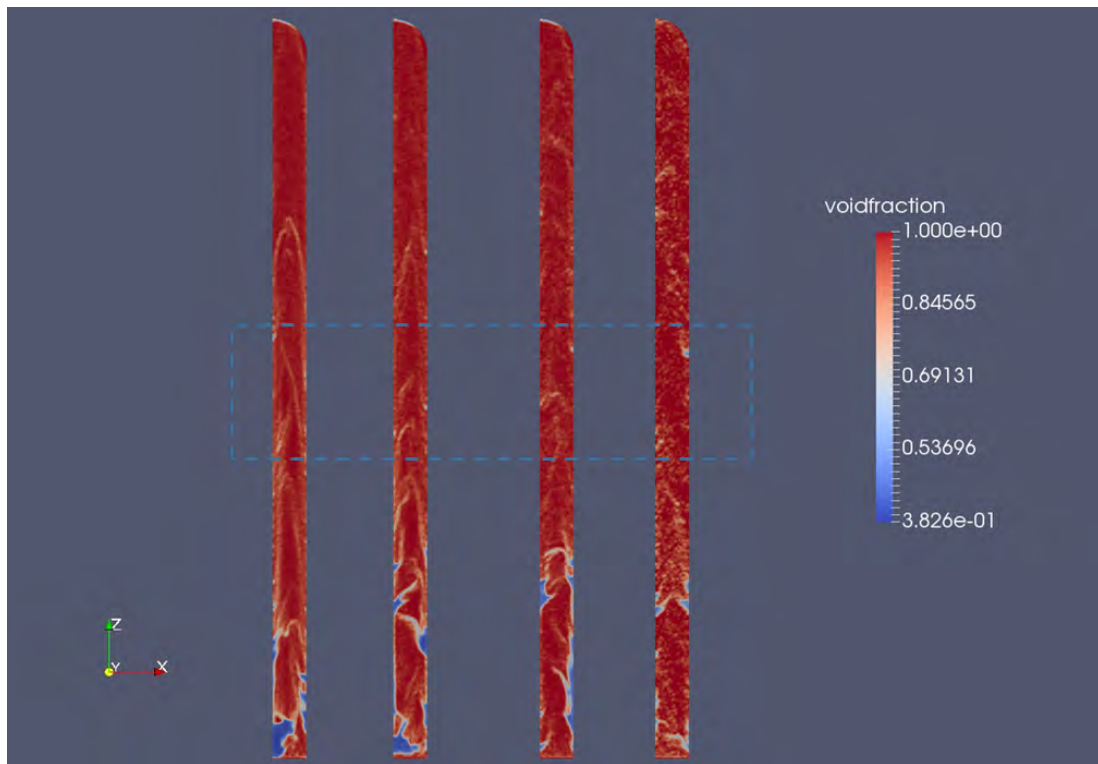
Fig. 4.2 Instantaneous gas-solid flow pattern: Left to right: K = 0.8, K = 1, K = 1.25, K = 2.

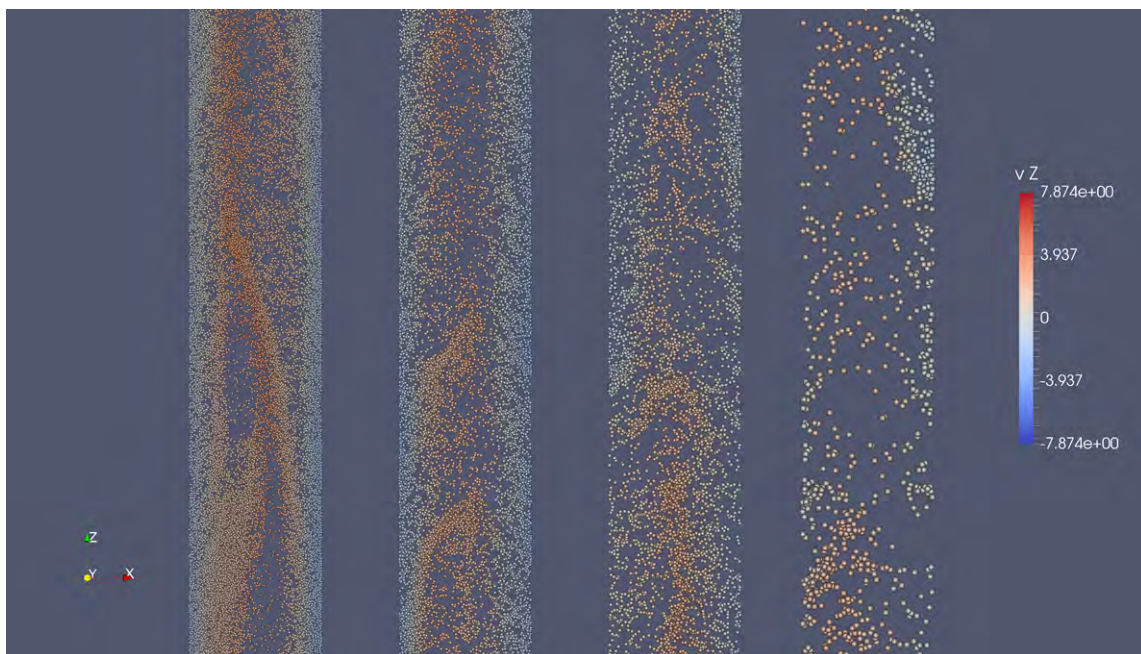Fig. 4.3 Snapshots of particle velocity of the middle region (dashes region in Fig. 4.2). Left to right: K = 0.8, K = 1, K = 1.25, K = 2.
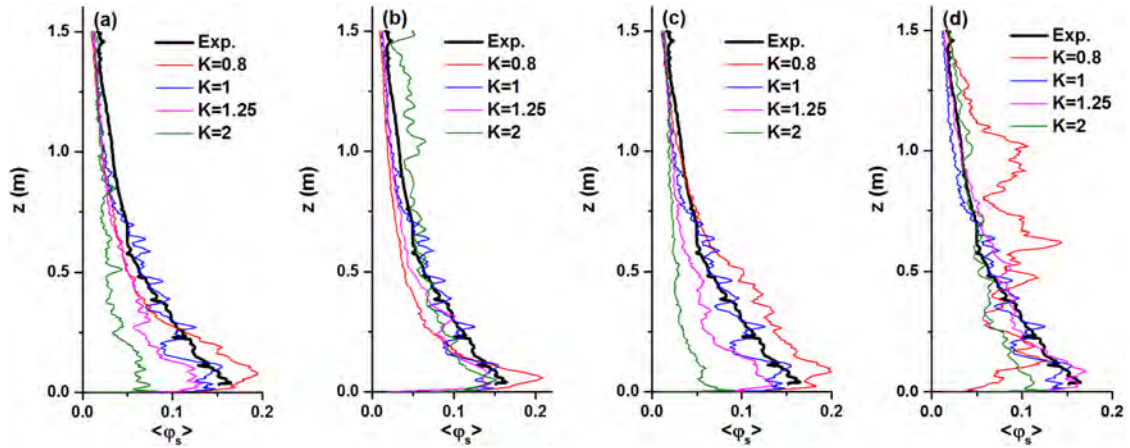
Fig. 4.4 Axial profiles of solids holdup under four scaling conditions.

better agreement with experiment than (a) and (c). The scatters of axial solids holdup of case $K = 0.8$ in Figure 4.4(d) will probably reduce when the simulation runs longer time.

In Figures 4.5 and 4.6, the cross-sectional profiles of solids volume fraction are displayed. The axial positions are 0.3 m and 1.2 m respectively in each figure, and each figure contains four sub-figures, which represents four different mapping conditions. In each sub-figure four simulation results using different scaling factors are compared with the experimental data. It can be seen that all simulation results show the same tendency as the experimental data. In the horizontal direction, the typical U-shaped profile is obtained. In the axial direction, the solids holdup decreases with increasing heights, which matches what we observed in Figure 4.4. The U-shaped profiles possess a flatter solids holdup profiles at higher positions in the riser.

The profiles of solids holdup in the dense (bottom) region are shown in Figure 4.5. All the mapping conditions are acceptable except condition c which is scaling riser depth while keeping the grid size constant. The volume ratio of grid size and particle is different. The ratio of riser depth and particle diameter is constant. As the fact that the riser is a pseudo-2D bed with no-slip boundary condition for the front/back walls, when scaling the riser depth the bridge formation of gas-solid hydrodynamics would be changed. Furthermore conditions b and d are suitable for all cases which applied the closured scaling up of the particle diameters.

In Figure 4.6 the solids holdup profiles in the dilute (top) region are displayed. It can be seen that at axial position H = 1.2 m the U-shaped profiles possess an asymmetric distribution for conditions b and d, which are cases having (almost) constant ratio of computational cell and particle volume. This is due to the fact that the curved one-sided lateral solids outlet has an apparent effect on the solids volume fraction in these two conditions.

79
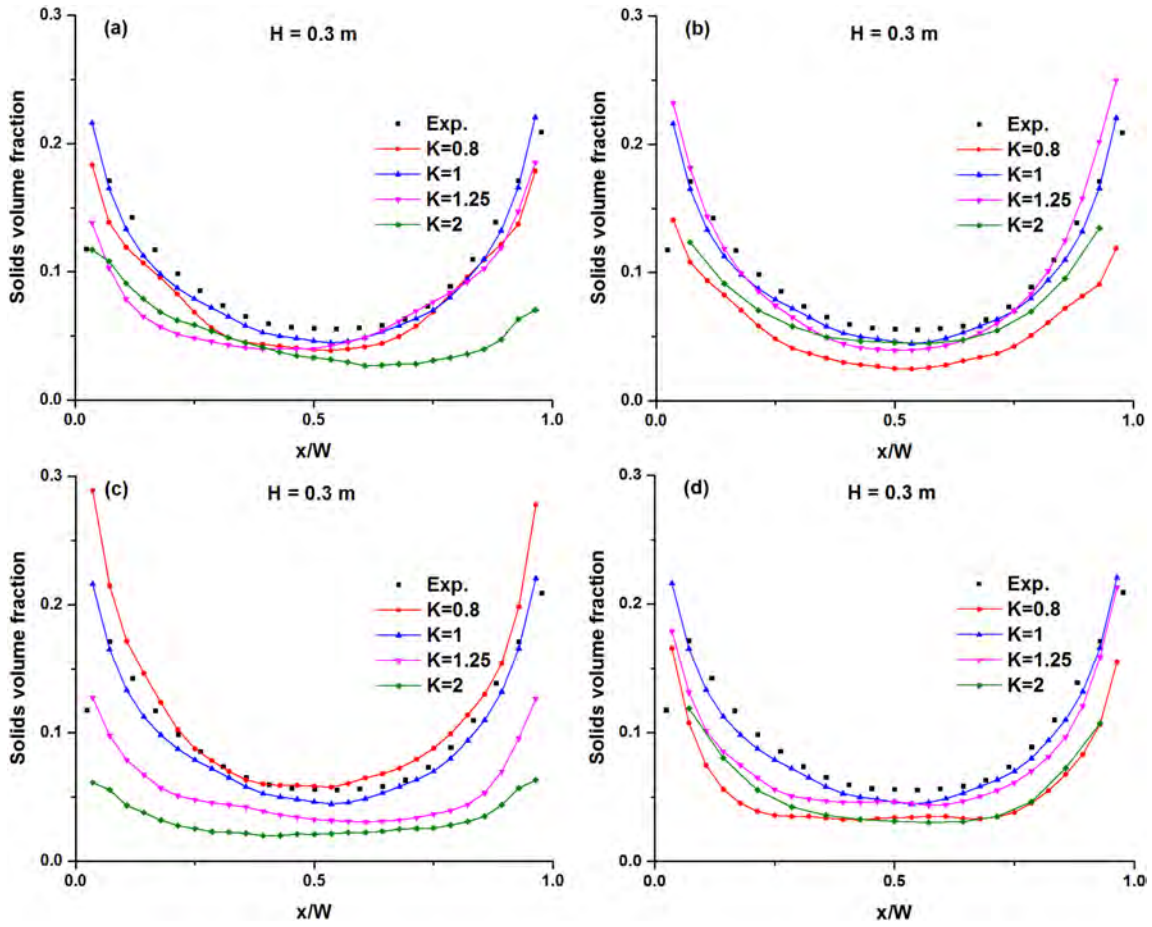
Fig. 4.5 Cross-sectional profiles of solids volume fraction under different scaling condition. H = 0.3 m.

4.4.3 Time-averaged solids mass flux profiles

The solids mass flux constitutes another important quantity and is computed for each computational cell from:

$$\langle \mathbf{G}_s(t) \rangle = \rho_s \langle \phi(t) \mathbf{v}_s(t)_{cell} \rangle \tag{4.25}$$

where the product of the local solids volume fraction ($\phi = 1 - \varepsilon$) and solids velocity is time-averaged.

Figures 4.7 and 4.8 show the simulated and experimental profiles of the solids mass flux at two axial positions 0.3 m and 1.2 m. The organization of these figures is the same as in section 4.4.2. The experimental data and simulation results exhibit the same tendency of solids up-flow in the core region of the riser and a relatively high down-flow close to the riser walls. At higher axial coordinates, the solids mass flux distribution becomes relatively flat.
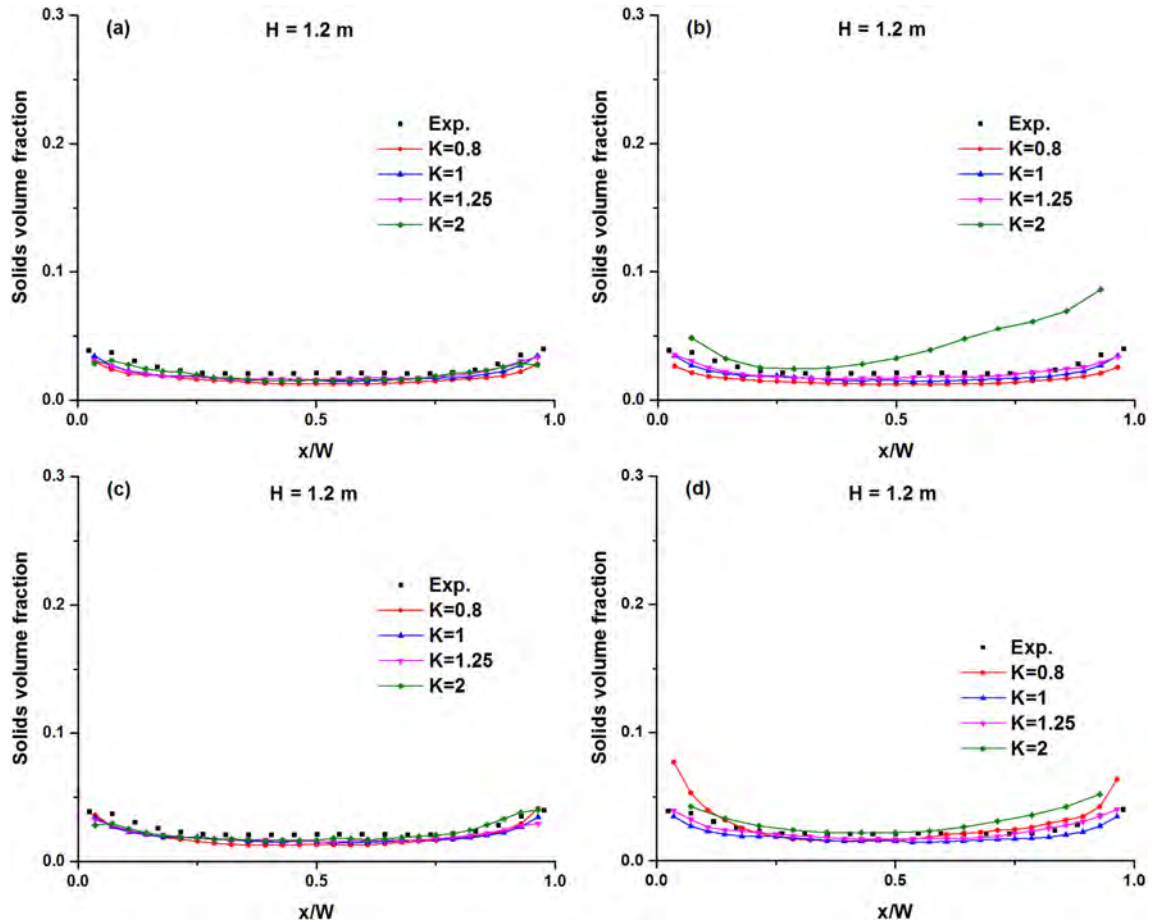
Fig. 4.6 Cross-sectional profiles of solids volume fraction under different scaling condition. H = 1.2 m.

By comparing the numerical results for different scaling factors, it is observed that scaling conditions b and d produce a better performance than the other two approaches. In Figure 4.8, the profiles of solids mass flux at height = 1.2 m are shown. The distribution of solid mass flux for K = 2 becomes more uniform than the other cases.

4.4.4 Cluster profiles

As previously mentioned, constant solids holdup thresholds are employed along the entire region of the pseudo-2D riser in order to detect and classify clusters. In this way, it is ensured that a uniform definition of clusters is used and that the quantified cluster-related properties are not influenced by a changing definition along the axial and cross-sectional directions of the riser. Clusters are defined as connected regions with local solids volume fractions larger than 0.2 everywhere that have a minimum area of 60 mm^2 and a dense core with
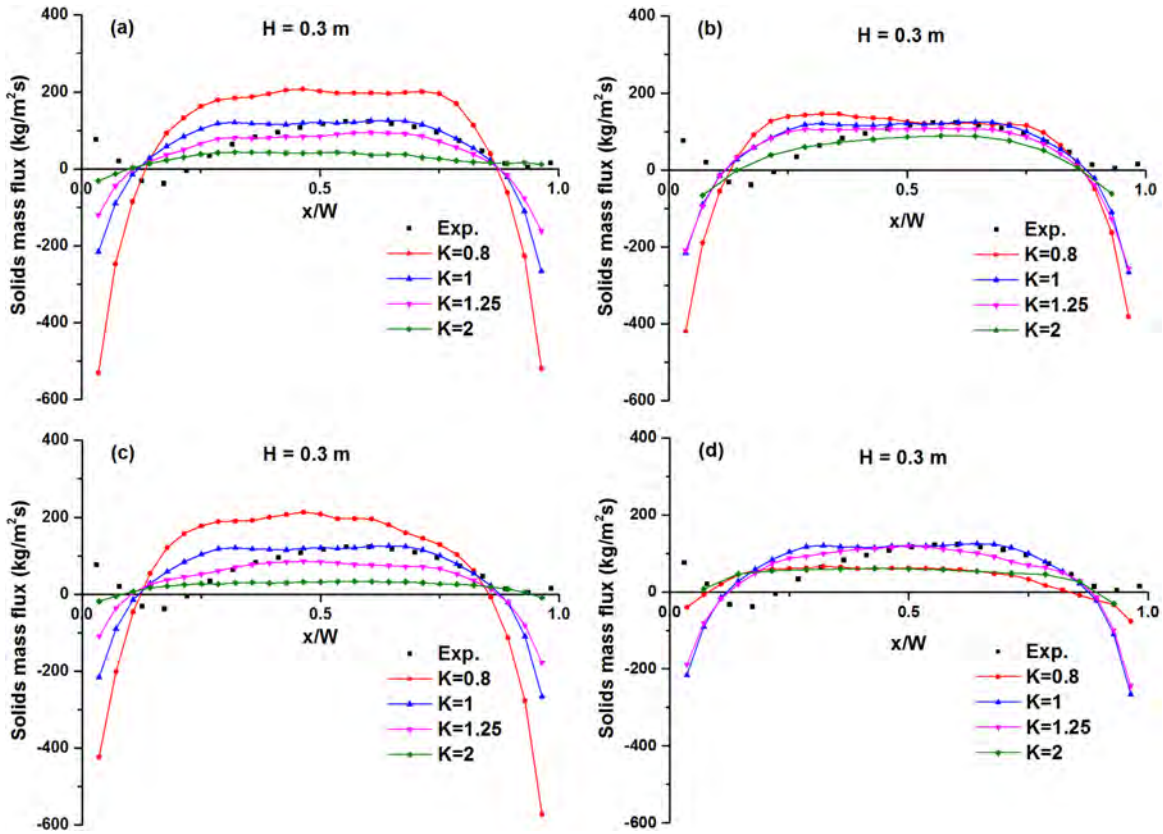
Fig. 4.7 Cross-sectional profiles of solids mass flux under four scaling factor. H = 0.3 m.

at least one grid with $\varphi_s > 0.4$. In this work the detection of clusters was performed by a Matlab script. Figure 4.9 displays the snapshots of particle velocity obtained from four scaling factor scenarios using mapping condition b. Clusters can be observed, with dense cores formed close to the wall and big dilute strands of particles that tend to move upwards. Comparing with Figure 4.3, especially in snapshot of K = 2 the cluster phenomena becomes more apparent in Figure 4.9. The represented clusters could be better captured when applying the scaling approach condition b than condition a.

To quantitatively study the cluster characteristics, profiles of cluster solids holdup are shown in Figure 4.10. The mean solids volume fraction of each cluster is computed for the corresponding cells which are occupied by the identified cluster. Therefore the averaged cluster internal solids holdup is calculated from the following expression:

$$\varphi_{cluster} = \frac{\sum \varphi_s}{\sum N_{cells,occupied}} \tag{4.26}$$

It is noted that for all the cases using different scaling factors and mapping conditions, the solids holdups of clusters are in a similar range with more clusters close to the walls
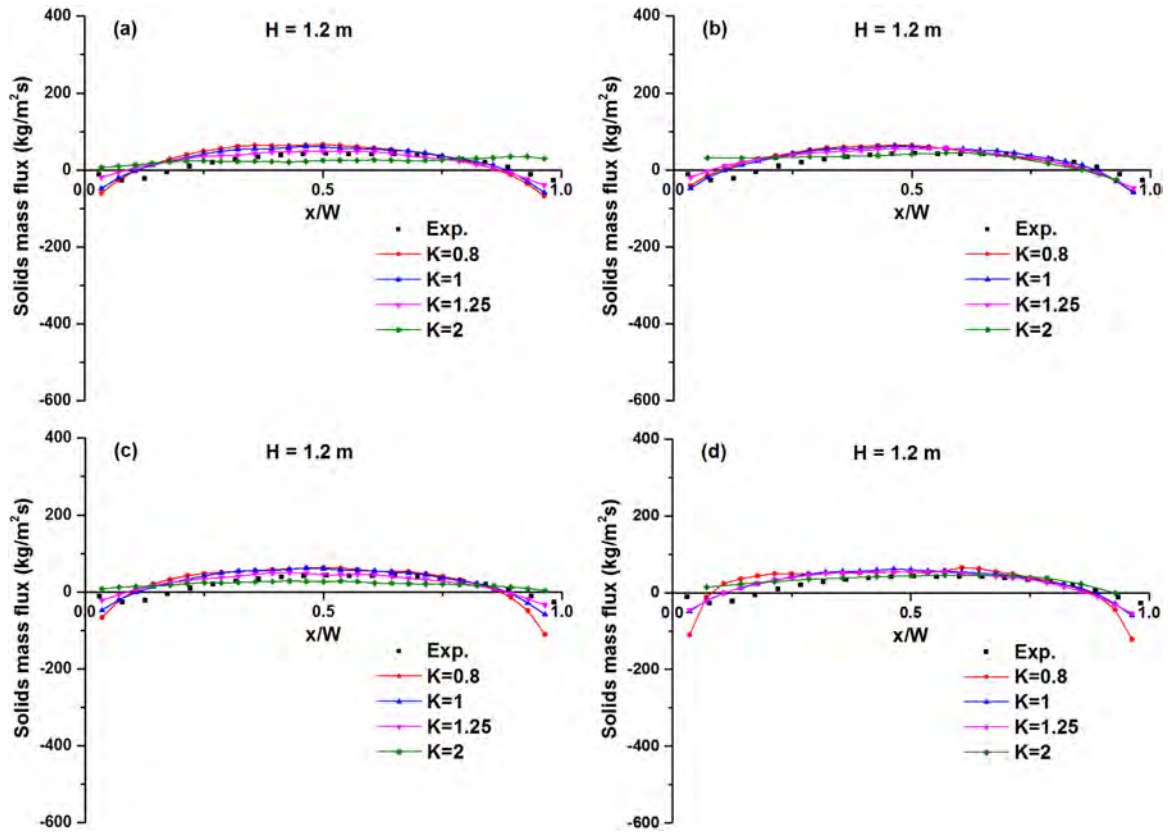
Fig. 4.8 Cross-sectional profiles of solids mass flux under four scaling factor. H = 1.2 m.

whilst the clusters are sparsely distributed in the core region. This reveals that our scaling method captures the cluster phenomena quite well. It can also be seen that a higher scaling factor leads to less clusters in the whole system. Whilst the cluster numbers do not show an obvious difference among the applied scaling factor approaches in conditions b and d and the core-annulus distribution is also well captured. This indicates that the volume ratio of grid and particle has a significant influence on cluster solids holdup profiles.

In Figure 4.11, profiles of cluster velocity are plotted for different scaling factors and mapping conditions. The typical symmetric core-annulus distribution is seen here, with mostly downwards flowing clusters near the wall whilst clusters in the core region are mostly moving upwards. This also matches with the observations from Figure 4.9. Using different scaling factors, the distribution of cluster velocity is quite similar and in the annulus region there are more clusters moving downwards except for the cases K = 2. In the set of K = 2 cases, the velocity distribution of clusters becomes more symmetric near the walls. In conditions b and d, the cluster number is more uniform in comparison with other conditions, so is the cluster velocity. Hence for further studies on cluster analyses, keeping the volume ratio constant would be advisable.
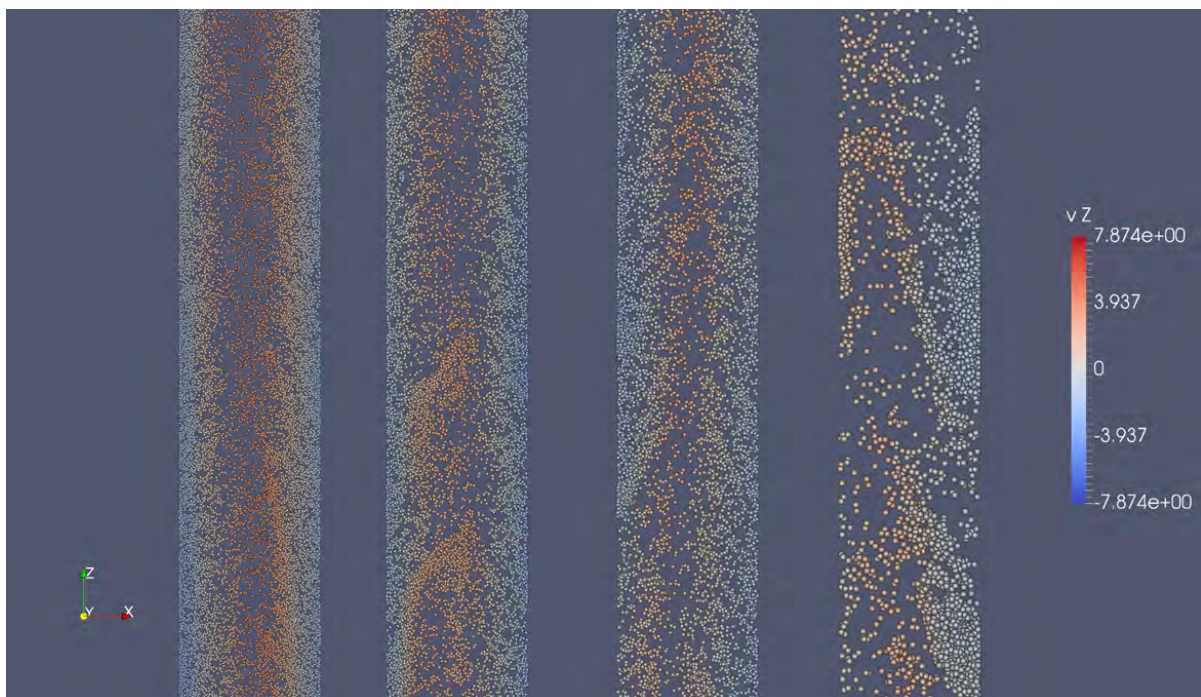
Fig. 4.9 Snapshots of cluster pattern of the middle region (dashes region in Fig. 4.2). Condition B, scaled grid and const. depth. Left to right: K = 0.8, K = 1, K = 1.25, K = 2.
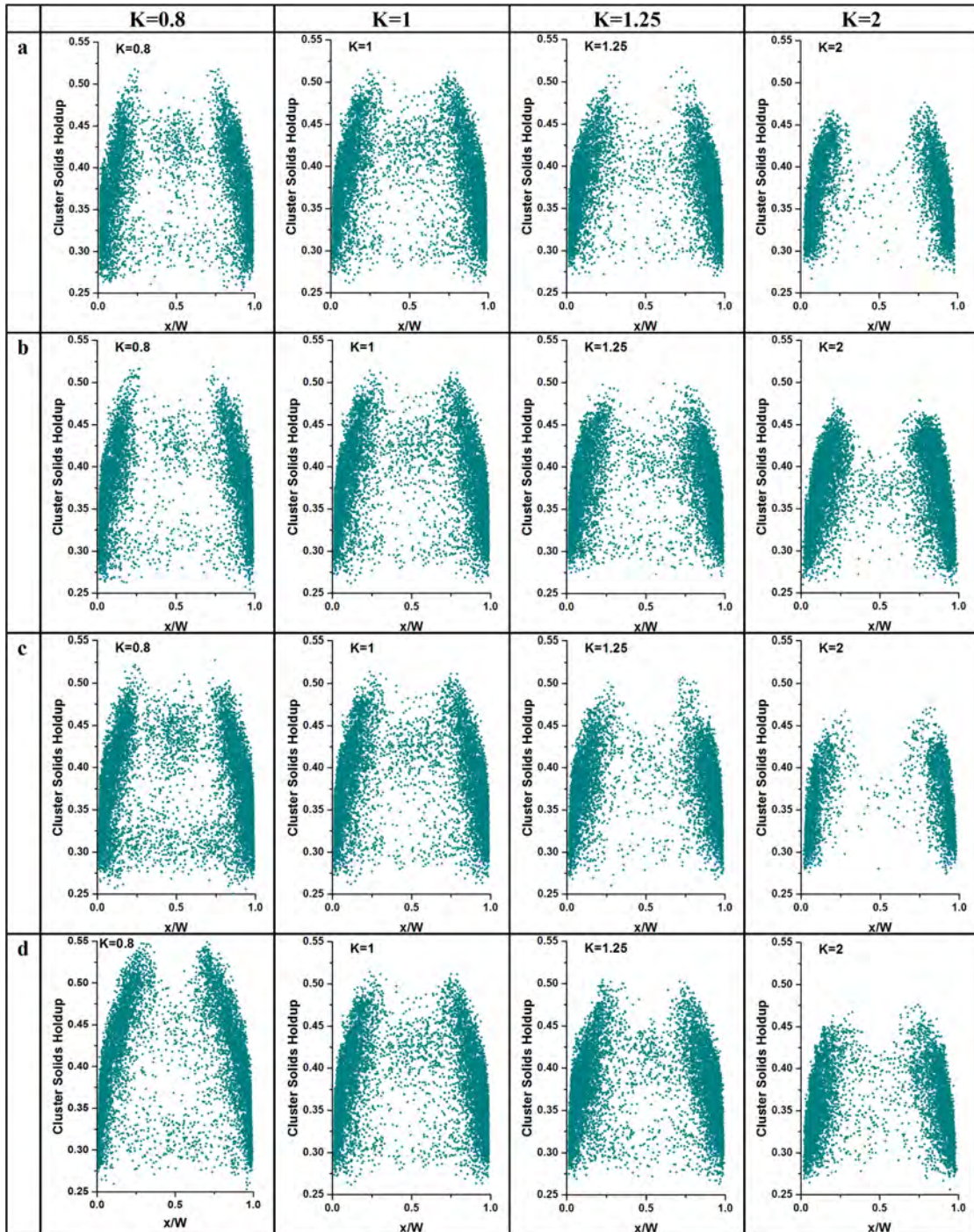
Fig. 4.10 Cluster solids holdup vs centroid locations under different scaling factors and mapping conditions.
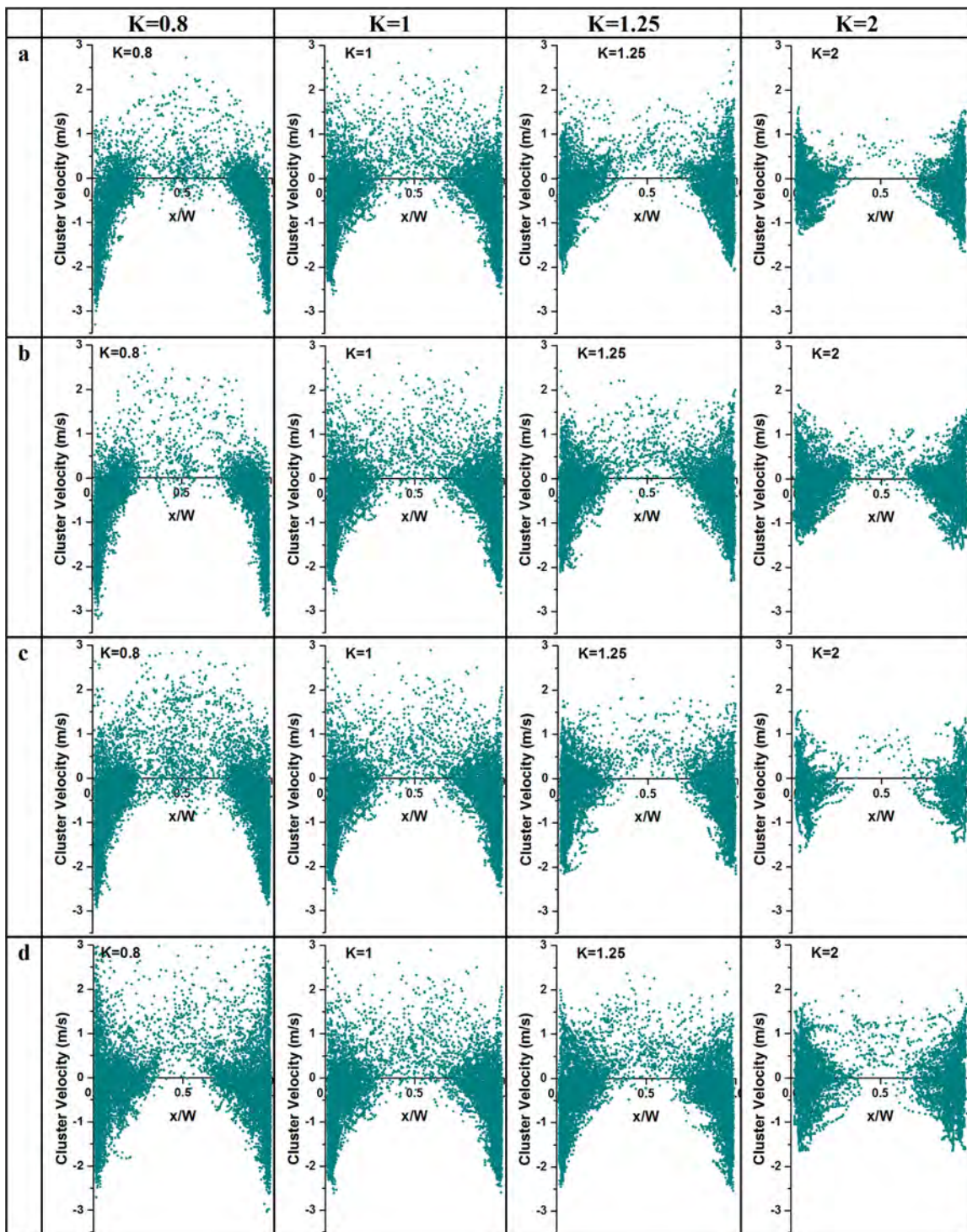
Fig. 4.11 Cluster velocity under different scaling factors and mapping conditions.

4.5   Conclusions and recommendations

In this chapter, a scaling method is developed and validated in detail by performing extensive simulations of a pseudo-2D circulating fluidized bed riser. To maintain the same hydrodynamic behavior seven gas and particle properties were scaled, such as the particle diameter, the gas viscosity, gravity, normal spring stiffness etc. Besides scaling the gas and particle properties, the grid size and riser depth are also scaled by considering four scaled mapping conditions. The influence of the scaling method, the scaled grid size and riser depth on the fluidized riser hydrodynamics has been quantified.

The experimental and simulated solids volume fraction and mass flux profiles provide quantitative information about the performance of the scaling method on gas-particle flow behavior. Firstly, it is noted that the scaling method could well capture the typical U-shaped solids volume fraction profiles, and the particle up-flow in the core region and a relatively high down-flow close to the riser walls. Secondly, considering the different mapping conditions, while applying different scaling factors (K) the solids volume fraction distributions match quite well for all mapping conditions except when the grid size is not scaled (conditions a and c). In the dilute region, the asymmetric geometry of the riser outlet has an apparent effect on the cross-sectional profiles of solids volume fraction when the grid size is scaled (conditions b and d). The solids mass flux profiles obtained for different scaling factors match much better in conditions b and d than in the other two conditions. In other words, when applying the scaling rules derived in this work, it is essential to also scale the value of $\Delta V/V_p$.

Furthermore, cluster characteristics (cluster holdup and velocity) were analyzed. By applying the scaling method, the simulation results exhibit similar trends in solids holdup and cluster velocity. When scaling is applied, there are more downwards flowing clusters close to the walls whilst the upwards clusters are sparsely distributed in the core region. It is noted that clusters could be better captured when applying the scaling method under conditions b or d than condition c. By analyzing the cluster holdups and velocity for different scaling factors, the spatial distribution of the clusters is more uniform in conditions b and d, and so is the cluster velocity. Finally, the core-annulus distribution is also well captured. This confirms that scaling of $\Delta V/V_p$ is essential for faithful prediction of cluster characteristics.

Chapter 5

Scaling Method for CFD-DEM Simulations of Binary Particle Systems

Abstract

In this chapter, the applicability of the scaling method developed in chapter four for binary systems is studied. A detailed comparison between experimental data and a series of Computational Fluid Dynamics (CFD)- Discrete Element Model (DEM) simulations of a pseudo-2D circulating fluidized riser is performed. By applying the scaling method, both the flow behavior and cluster characteristics are investigated, such as the velocity and holdup of solids and clusters of the binary system. To investigate how the scaling method behaves on binary systems, four mapping conditions with different ratios of the grid size and particle volume and modified ratio of riser depth to particle size were analyzed. The comparison of numerical and experimental results reveals that, to predict the hydrodynamic behavior and cluster phenomena of binary systems, a proper scaling of the interphase momentum mapping is necessary.

5.1   Introduction

In recent years, gas-solid circulating fluidized riser reactors have been extensively employed in a variety of industrial facilities and process engineering applications, including coal gasification (Bhutto et al., 2013; Kim et al., 1997; Klimanek et al., 2015; Minchener, 2005), fluid catalytic cracking (Almuttahar and Taghipour, 2008; Lappas et al., 2017; Yeo and Kim, 2020), petroleum coke (Chen and Lu, 2007; Chen et al., 2010; Conn, 1995; Cui et al., 2018), polymerization reactions (Gidaspow, 2019; Gobin et al., 2003; Trivedi et al., 2006). The increasing number and diversity of applications of the CFB riser have demanded the development of more realistic and efficient design tools. To accomplish successful and reliable design of circulating fluidized risers, numerous investigations have been undertaken over the past decades, facilitating a comprehensive understanding of the complex hydrodynamics of gas-solid flows (Almuttahar and Taghipour, 2008; Li et al., 2014; Patience and Chaouki, 1993), in which clusters play a significant role in flow structure evolution (Firuzian et al., 2014; Patel et al., 2021). Therefore, significant efforts have been made to obtain detailed information on the characteristics and parameters of clusters through both experiments and simulations (Wei et al., 2020; Yang and Zhu, 2014), such as the size, velocity and solid concentration inside the clusters, and cluster live time, to obtain a better understanding of their structure. Because of the large scale of gas-solid systems such as circulating fluidized beds, the simulations are quite expensive and time-consuming. In industrial units, such as FCC reactors, the distribution of catalyst particles affects the hydrodynamics behavior profoundly (Gidaspow and Huilin, 1998; Grace and Sun, 1991; Yang et al., 2021). Careful consideration of how to fulfill both accuracy and efficiency of the numerical simulations are therefore essential.

In the past decades, Euler–Euler (E–E) and Euler–Lagrange (E-L) approaches have been employed for simulations of gas-particle flows. In the E–E approach, to which the Two-Fluid Model (TFM) belongs, both the fluid phase and the particle phases are represented as continuous phases. In contrast, the Euler–Lagrange method combines a continuum description of the fluid phase with a Lagrange representation of the dispersed phase, based on the Newtonian equations of motion. Due to difficulties of an accurate representation of the particle-particle and particle-wall collisions, the E-E method requires additional model assumptions. In contrast, in the Euler-Lagrange approach collision detection between particle and particle or particle and wall can be deterministically detected. Fine-grid TFM simulations of Geldart A particles with homogeneous drag model were reported by Hong et al. (2016), demonstrating that the method is suitable for low-gas-velocity bubbling fluidized beds but is not adequate to resolve the meso-scale structures in high velocity fluidized beds. Adamczyk et al. (2014) made a comparison between the standard Euler-Euler and novel hybrid Euler-

Lagrange approaches, and found that the use of the hybrid Euler–Lagrange approach to model air-fuel combustion is very promising, whilst there is an important disadvantage of using the Euler-Euler approach due to long calculation times. To study the hydrodynamics of gas-solids flows in a 3D lab-scale spouted fluidized bed, Almohammed et al. (2014) investigated the behavior of Euler-Euler and CFD-DEM models. It turns out that the two-fluid model shows some notable discrepancies when the gas mass flow rate is increased while the CFD-DEM approach is more successful in reproducing realistic flow patterns. The effect of spent catalyst distribution and horizontal baffles in an industrial FCC regenerator was investigated by using MP-PIC numerical simulation (Yang et al., 2021), where the results suggest that the MP-PIC simulations can be successfully employed to study the effect of internals on the hydrodynamics in an industrial coaxial compact FCC regenerator. Alobaid et al. (2013) proposed a procedure that allows the variation of the Eulerian grid resolution independent of the particle size and consequently improves the calculation accuracy and suggested that the extended CFD-DEM model can predict accurately the particle motion and the pressure gradients in quasi-2D spouted–fluidized beds.

Recently, CFD-DEM has established itself as the most flexible simulation tool for moderately large gas-solid systems. To make such simulations accurate, the adapted model should be as realistic as possible, requiring representation of the size distribution of the particles. The main challenge of CFD-DEM is the computational time related to the large number of particles (Hoomans et al., 2000) and limited physical time which can be considered in the simulations. Considerable efforts have been made by researchers to optimize the CFD-DEM method. Parallel algorithms for the Discrete Element Method (DEM) software were utilised to increase the speed of calculations, including tools such as the Message Passing Interface (MPI) or OpenMP (Fleissner and Eberhard, 2008; Maknickas et al., 2006). However, (Alobaid et al., 2014) states that parallelization only accelerates CFD-DEM simulations if the critical number for the domain decomposition, which depends on the number of particles, is not reached. Above this number, the performance is no longer proportional to the number of processors. An increase in solids contents results in a shift of the critical decomposition number to a higher number of CPUs. A linked and hashed DEM grid was constructed by Brosh et al. (2014) to speed up the simulation and they found out that by carrying out an NBS (No Binary Search) in the hashed DEM cell for particles of similar size, near linear search behavior was attained and additionally that the contact search algorithm is much faster. Bierwisch et al. (2009) investigated a grain-scale rule for the parameters in a certain set of force interaction laws which can be applied to different DEM forces and claimed that their derivation of the force scaling was valid for a dilute granular system where only binary collisions occur and for a dense system via the solids phase stress tensor. But whether the

scaling is still valid in intermediate dense regimes is not clear. Lichtenegger and Pirker (2018) described the influence of the smallest particles in strongly polydisperse systems in an implicit fashion and derived simple models for the separated and single, broad size distribution cases where particle numbers are reduced drastically at minor accuracy impairments. However, the implications of this model are discussed only for the interaction with a fluid phase but not its impact on the contact mechanics of the material. Although a lot of effort has been made to accelerate CFD-DEM simulations, how to speed up the simulations of polydisperse fluidized systems still requires more attention.

Due to the broad distribution of particle diameters in circulating fluidized beds, the behavior of the scaling method as discussed in Chapter 4 has so far not been tested on the binary system, which will be reported in this chapter. First the methodology and governing relations of the CFD-DEM method and the scaling method are described. Subsequently the scaled properties and four different scaling scenarios will be introduced and discussed. In the following section, the effect of scaling method on the binary particle flow characteristics, including cluster characteristics are discussed. The main findings and the concluding remarks of this work are included in the final section.

5.2   Numerical method

The CFD-DEM method (CFDEM) developed by Kloss et al. (2009) has been employed to carry out simulations of co-current gas-solids flow in a CFB riser. The Navier-Stokes and continuity equations are used to describe the flow patterns of the gas phase:

$$\frac{\partial \left(\varepsilon_g \rho_g\right)}{\partial t} + \nabla \cdot \left(\varepsilon_g \rho_g \mathbf{u}_g\right) = 0 \tag{5.1}$$

$$\frac{\partial \left(\varepsilon_g \rho_g \mathbf{u}_g\right)}{\partial t} + \nabla \cdot \left(\varepsilon_g \rho_g \mathbf{u}_g \mathbf{u}_g\right) = -\varepsilon_g \nabla P - \nabla \cdot \left(\varepsilon_g \tau_g\right) - \mathbf{S}_p + \varepsilon_g \rho_g \mathbf{g} \tag{5.2}$$

where the source momentum term $\mathbf{S}_p$ represents the momentum exchange with the particulate phase and is given by:

$$\mathbf{S}_p = \frac{1}{\Delta V} \sum_{i=0}^{N_p} \frac{\beta V_p}{1 - \varepsilon_g} \left(\mathbf{u}_g - \mathbf{v}_p\right) \delta \left(\mathbf{r} - \mathbf{r}_p\right) dV \tag{5.3}$$

In the equations, the subscript g indicates the fluid phase and p the particulate phase. Individual particles are labeled by the subscript i. The gas-particle drag coefficient β is calculated from the Beetstra drag correlation (Beetstra et al., 2007).

The particle motion is governed by the Newtonian equations of motion:

$$m_p \frac{d\mathbf{r}_p^2}{dt^2} = -V_p \nabla P + \frac{\beta V_p}{1 - \varepsilon_g} \left(\mathbf{u}_g - \mathbf{v}_p\right) + m_p \mathbf{g} + \mathbf{F}_c \tag{5.4}$$

$$I_p \frac{d\omega_p}{dt} = \tau_p \tag{5.5}$$

where r_p represents the particle position. The forces on the right-hand side of Eq. 5.4 are due to the pressure gradient, drag, gravity and contact forces. τ_p is the torque and ω_p the angular velocity.

The scaling model

Facing the large number of particles in a CFB riser, a moderate reduction of the number of discrete particles would already decrease the simulation time considerably. To reach this goal, while maintaining comparable hydrodynamic behavior, the equations of motion and the collisional behavior of the particles will be scaled properly.

Based on the scaling method of our previous work (Mu et al., 2020), the following five dimensionless groups will be kept constant:

$$N_\rho = \frac{\rho_s - \rho_f}{\rho_s}, \text{Re} = \frac{\varepsilon \rho_f u_{rel} d}{\mu}, N_{Ar} = \frac{d^2 \rho_s g}{\varepsilon \mu u_{rel}}, N_{kn} = \frac{K_n}{\rho_s d^2 g}, N_{\gamma n} = \frac{\gamma_n v_0}{\rho_s d^3 g}. \qquad (5.6)$$

Hence, in this study,

- The following five parameters will be kept constant: u_{rel}, ε, v_0, ρ_s, ρ_f,

- The remaining seven parameters will be changed to ensure proper scaling: d, μ, g, k_n, k_t, γ_n, γ_t,

- The scaling rules of particles of different size are principally the same and hold for all particle properties: diameter, spring stiffness and damping factor:

$$d_1 = K d_0, \mu_1 = K \mu_0, g_1 = \frac{g_0}{K}, K_{n1} = K k_{n0}, K_{t1} = K k_{t0}, \gamma_{n1} = K^2 \gamma_{n0}, \gamma_{t1} = K^2 \gamma_{t0}$$

$$(5.7)$$

where K represents the scaling factor.

5.3   Simulation settings

The geometric design of the simulations is based on the experimental setup of Mathiesen et al. (2000). The diameter of the riser is 32 mm and 1.0 m high. At the top of the riser, the suspended particles enter a cyclone where the solids are separated from the gas and recycled via a return loop. The gas inlet distributor is located at the bottom of the riser. Performing simulations of this full-scale 3D cylindrical CFB riser with millions of particles is time-consuming and difficult. Consequently it has been described to represent the actual geometry as a pseudo-2D full-field riser reactor located in the middle section of the cylindrical riser tube. The top view of the system and its representation is shown in Fig. 5.1. The simulation domain in our study is $1000 \times 32 \times 1.2$ mm (height $\times$ width $\times$ depth). The front and back wall are set to free slip boundary conditions, whilst left and right wall no slip.
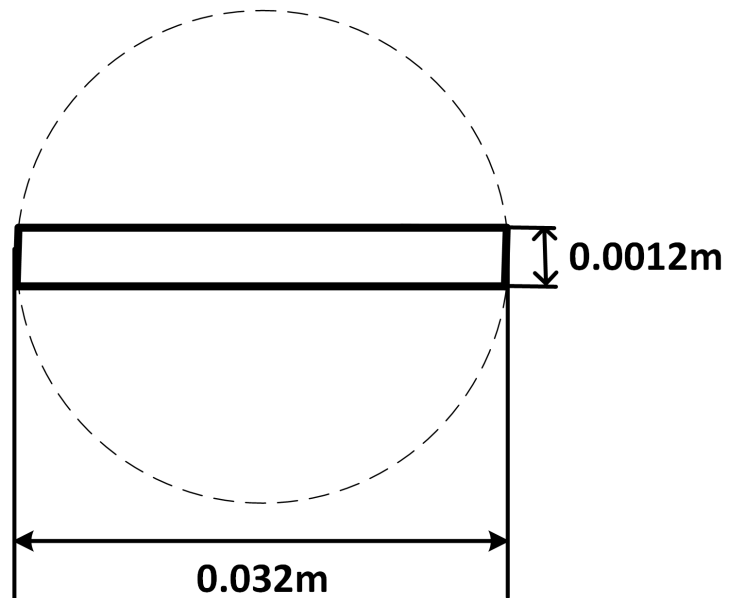
Fig. 5.1 Schematic drawing of the riser (from top view) tube and the representation in the simulations.

The binary system consists of two groups of particles: type 1 and type 2, which represent the smaller size of particles and larger ones respectively. The scaled parameters and other relevant parameters are summarized in Table 5.1. The two distinct particle groups are mixed thoroughly at the bottom of the riser with identical solids volume fractions. The overall solids volume fraction in the riser amounts 2.5%. For each case the simulated time amounts 12 s where time-averaging was performed from 5 s to 12 s.

Similar to Chapter 4, four scenarios (conditions) of the scaled simulations were considered:

- Condition a, base case, i.e. no scaling of grid size or riser depth,

Table 5.1 Numerical parameters. The scaled parameters are indicated in boldface.

Parameter	Unit	K = 1	K = 1.5	K = 2	K = 3
Particle diameter	μm	**125 185**	**187.5 277.5**	**250 370**	**375 555**
Particle density	kg/m^3	2400	2400	2400	2400
Particle number	-	**614, 465**	**182, 064**	**76, 808**	**22, 758**
Gas density	kg/m^3	1.2	1.2	1.2	1.2
Gas viscosity	kg/m·s	**$1.8 \cdot 10^{-5}$**	**$2.7 \cdot 10^{-5}$**	**$3.6 \cdot 10^{-5}$**	**$5.4 \cdot 10^{-5}$**
Gravity	m/s^2	**9.81**	**6.54**	**4.905**	**3.27**
Gas velocity	m/s	1.0	1.0	1.0	1.0
Normal coefficient of restitution	-	0.97	0.97	0.97	0.97
Tangential coefficient of restitution	-	0.33	0.33	0.33	0.33
Friction coefficient	-	0.1	0.1	0.1	0.1
Normal spring stiffness	N/m	**1600**	**2400**	**3200**	**4800**
Tangential spring stiffness	N/m	**514.08**	**771.13**	**1028.17**	**1542.25**

- Condition b, scaling of grid size and no scaling of riser depth,

- Condition c, no scaling of grid size, but scaling of riser depth,

- Condition d, scaling both grid size and riser depth.

The effect of the above scaling conditions on some of the relevant hydrodynamic ratios and the respective number of particles in the system are given in Table 5.2.

Table 5.2 Ratios of cell volume to particle volume and cell size to particle size, for the two particle groups respectively, in four scaling scenarios. The parameters that are kept (almost) constant are indicated in boldface.

		K = 1		K = 1.5		K = 2		K = 3	
$\Delta V/V_p$	a	587.0	181.1	173.9	53.7	73.4	22.6	21.7	6.7
	b	**587.0**	**181.1**	**695.7**	**214.6**	**587.0**	**181.1**	**695.7**	**214.6**
	c	587.0	181.1	173.9	53.7	73.4	22.6	21.7	6.7
	d	**587.0**	**181.1**	**521.8**	**161.0**	**587.0**	**181.1**	**521.8**	**161.0**
D/d_p	a	9.6	6.5	6.4	4.3	4.8	3.2	3.2	2.2
	b	9.6	6.5	6.4	4.3	4.8	3.2	3.2	2.2
	c	**9.6**	**6.5**	**9.6**	**6.5**	**9.6**	**6.5**	**9.6**	**6.5**
	d	**9.6**	**6.5**	**9.6**	**6.5**	**9.6**	**6.5**	**9.6**	**6.5**
$N_p\,(N_{cell})$	a	614 465 (64 000)		182 064 (64 000)		76 808 (64 000)		22 758 (64 000)	
	b	614 465 (64 000)		182 064 (16 000)		76 808 (8 000)		22 758 (2 000)	
	c	614 465 (64 000)		273 095 (96 000)		153 616 (128 000)		68 274 (192 000)	
	d	614 465 (64 000)		273 095 (32 000)		153 616 (16 000)		68 274 (8 000)	

5.4 Results and discussion

In this section, the results are presented for the set of simulations as described in the previous section. First, the effect of the scaling mapping conditions (a-d) on the time-averaged particle velocity and solids volume fraction profiles of the binary system will be discussed. Subsequently, the effect of different scaling factors (K) on the binary system will be studied. In both parts a comparison of the simulation results with the experiment data from literature is included (Mathiesen et al., 2000). Finally, the effects on the cluster characteristics of the binary system will be discussed.

5.4.1 Effect of scaling mapping conditions (K = 3)

To obtain a qualitative impression of the influence of different scaling mapping conditions on the riser flow behavior, snapshots of the volume fraction of the gas phase in the total riser are represented in Figure 5.2, displaying results for condition a to d from left to right. As can be seen, under all four scaling mapping conditions the volume fraction of the gas phase increases significantly along the riser height. Horizontally more clusters are observed close to the walls in agreement with the expected core-annulus flow structure of a riser.

Figure 5.3 shows the time-averaged solids volume fraction of small and large particles (left and right column) along the horizontal direction for K = 3. By comparing the simulation results from four different scaling conditions and the experimental results, we find that the solids volume fraction invariably decreases along the vertical direction of the riser. This agrees with many experimental observations that CFB risers feature a dense bottom section and a dilute top section. Horizontally, the solids volume fraction distribution is U-shaped both for simulations and experiments which is caused by the loss of kinetic energy due to dissipative collisions between particles and walls. Furthermore, condition b produces the best agreement between the experimental and simulation results.

Lateral profiles of the time-averaged particle vertical velocity are shown in Figure 5.4. These velocity profiles at three different heights are displayed from top to bottom, whilst small and large particles are shown from left to right respectively. In each figure the comparison between experimental data and simulation results is shown using one of the four different scale conditions. The same tendency of up-flow in the center region and down-flow close to the left and right walls are displayed. These results match our expectations namely a dense region at the bottom of the riser and dilute region at the top. Conditions a and c produce a flatter distribution than conditions b and d for both types of particle. This suggests that scaling the grid size is an important factor in scaled simulations of solids flow in CFB risers.
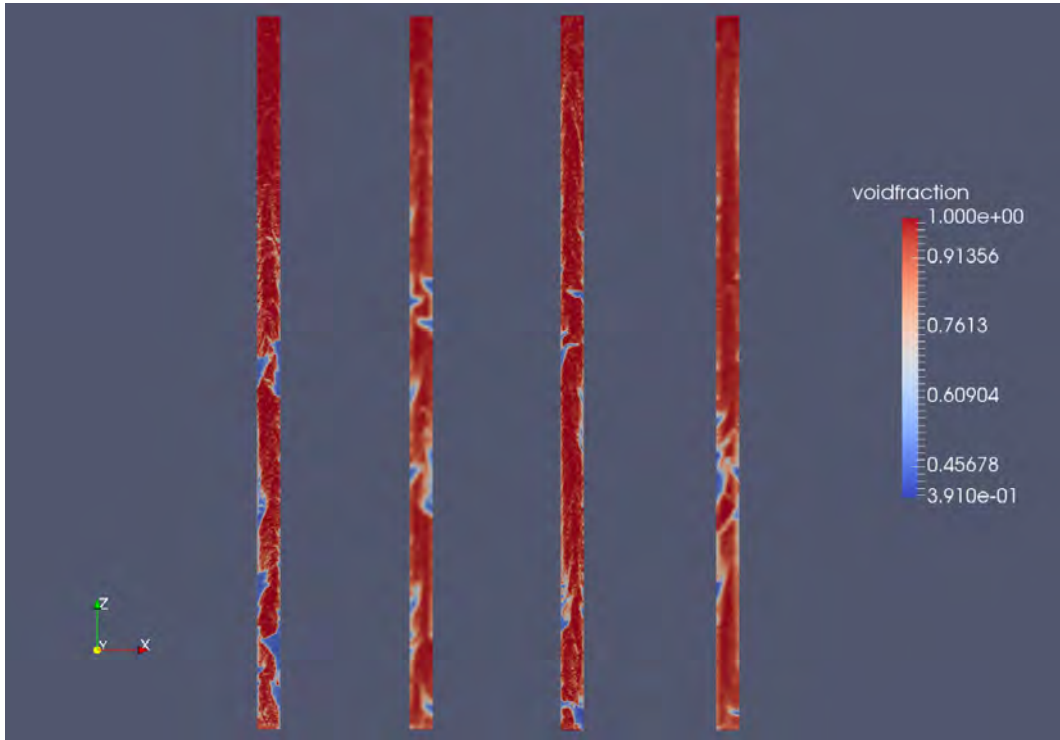
Fig. 5.2 Snapshots of gas phase volume fraction profiles of the total riser under different scaling factor conditions, K = 3, with results from different mapping strategies a to d displayed from left to right.

Therefore, in the following subsections, condition b will form the basis for discussion of the impact different scaling factors on particle velocity profiles and cluster characteristics.

5.4.2   Effect of scaling factors (Condition b: scaled grid.)

Due to the large number of particles for case K = 1 and the required computational time the final results for this case could unfortunately not be obtained. The simulation ran for 5.89 s which took about 26 weeks of computational time. By comparing the time-averaged particle velocity, solids volume fraction and mass flux profiles for case K = 2 for time-averaging intervals of (5 - 12) s and (4 - 5.89) s it was found that at lower heights (i.e. less than 0.4 m) the gas-solid phase flow has become steady whilst at higher elevation in the riser the flow pattern is still developing. Therefore, in the first top row of Figure 5.5 the time-averaged particle velocity at lower height under different scaling factors including K = 1 case are displayed, whilst in the second and third row the velocity profile at higher heights under only three scaling factor conditions are presented. The experimental data and simulation results exhibit the same tendency of solids down-flow close to the riser walls and a relatively high up-flow

Fig. 5.3 Time-averaged solids volume fraction profiles of small and large particles at different heights, K = 3 with different mapping conditions a-d.

Fig. 5.4 Time-averaged particle vertical velocity profiles of small and large particles at different heights, K = 3, under different mapping conditions a-d.

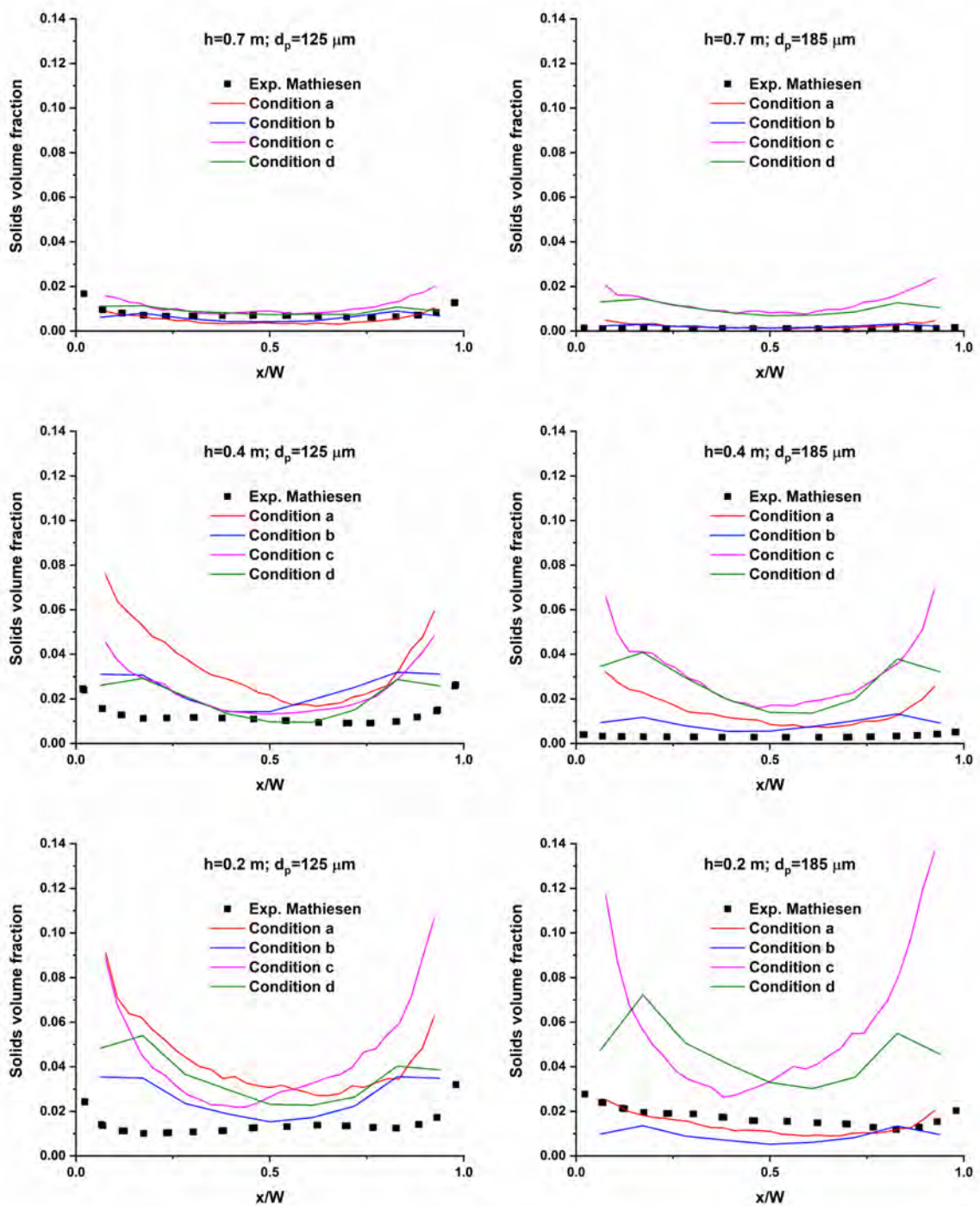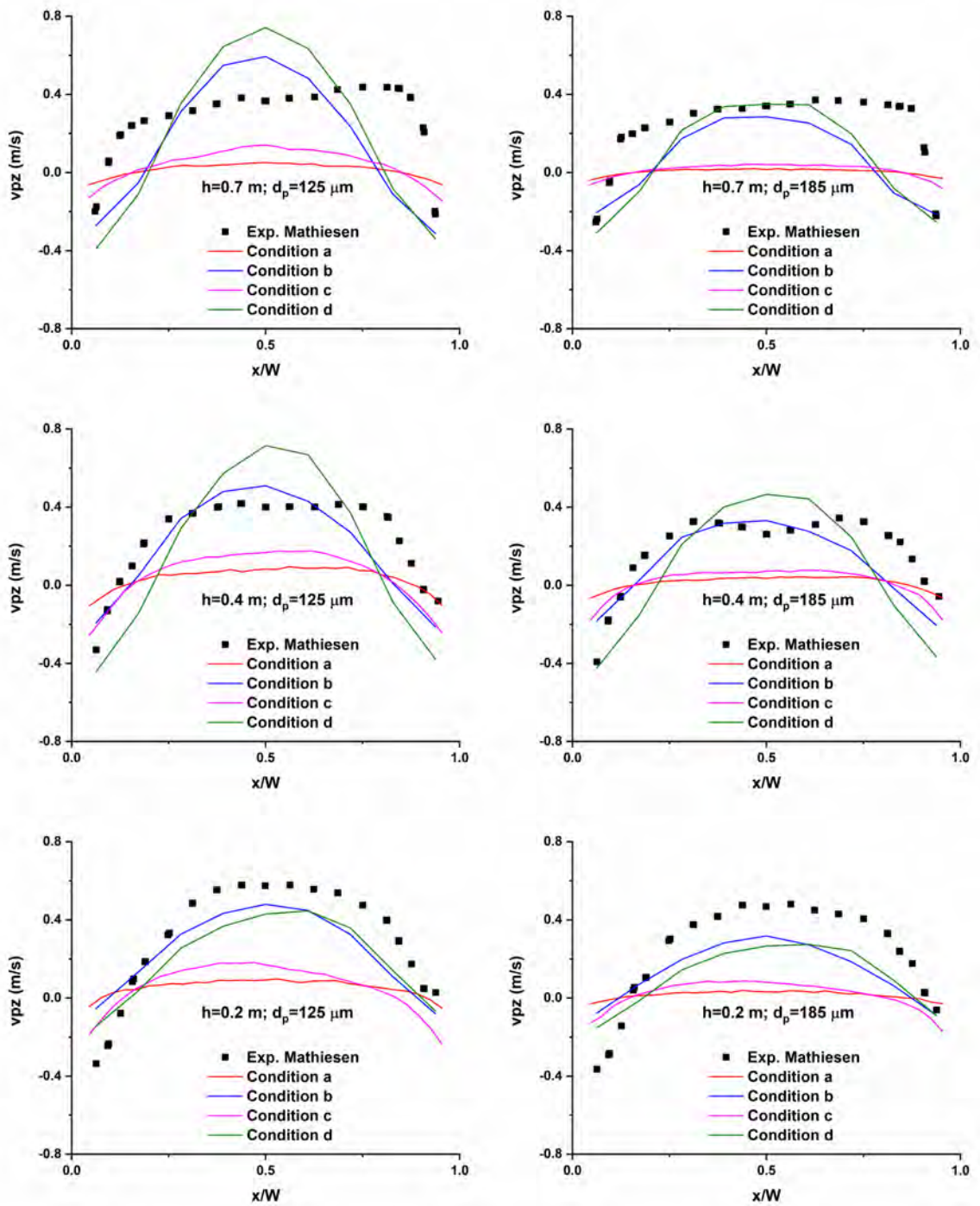in the core region of the riser. At higher vertical positions, the particle velocity distribution of large particles becomes relatively flat, while for small particles, the simulation results indicate that the velocity distribution in the core region becomes narrower than observed in the experiments.

By comparing the simulation results obtained for different scaling factors, it is observed that at h = 0.2 m in the riser the scaled simulations produce a better performance with respect to the predicted particle velocities in the binary system in comparison with the results obtained at the two higher positions. However, the differences between results obtained for different scaling factors are acceptable.

Figure 5.6 shows the simulated and experimental profiles of the solids volume fraction for the two types of particles at three different axial positions 0.7 m, 0.4 m and 0.2 m (from top to bottom) respectively. The organization of these figures is the same as in Figure 5.5. The experimental and numerical profiles exhibit the same features of the U-shape distribution along the horizontal direction with a relative dilute core region and a dense region close to the walls of the riser. In the bottom zone the flow is more dense than in the top of the column. These observations hold for both types of particles.

From the two sub-figures at h = 0.2 m, it can be seen that the solids volume fraction profile for K = 1 is less smooth in comparison with the other three cases, which is due to longer simulation times for the higher K cases. Furthermore, the distribution of solids volume fraction of K = 3 becomes more uniform than the other cases. This observation as well holds for both types of particles.

5.4.3 Effects on Cluster profiles

Clusters are denser regions in the riser that form naturally due to dissipative particle-particle and particle-wall collisions in dense riser flows. Clusters have a considerable impact on the flow structure in gas–solid circulating fluidized beds. In this subsection, the cluster profiles of the binary system, under different scaling and mapping conditions, will be studied. The same cluster detection method as used in Mu et al. (2020) was adopted.

Figure 5.7 displays several snapshots of the particles, colored by velocity in the middle region of the riser. From left to right the total amount of particles, small particles and large particles are shown in the selected region. It can be seen that the two types of particles are well mixed in the riser and each cluster contains both types of particles. Hence the following analyses of the cluster characteristics of the binary system will be carried out in more detail by adding the contributions of the two type of the particles to the overall solids volume fraction rather than dividing each cluster to two parts. The particle velocity distributions of these two types of particles match with the observations from Figure 5.4 and

Fig. 5.5 Time-averaged particle velocity profiles of small and large particles at different heights, Condition b: scaling grid, for different scaling factors (K).

5.5. Furthermore the analysis reveals that the clusters in the core region are moving upwards while the ones close to the walls are moving downwards.
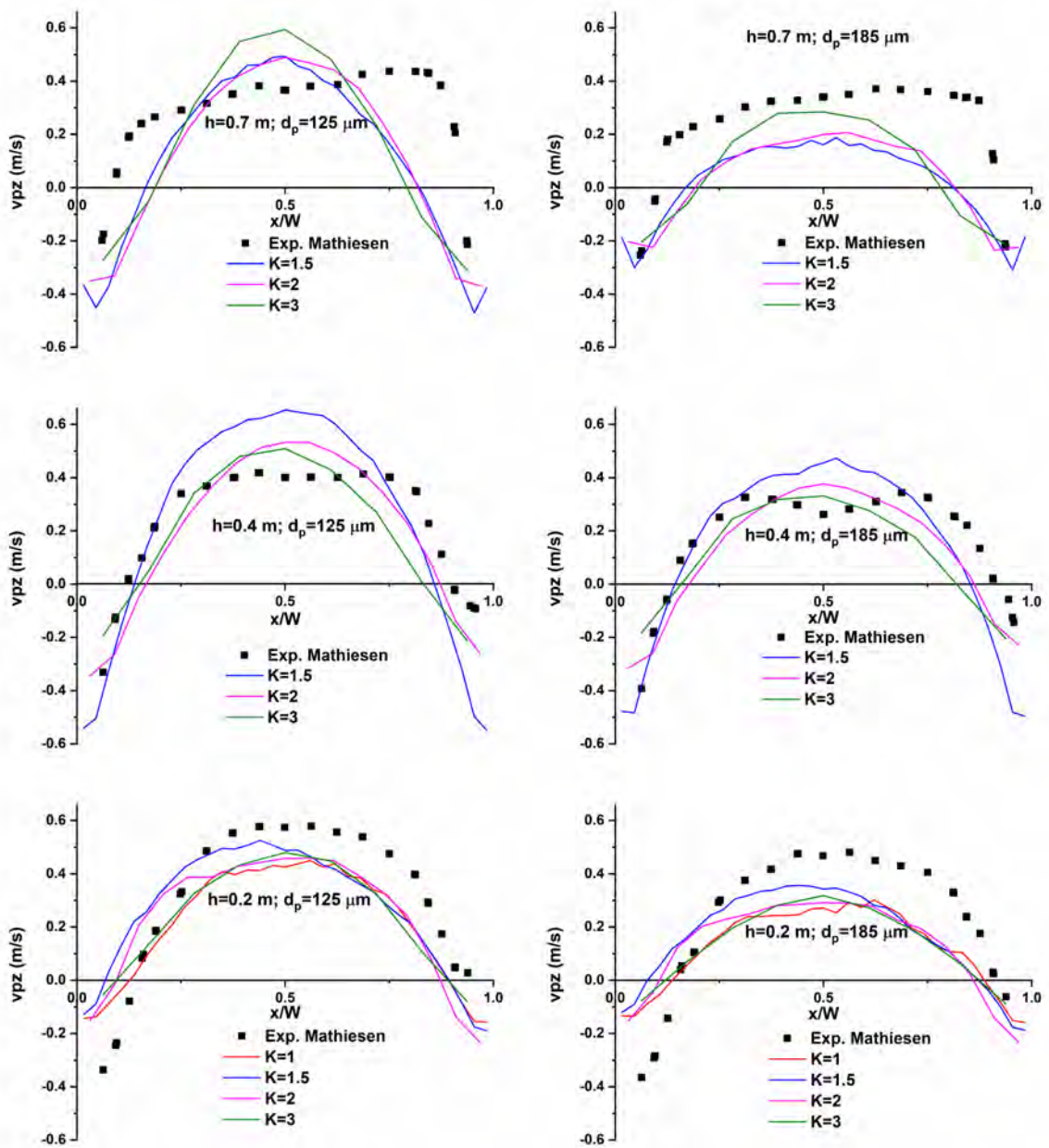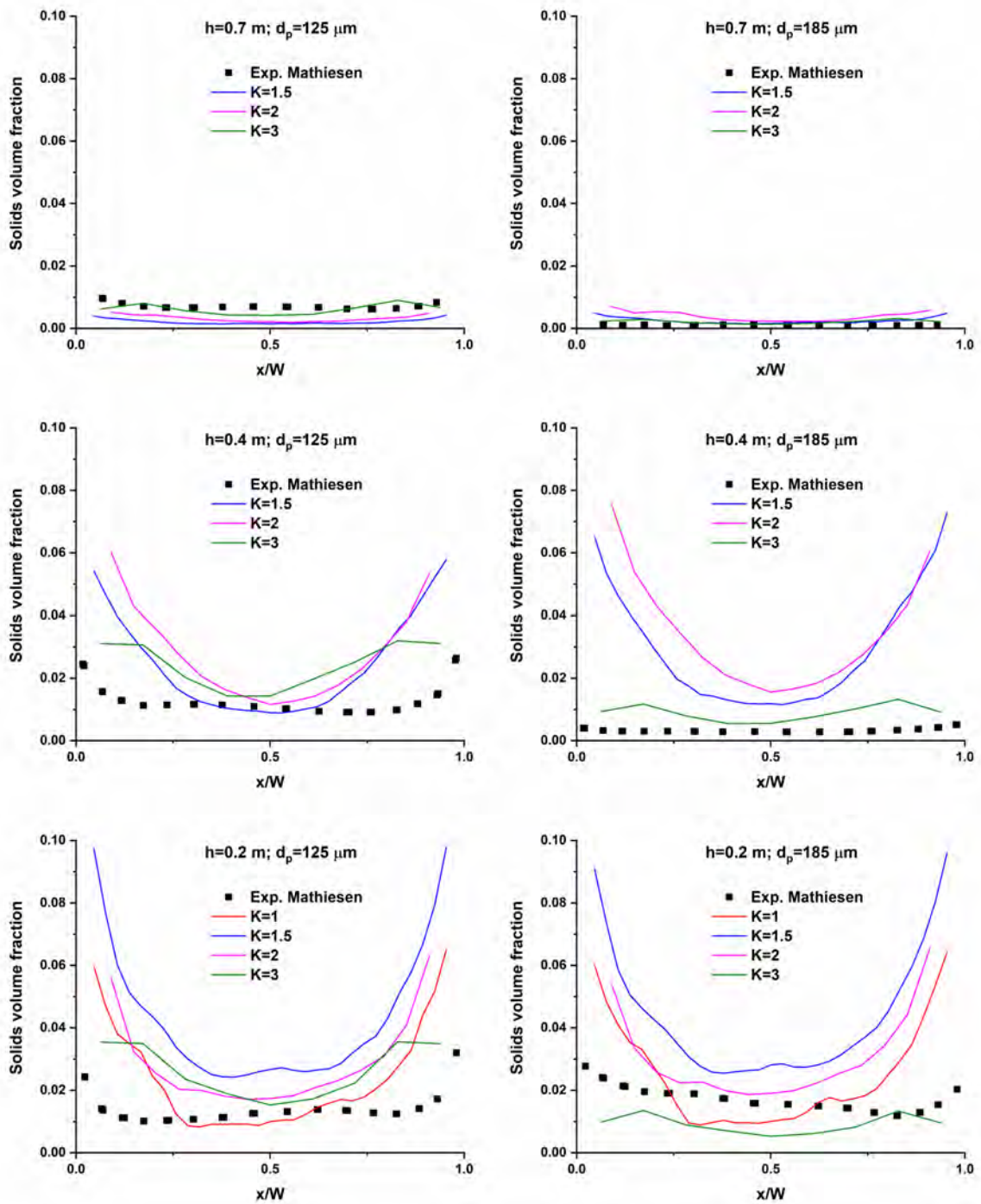
Fig. 5.6 Time-averaged solids volume fraction profiles of small and large particles at different heights, Condition b: scaling grid, under different scaling factor (K).
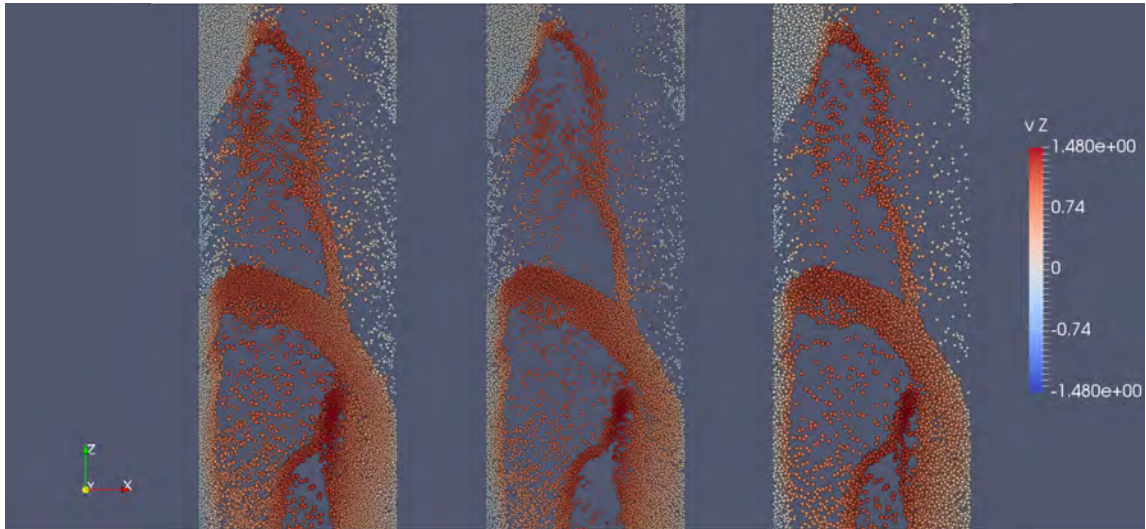
Fig. 5.7 Snapshots of cluster patterns. Left to right: total particles; small particles; large particles.

Effect of scaling mapping conditions (K = 3)

To quantitatively discuss the effect of scaling mapping conditions on the cluster characteristic of the binary system, the cluster solids volume fraction profiles are shown in Figure 5.8. The mean solids holdup of one cluster is calculated from the following expression:

$$\varphi_{cluster} = \frac{\sum \varphi_s}{\sum N_{cells,occupied}} \qquad (5.8)$$

From Figure 5.8 it can be seen that a similar tendency for clustering is found under all conditions, with more clusters being formed close to the walls in comparison with the core region of the riser. Furthermore, it can be observed that a similar range of cluster solids volume fraction is found under different scaling mapping conditions except for condition b. Under condition b, the cluster solids holdups are relatively small and are extending more towards the center of the bed. This reveals that the ratio of grid size and particle diameter plays an important role on cluster solids volume fraction profiles of the binary system. Therefore, the analysis of the cluster profiles under condition b will be mainly discussed in the following subsection.

In Figure 5.9, the profiles of cluster velocity under different scaling mapping conditions are presented. As can be seen, the symmetric core-annulus distribution is displayed under all scaling mapping conditions. The clusters located close to the walls are mostly moving downwards while mostly upwards flowing clusters are found in the core region. This also matches with the observations from Figure 5.7. With condition b, the cluster velocity profiles
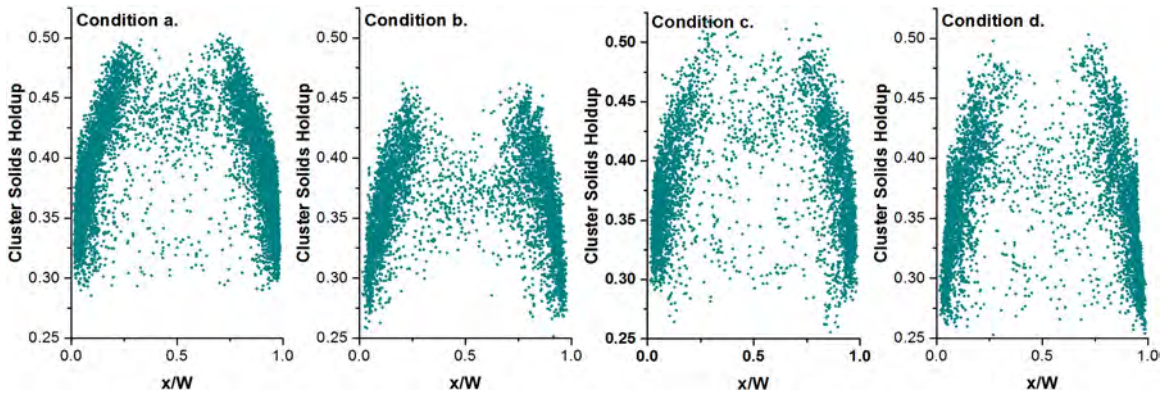
Fig. 5.8 Cluster solids holdup under four scaling mapping conditions. (K = 3)

are relatively low in comparison with the other conditions. It follows that for this binary system, the scaling of the ratio of grid size and particle diameter (condition b) has a significant influence on the cluster motion, both in terms of their velocity as well as their holdup.
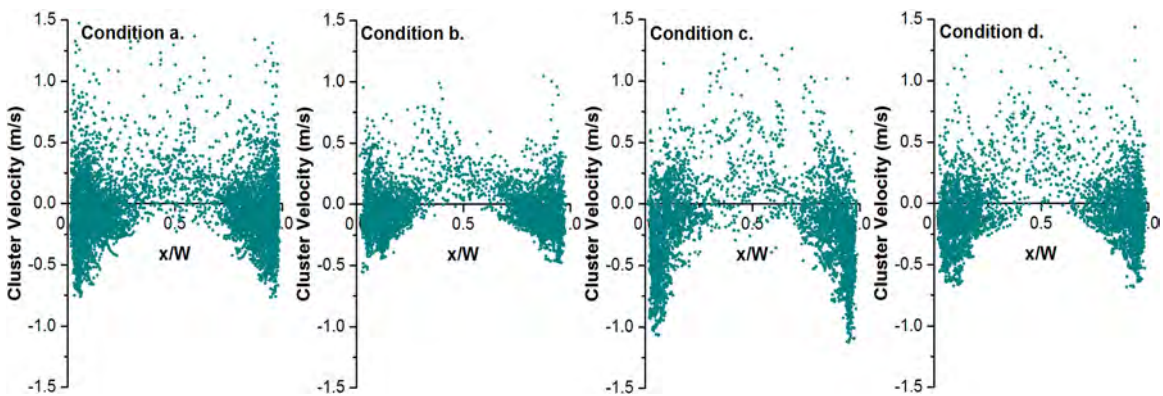
Fig. 5.9 Cluster velocity under four scaling mapping conditions. (K = 3)

Effect of scaling factors (Condition b: scaled grid.)

As mentioned in section 5.4.2, for K = 1 which had run for 5.89 s , the solids volume fraction profile at higher positions of the riser had not reached the steady state. Since the cluster formation at higher elevations would be influenced significantly the analysis of cluster-related profiles under three scaling factor conditions, except K = 1, will be discussed in this subsection.

The profiles of cluster solids holdup versus the cluster centroid horizontal position are plotted in Figure 5.10. For the different scaling factors, a similar behaviour is observed in the region close to the walls where more clusters reside that are denser than the ones present in the center of the riser. This matches the observations from the animations of the volume

fraction of the overall riser, where there are more clusters formed close to the walls than in the core region. A similar behaviour can be inferred from Figure 5.2. For K = 3, the solids holdup of clusters becomes relatively low in comparison with its counterparts obtained from the other two cases. This suggests that there is a critical threshold for the formation or detection of clusters for larger scaling factors, which needs to be further investigated.
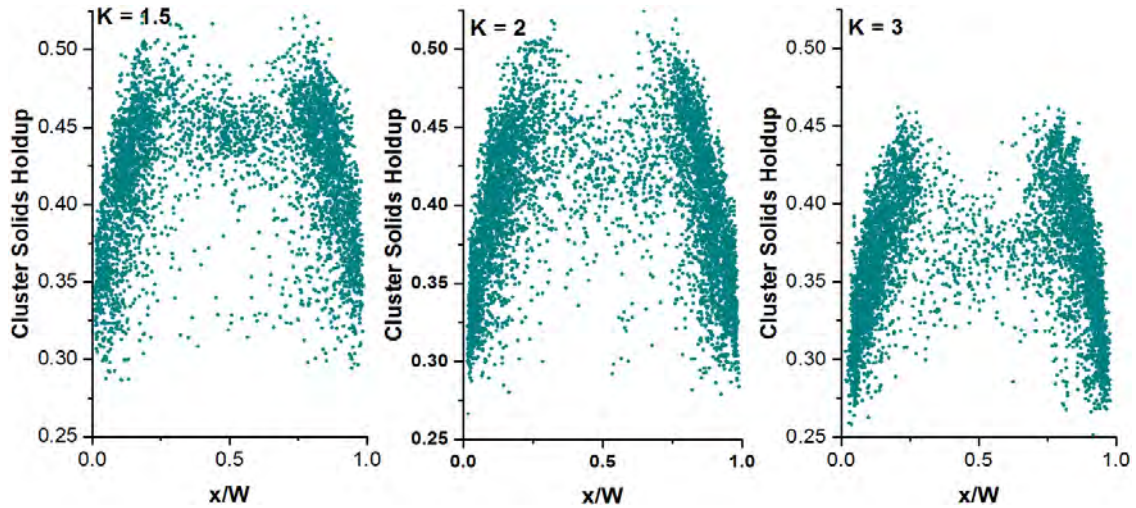
Fig. 5.10 Cluster solids holdup under three scaling factor conditions. (Condition b)

In Figure 5.11, the profiles of cluster velocity of the binary system for three scaling factor conditions are presented. It is noted that by employing different scaling factors, the cluster velocity is well predicted where in addition a symmetric distribution is found which matches the so-called core-annulus flow pattern in the binary system. At lower scaling factors, the distribution of the cluster velocity in the horizontal direction is more uniform than for its counterpart with K = 3. At higher values of K most of the clusters are located close to the riser walls.
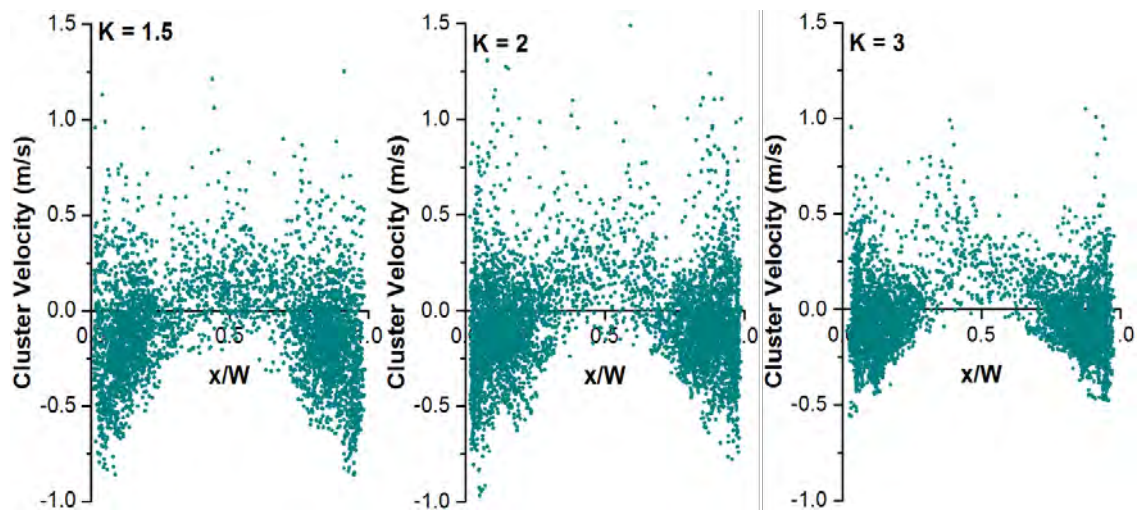
Fig. 5.11 Cluster velocity under three scaling factor conditions. (Condition b)

5.5   Conclusions and recommendations

In this work, the scaling method as described in chapter 4 has been applied to a binary gas-solid two phase flow. Four different scaling conditions were investigated by performing a series of simulations of a pseudo-2D circulating fluidized bed riser reactor. Scaling the properties of both the gas and solid phase was undertaken. Moreover, the ratio of the grid size and particle diameter and the ratio of riser depth and particle diameter were scaled as well for the binary system, leading to four different scaling/mapping conditions. The effect of the scaling method, the scaled grid size and the scaled riser depth on the hydrodynamics and cluster phenomena of the binary system have been quantified.

To assess the performance of the scaling method for a binary system, the simulated particle velocity profiles and solids volume fraction profiles were compared with experimental data reported in literature. Firstly, the distribution of solids volume fraction profiles of the binary system in the whole riser were compared for all four scaling mapping conditions. Both the simulation results and experimental data display a decaying solids volume fraction . In the horizontal direction there are relatively more particles located close to the walls in comparison with the center region of the riser, in accordance with the core-annular flow structure reported in literature. Secondly, at three axial locations the cross-sectional particle velocity and solids volume fraction distributions of two types of particles under different scaling mapping conditions were presented separately to quantify the impact of ratio of grid size and particle diameter and ratio of riser depth and particle diameter on flow pattern evolution. Along the horizontal direction both in the simulation results and experimental data, the typical U-shaped distributions are observed of the time-averaged solids volume fraction, whilst up-flow in the center region and down-flow close to the walls are found for the time-averaged particle velocity profiles. Out of the four scaling mapping conditions, condition b shows a better performance in comparison with the experimental results. Furthermore, the effect of scaling factors on the hydrodynamic behavior of the binary system in the riser were investigated by comparison of the experimental and numerical results. At higher axial positions, the particle velocity distribution of large particles becomes relatively flat, while for small particles the obtained simulation results revealed that the velocity distribution in the core region becomes narrower in comparison with the experimental data. We conclude that the adapted scaling method for the binary system could describe the gas-particle flow characteristics reasonably well.

Finally, the effects of scaling conditions and scaling factors on cluster characteristics of the binary system such as cluster volume fraction, cluster velocity were studied. Due to the vigorous solids mixing of the two types of particles in the binary system, both types of particles are present in the clusters. The analysis of cluster profiles reported in this work were

therefore focused on the overall cluster instead of individual clusters. The applied scaling conditions produce similar trends in both the cluster velocity and cluster volume fraction profiles. It is noted that under scaling condition b the distribution of cluster characteristics is less pronounced, both in terms of velocity as cluster holdup. Thus, the ratio between grid size and particle diameter plays an important role on cluster characteristics of the binary system and should be discussed more extensively in the future work. The distribution of the cluster holdup and velocity profiles could be well predicted by different scaling factor, whereas under higher scaling factor conditions there are less clusters formed in the center of the riser. To simplify the analysis a binary solids system was chosen here. The extension of this study to polydisperse particulate systems is suggested including the quantification of the mass transfer characteristics.

Chapter 6

Conclusions

Conclusions

In this thesis a numerical study of dense bubbling gas-fluidized beds as well as circulating gas-fluidized bed risers has been carried out. For the accurate representation of both particle-particle as well as particle-fluid interaction the combined CFD-DEM approach was adopted.

Dense bubbling gas-fluidized beds

For the bubbling fluidized bed simulations the heat liberation due to an exothermic reaction was mimicked by including a constant heat source term in the thermal energy equation of the particulate phase. As a first step the implementation of the heat source term was successfully verified by comparing the simulation results with analytical solutions and numerical results obtained from an independent one-dimensional model for transient heat transfer in a fixed bed. Following this verification step the 3D CFD-DEM model was used to study the influence of the superficial gas velocity and the bed aspect ratio on the hydrodynamics and thermal behavior of a pseudo-2D bubbling gas-fluidized bed. It was found that the particles are better mixed when the superficial gas velocity and the bed aspect ratio increase leading to a more isothermal bed. Furthermore, in an attempt to represent catalyst deactivation and the associated reduction in the rate of heat production, systems with mixtures of particles with heat source ("active particles") and without heat source (inactive particles") were studied. The simulation results revealed that the heat transfer from the active to the inactive particles via the interstitial gas phase proved to be quite effective due to the very high volumetric gas-particle heat transfer coefficients typically prevailing in dense gas-fluidized beds.

Circulating gas-fluidized bed risers

To enable simulations of the hydrodynamics of circulating fluidized bed risers at relatively low computational cost, a scaling method was developed and carefully validated by comparing the computational results with experimental data. The influence of the solids inlet and outlet configurations and the superficial gas velocity on the flow structure was investigated computationally for a pseudo-2D riser using 0.85 mm glass beads. Specifically a comparison was made between results obtained from two different CFD-DEM codes, namely an in-house developed code and the open-source code OpenFoam-CFDEM-LIGGHTS, and experimental data reported by Carlos Varas et al. (2017). In the analysis the obtained cross-sectional profiles of the solids volume fraction and solids mass flux were examined at three axial locations low in the riser and three axial locations near the riser exit. The analysis revealed that the time-averaged solids volume fraction is significantly higher at the three low axial positions. The effect of the inlet (side inlet or bottom inlet) on the lateral profiles of solids volume fraction and solids mass flux near the exit is negligible. In addition it was found

that the profiles of these quantities strongly depend on the superficial gas velocity. At low superficial velocities the flow pattern is characterized by strong solids up-flow in the core region and strong solids down-flow close to the riser walls. In case a lateral outlet with rough walls is used the solids mass flux distribution becomes asymmetric which becomes more pronounced with increasing superficial gas velocity and higher axial position in the riser. An important feature of the complex flow structure prevailing in CFB risers are clusters which were therefore investigated in more detail. Analysis of both experimental and simulation results revealed that most of the clusters reside near the walls which is referred to as the core-annulus flow structure. The cluster frequency is significantly influenced by the superficial gas velocity with a more symmetrical distribution in case particles are introduced at the bottom of the riser. This underlines the importance of the solids inlet configuration which should receive more attention in future work.

To achieve both accuracy and efficiency in CFD-DEM simulations of systems such as (large scale) CFB risers, a scaling method was developed and validated as well in this work. The equations of motion for the particles as well as the models for particle-fluid interaction, particle-particle and particle-wall encounters were scaled such that a similar flow behavior results while the particle number and hence the computational time significantly decreases. Thus, seven gas and particle properties were scaled including the particle diameter, the gas viscosity, gravitational acceleration, normal and tangential spring stiffness. Besides scaling of the gas and particle properties, the ratio of the particle diameter and Eulerian grid size as well as the ratio of riser depth and particle diameter were scaled to fully investigate the impact of the scaling method on the riser hydrodynamics. Extensive simulations of pseudo-2D riser flow were performed and the computational results were compared with experimental data to quantify the impact of the scaling method on the profiles of solids volume fraction, solids mass flux as well as cluster characteristics. The applied scaling methods could well capture the typical U-shaped solids volume fraction profiles with particle up-flow in the core region and pronounced down-flow close to the riser walls. In addition, when scaling of the ratio of the particle diameter and the Eulerian grid size was applied, the time-averaged cross-sectional profiles of solids volume fraction and solids mass flux matched quite well for the chosen scaling factors. To complete the analysis, also the impact of the scaling conditions on the cluster characteristics was studied revealing that the ratio of the particle volume and volume of the Eulerian cells should be kept constant to correctly capture the key cluster features.

Following the assessment of the accuracy and efficiency of the developed scaling method for a laboratory scale riser, the method was applied to a binary system. The performance of the scaling method was investigated by performing a series of simulations of a pseudo-2D riser containing two types of particles. The simulation results were compared with

experimental data reported by Mathiesen et al. (2000). The effect of scaling of the properties of the gas and solid phase, the ratio of the grid size and particle diameter and the ratio of riser depth and particle diameter were all studied. The effect of the scaling conditions on the flow structure and cluster characteristics of the binary particle system were also quantified. Firstly, the profiles of particle velocity and solids volume fraction of the two types of particles were analyzed separately for the applied scaling conditions. It was found that for both types of particles the solids volume fraction decreases in the vertical direction of the riser whilst in the horizontal direction the well-known U-shaped distribution was obtained. Typically up-flow in the center region and down-flow close to the left and right walls was observed where the particle velocity decreased in the axial direction in accordance with the expectations. When the riser depth was scaled a flatter distribution was found in comparison with the case where the grid size was scaled for both types of particles. This finding indicates that scaling of the grid size affects the solids motion of binary particle systems in CFB risers. Finally the influence of scaling conditions on cluster characteristics of binary systems was assessed. Each detected cluster consisted of both types of particles due to the vigorous solids mixing. Consequently, the cluster analysis was limited to the overall cluster behavior. Cluster velocities and solids volume fraction profiles were affected by the scaling conditions but could be well-predicted by using different scaling factors. These findings demonstrate the performance of the new scaling method for binary systems as well as the importance of the (scaling) ratio of grid size and particle diameter. It is suggested that in future studies the work reported in this thesis is extended to riser flows with coupled mass and heat transfer in the presence of catalytic reactions.

References

W. P. Adamczyk, G. Węcel, M. Klajny, P. Kozołub, A. Klimanek, and R. A. Białecki. Modeling of particle transport and combustion phenomena in a large-scale circulating fluidized bed boiler using a hybrid euler–lagrange approach. *Particuology*, 16:29–40, 2014.

N. Almohammed, F. Alobaid, M. Breuer, and B. Epple. A comparative study on the influence of the gas flow rate on the hydrodynamics of a gas–solid spouted fluidized bed using euler–euler and euler–lagrange/dem models. *Powder technology*, 264:343–364, 2014.

A. Almuttahar and F. Taghipour. Computational fluid dynamics of high density circulating fluidized bed riser: study of modeling parameters. *Powder Technology*, 185(1):11–23, 2008.

F. Alobaid, J. Ströhle, and B. Epple. Extended cfd/dem model for the simulation of circulating fluidized bed. *Advanced Powder Technology*, 24(1):403–415, 2013.

F. Alobaid, N. Baraki, and B. Epple. Investigation into improving the efficiency and accuracy of cfd/dem simulations. *Particuology*, 16:41–53, 2014.

M. J. Andrews and P. J. O'Rourke. The multiphase particle-in-cell (mp-pic) method for dense particulate flows. *International Journal of Multiphase Flow*, 22(2):379–402, 1996.

A. Bakker, G. Gilmer, M. Grabow, and K. Thompson. A special purpose computer for molecular dynamics calculations. *Journal of Computational Physics*, 90(2):313–335, 1990.

P. Basu and P. K. Nag. An investigation into heat transfer in circulating fluidized beds. *Int. J. of heat and Mass Transfer*, 30(11):2399–2409, 1987.

R. Beetstra, M. A. Van der Hoef, and J. A. M. Kuipers. Numerical study of segregation using a new drag force correlation for polydisperse systems derived from lattice-boltzmann simulations. *Chemical Engineering Science*, 62(1):246–255, 2007.

S. Benyahia. Fine-grid simulations of gas-solids flow in a circulating fluidized bed. *AIChE Journal*, 58(NETL-PUB-2), 2012.

A. W. Bhutto, A. A. Bazmi, and G. Zahedi. Underground coal gasification: From fundamentals to applications. *Progress in Energy and Combustion Science*, 39(1):189–214, 2013.

References

C. Bierwisch, T. Kraft, H. Riedel, and M. Moseler. Three-dimensional discrete element models for the granular statics and dynamics of powders in cavity filling. *Journal of the Mechanics and Physics of Solids*, 57(1):10–31, 2009.

R. Bird, W. Stewart, and E. Lightfoot. *Transport Phenomena*. John Wiley & Sons, 2001.

L. Bolton and J. Davidson. Recirculation of particles in fast fluidized risers. In *Circulating Fluidized Bed Technology*, pages 139–146. Elsevier, 1988.

V. A. Borodulya, V. L. Ganzha, Y. S. Teplitskii, and Y. G. Epanov. Heat transfer in fluidized beds. *Journal of engineering physics*, 49(4):1197–1202, 1985.

T. Brosh, H. Kalman, and A. Levy. Accelerating cfd–dem simulation of processes with wide particle size distributions. *Particuology*, 12:113–121, 2014.

A. Carlos Varas, E. Peters, N. Deen, and J. Kuipers. Solids volume fraction measurements on riser flow using a temporal-histogram based dia method. *AIChE Journal*, 62(8):2681–2698, 2016.

J. Chen and X. Lu. Progress of petroleum coke combusting in circulating fluidized bed boilers—a review and future perspectives. *Resources, conservation and recycling*, 49(3): 203–216, 2007.

L. Chen, D. Kost, and W. A. Dick. Petroleum coke circulating fluidized bed combustion product effects on soil and water quality. *Soil science*, 175(6):270–277, 2010.

P. W. Cleary, R. Morrisson, and S. Morrell. Comparison of dem and experiment for a scale model sag mill. *International Journal of Mineral Processing*, 68(1-4):129–165, 2003.

R. Cocco, F. Shaffer, R. Hays, S. R. Karri, and T. Knowlton. Particle clusters in and above fluidized beds. *Powder Technology*, 203(1):3–11, 2010.

R. Conn. Laboratory techniques for evaluating ash agglomeration potential in petroleum coke fired circulating fluidized bed combustors. *Fuel processing technology*, 44(1-3): 95–103, 1995.

J. Cui, L. Duan, Y. Jiang, C. Zhao, and E. J. Anthony. Migration and emission of mercury from circulating fluidized bed boilers co-firing petroleum coke and coal. *Fuel*, 215: 638–646, 2018.

P. A. Cundall and O. D. Strack. A discrete numerical model for granular assemblies. *geotechnique*, 29(1):47–65, 1979.

J. De Wilde, G. Heynderickx, G. Marin, et al. Experimental study of inlet phenomena of 35 inclined non-aerated and aerated y-inlets in a dilute cold-flow riser. *Chemical engineering science*, 62(1-2):339–355, 2007.

N. G. Deen, M. Van Sint Annaland, M. A. Van der Hoef, and J. A. M. Kuipers. Review of discrete particle modelling of fluidized beds. *Chemical Engineering Science*, 62(1-2): 28–44, 2007.

A. Džiugys and B. Peters. An approach to simulate the motion of spherical and non-spherical fuel particles in combustion chambers. *Granular matter*, 3(4):231–266, 2001.

S. Ergun. Fluid flow through packed columns. *Chemical Engineering Progress*, 48:89–94, 1952.

N. Firuzian, R. Sotudeh-Gharebagh, and N. Mostoufi. Experimental investigation of cluster properties in dense gas–solid fluidized beds of different diameters. *Particuology*, 16:69–74, 2014.

F. Fleissner and P. Eberhard. Parallel load-balanced simulation for short-range interaction particle methods with hierarchical particle grouping based on orthogonal recursive bisection. *International Journal for Numerical Methods in Engineering*, 74(4):531–553, 2008.

X. Gao, T. Li, and W. A. Rogers. Assessment of mesoscale solid stress in coarse-grid tfm simulation of geldart a particles in all fluidization regimes. *AIChE Journal*, 64(10): 3565–3581, 2018.

D. Geldart and M. Rhodes. From minimum fluidization to pneumatic transport-a critical review of the hydrodynamics. *Circulating fluidized bed technology*, pages 21–31, 1986.

D. Gidaspow. High production circulating fluidized bed polymerization reactors. *Powder Technology*, 357:108–116, 2019.

D. Gidaspow and L. Huilin. Equation of state and radial distribution functions of fcc particles in a cfb. *AIChE Journal*, 44(2):279–293, 1998.

D. Gidaspow, J. Jung, and R. K. Singh. Hydrodynamics of fluidization using kinetic theory: an emerging paradigm: 2002 flour-daniel lecture. *Powder Technology*, 148(2-3):123–141, 2004.

M. Girardi, S. Radl, and S. Sundaresan. Simulating wet gas–solid fluidized beds using coarse-grid cfd-dem. *Chemical Engineering Science*, 144:224–238, 2016.

L. Glicksman, M. Hyre, and P. Farrell. Dynamic similarity in fluidization. *International Journal of Multiphase Flow*, 20:331–386, 1994.

A. Gobin, H. Neau, O. Simonin, J.-R. Llinas, V. Reiling, and J.-L. Sélo. Fluid dynamic numerical simulation of a gas phase polymerization reactor. *International journal for numerical methods in fluids*, 43(10-11):1199–1220, 2003.

A. Gómez-Barea and B. Leckner. Modeling of biomass gasification in fluidized bed. *Progress in Energy and Combustion Science*, 36(4):444–509, 2010.

C. Goniva, C. Kloss, N. G. Deen, J. A. Kuipers, and S. Pirker. Influence of rolling friction on single spout fluidized bed simulation. *Particuology*, 10(5):582–591, 2012.

J. Grace and G. Sun. Influence of particle size distribution on the performance of fluidized bed reactors. *The Canadian Journal of Chemical Engineering*, 69(5):1126–1134, 1991.

C. Guenther and R. Breault. Wavelet analysis to characterize cluster dynamics in a circulating fluidized bed. *Powder technology*, 173(3):163–173, 2007.

D. J. Gunn. Transfer of heat or mass to particles in fixed and fluidized beds. *Int. J. Heat Mass Transf*, 21:467–476, 1978.

References

E.-U. Hartge, D. Rensner, and J. Werther. Solids concentration and velocity patterns in circulating fluidized beds. In *Circulating fluidized bed technology*, pages 165–180. Elsevier, 1988.

G. Heynderickx, J. De Wilde, G. Marin, et al. Experimental and computational study of t-and l-outlet effects in dilute riser flow. *Chemical engineering science*, 66(21):5024–5044, 2011.

K. Hong, S. Chen, W. Wang, and J. Li. Fine-grid two-fluid modeling of fluidization of geldart a particles. *Powder Technology*, 296:2–16, 2016.

B. Hoomans, J. Kuipers, and W. P. M. van Swaaij. Granular dynamics simulation of segregation phenomena in bubbling gas-fluidised beds. *Powder Technology*, 109(1-3): 41–48, 2000.

B. P. B. Hoomans, J. A. M. Kuipers, W. J. Briels, and W. P. M. van Swaaij. Discrete particle simulation of bubble and slug formation in a two-dimensional gas-fluidised bed: A hard-sphere approach. *Chemical Engineering Science*, 51(1):99–118, 1996.

M. Horio and H. Kuroki. Three-dimensional flow visualization of dilutely dispersed solids in bubbling and circulating fluidized beds. *Chemical Engineering Science*, 49(15):2413–2421, 1994.

L. Hua, J. Wang, and J. Li. Cfd simulation of solids residence time distribution in a cfb riser. *Chemical Engineering Science*, 117:264–282, 2014.

T. Kadyrov, F. Li, and W. Wang. Impacts of solid stress model on mp-pic simulation of a cfb riser with emms drag. *Powder Technology*, 354:517–528, 2019.

M. Khan, M. Hussain, Z. Mansourpour, N. Mostoufi, N. Ghasem, and E. Abdullah. Cfd simulation of fluidized bed reactors for polyolefin production–a review. *Journal of Industrial and Engineering Chemistry*, 20(6):3919–3946, 2014.

Y. J. Kim, J. M. Lee, and S. D. Kim. Coal gasification characteristics in an internally circulating fluidized bed with draught tube. *Fuel*, 76(11):1067–1073, 1997.

A. Klimanek, W. Adamczyk, A. Katelbach-Woźniak, G. Węcel, and A. Szlęk. Towards a hybrid eulerian–lagrangian cfd modeling of coal gasification in a circulating fluidized bed reactor. *Fuel*, 152:131–137, 2015.

C. Kloss, C. Goniva, G. Aichinger, and S. Pirker. Comprehensive dem-dpm-cfd simulations-model synthesis, experimental validation and scalability. In *Proceedings of the seventh international conference on CFD in the minerals and process industries, CSIRO, Melbourne, Australia*, pages 9–11, 2009.

S. Kuang, K. Li, S. Shrestha, and A. Yu. Discrete particle simulation of heterogeneous gas-solid flows in riser and downer reactors. *Powder Technology*, 375:221–232, 2020.

J. A. M. Kuipers and W. P. M. van Swaaij. Computational fluid dynamics applied to chemical reaction engineering. *In J. Wei, editor, Advances in Chemical Engineering*, pages 227–328, 1998.

D. Kunii and O. Levenspiel. Butterworth-heinemann series in chemical engineering. butterworth-heinemann limited. *Fluidization engineering*, 1991a.

D. Kunii and O. Levenspiel. *Fluidization engineering*. Butterworth-Heinemann, 1991b.

K. Kuwagi and M. Horio. A numerical study on agglomerate formation in a fluidized bed of fine cohesive particles. *Chemical Engineering Science*, 57(22-23):4737–4744, 2002.

U. Lackermeier, C. Rudnick, J. Werther, A. Bredebusch, and H. Burkhardt. Visualization of flow structures inside a circulating fluidized bed by means of laser sheet and image processing. *Powder Technology*, 114(1-3):71–83, 2001.

A. A. Lappas, D. K. Iatridis, E. P. Kopalidou, and I. A. Vasalos. Influence of riser length of a fluid catalytic cracking pilot plant on catalyst residence time and product selectivity. *Industrial & Engineering Chemistry Research*, 56(45):12927–12939, 2017.

T. Li, J.-F. Dietiker, and L. Shadle. Comparison of full-loop and riser-only simulations for a pilot-scale circulating fluidized bed riser. *Chemical Engineering Science*, 120:10–21, 2014.

Z. Li, M. Van Sint Annaland, J. A. M. Kuipers, and N. G. Deen. Effect of superficial gas velocity on the particle temperature distribution in a fluidized bed with heat production. *Chemical Engineering Science*, 140:279–290, 2016.

T. Lichtenegger and S. Pirker. Cfd-dem modeling of strongly polydisperse particulate systems. *Powder Technology*, 325:698–711, 2018.

S. Limtrakul, A. Boonsrirat, and T. Vatanatham. Dem modeling and simulation of a catalytic gas-solid fluidized bed reactor: a spouted bed as a case study. *Chemical Engineering Science*, 59(22-23):5225–5231, 2004.

J. Link, W. Godlieb, P. Tripp, N. Deen, S. Heinrich, J. Kuipers, M. Schönherr, and M. Peglow. Comparison of fibre optical measurements and discrete element simulations for the study of granulation in a spout fluidized bed. *Powder technology*, 189(2):202–217, 2009.

A. Maknickas, A. Kačeniauskas, R. Kačianauskas, R. Balevičius, and A. Džiugys. Parallel dem software for simulation of granular media. *Informatica*, 17(2):207–224, 2006.

S. Manyele, J. Pärssinen, and J.-X. Zhu. Characterizing particle aggregates in a high-density and high-flux cfb riser. *Chemical Engineering Journal*, 88(1-3):151–161, 2002.

V. Mathiesen, T. Solberg, and B. H. Hjertager. An experimental and computational study of multiphase flow behavior in a circulating fluidized bed. *International Journal of Multiphase Flow*, 26(3):387–419, 2000.

C. C. Milioli, F. E. Milioli, W. Holloway, K. Agrawal, and S. Sundaresan. Filtered two-fluid models of fluidized gas-particle flows: new constitutive relations. *AIChE Journal*, 59(9): 3265–3275, 2013.

A. Miller and D. Gidaspow. Dense, vertical gas-solid flow in a pipe. *AIChE journal*, 38(11): 1801–1815, 1992.

References

A. J. Minchener. Coal gasification for advanced power generation. *Fuel*, 84(17):2222–2235, 2005.

M. Mokhtar, K. Kuwagi, T. Takami, H. Hirano, and M. Horio. Validation of the similar particle assembly (spa) model for the fluidization of geldart's group a and d particles. *AIChE journal*, 58(1):87–98, 2012.

L. Mu, K. Buist, J. Kuipers, and N. Deen. Scaling method of cfd-dem simulations for gas-solid flows in risers. *Chemical Engineering Science: X*, 6:100054, 2020.

A. Muhammad, N. Zhang, and W. Wang. Cfd simulations of a full-loop cfb reactor using coarse-grained eulerian–lagrangian dense discrete phase model: effects of modeling parameters. *Powder Technology*, 354:615–629, 2019.

J. Niewland, P. Huizenga, J. Kuipers, and W. P. M. van Swaaij. Hydrodynamic modelling of circulating fluidised beds. *Chemical engineering science*, 49(24):5803–5811, 1994.

A. Ozel, J. Kolehmainen, S. Radl, and S. Sundaresan. Fluid and particle coarsening of drag force for discrete-parcel approach. *Chemical engineering science*, 155:258–267, 2016.

A. Ozel, Y. Gu, C. C. Milioli, J. Kolehmainen, and S. Sundaresan. Towards filtered drag force model for non-cohesive and cohesive particle-gas flows. *Physics of Fluids*, 29(10): 103308, 2017.

T. O'Brien and M. Syamlal. Particle cluster effects in the numerical simulation of a circulating fluidized bed, 4th int. In *Conf. on CFB, Somerset, USA*, 1993.

P. J. O'Rourke and D. M. Snider. An improved collision damping time for mp-pic calculations of dense particle flows with applications to polydisperse sedimenting beds and colliding particle jets. *Chemical Engineering Science*, 65(22):6014–6028, 2010.

P. J. O'Rourke, P. P. Zhao, and D. Snider. A model for collisional exchange in gas/liquid/solid fluidized beds. *Chemical Engineering Science*, 64(8):1784–1797, 2009.

M. Pantzali, B. De Ceuster, G. Marin, and G. Heynderickx. Three-component particle velocity measurements in the bottom section of a riser. *International Journal of Multiphase Flow*, 72:145–154, 2015.

M. N. Pantzali, J. Marqués de Marino, G. B. Marin, and G. J. Heynderickx. Three-component solids velocity measurements in the outlet section of a riser. *AIChE Journal*, 62(10):3575–3584, 2016.

J.-F. Parmentier, O. Simonin, and O. Delsart. A functional subgrid drift velocity model for filtered drag prediction in dense fluidized bed. *AIChE Journal*, 58(4):1084–1098, 2012.

A. Passalacqua and R. Fox. Advanced continuum modelling of gas-particle flows beyond the hydrodynamic limit. *Applied Mathematical Modelling*, 35(4):1616–1627, 2011.

A. Passalacqua, R. Fox, R. Garg, and S. Subramaniam. A fully coupled quadrature-based moment method for dilute to moderately dilute fluid–particle flows. *Chemical Engineering Science*, 65(7):2267–2283, 2010.

N. Patankar and D. Joseph. Modeling and numerical simulation of particulate flows by the eulerian–lagrangian approach. *International journal of multiphase flow*, 27(10):1659–1684, 2001.

A. M. Patel, R. A. Cocco, and J. W. Chew. Key influence of clusters of geldart group b particles in a circulating fluidized bed riser. *Chemical Engineering Journal*, 413:127386, 2021.

G. S. Patience and J. Chaouki. Gas phase hydrodynamics in the riser of a circulating fluidized bed. *Chemical engineering science*, 48(18):3195–3205, 1993.

A. V. Patil, E. A. J. F. Peters, T. Kolkman, and J. A. M. Kuipers. Modeling bubble heat transfer in gas-solid fluidized beds using dem. *Chemical Engineering Science*, 105(0): 121–131, 2014.

S. Radl, C. Radeke, J. G. Khinast, and S. Sundaresan. Parcel-based approach for the simulation of gas-particle flows. In *8th International Conference on CFD in Oil & Gas, Metallurgical and Process Industries, Trondheim*, volume 23, pages 1084–1098, 2011.

S. Radl, M. Girardi, and S. Sundaresan. Effective drag law for parcel-based approaches–what can we learn from cfd-dem. In *European Congress on Computational Methods in Applied Sciences and Engineering (ECCOMAS 2012)*, pages 1225–1239, 2012.

D. Rapaport. Multi-million particle molecular dynamics: Ii. design considerations for distributed processing. *Computer Physics Communications*, 62(2-3):217–228, 1991.

T. A. B. Rashid, L.-T. Zhu, and Z.-H. Luo. Effect of granular properties on hydrodynamics in coarse-grid riser flow simulation of geldart a and b particles. *Powder Technology*, 359: 126–144, 2020.

M. Sakai and S. Koshizuka. Large-scale discrete element modeling in pneumatic conveying. *Chemical Engineering Science*, 64(3):533–539, 2009.

B. C. Schäfer, S. F. Quigley, and A. H. Chan. Acceleration of the discrete element method (dem) on a reconfigurable co-processor. *Computers & Structures*, 82(20-21):1707–1718, 2004.

S. Schneiderbauer and S. Pirker. Filtered and heterogeneity-based subgrid modifications for gas–solid drag and solid stresses in bubbling fluidized beds. *AIChE Journal*, 60(3): 839–854, 2014.

M. Schoen. Structure of a simple molecular dynamics fortran program optimized for cray vector processing computers. *Computer physics communications*, 52(2):175–185, 1989.

F. Shaffer, B. Gopalan, R. W. Breault, R. Cocco, S. R. Karri, R. Hays, and T. Knowlton. High speed imaging of particle flow fields in cfb risers. *Powder technology*, 242:86–99, 2013.

M. T. Shah, R. P. Utikar, V. K. Pareek, G. M. Evans, and J. B. Joshi. Computational fluid dynamic modelling of fcc riser: A review. *chemical engineering research and design*, 111: 403–448, 2016.

References

A. K. Sharma, K. Tuzla, J. Matsen, and J. C. Chen. Parametric effects of particle size and gas velocity on cluster characteristics in fast fluidized beds. *Powder Technology*, 111(1-2): 114–122, 2000.

D. M. Snider. An incompressible three-dimensional multiphase particle-in-cell model for dense particle flows. *Journal of computational physics*, 170(2):523–549, 2001.

C. Soong, K. Tuzla, and J. Chen. Identification of particle clusters in circulating fluidized bed. circulating fluidized bed technology iv, 1993.

S. Sundaresan. Role of hydrodynamics on chemical reactor performance. *Current Opinion in Chemical Engineering*, 2(3):325–330, 2013.

V. S. Sutkar, N. G. Deen, B. Mohan, V. Salikov, S. Antonyuk, S. Heinrich, and J. Kuipers. Numerical investigations of a pseudo-2d spout fluidized bed with draft plates using a scaled discrete particle model. *Chemical engineering science*, 104:790–807, 2013.

M. Syamlal and D. Gidaspow. Hydrodynamics of fluidization: prediction of wall to bed heat transfer coefficient. *AIChE J*, 31:127–135, 1985.

U. Trivedi, A. Bassi, and J.-X. J. Zhu. Continuous enzymatic polymerization of phenol in a liquid–solid circulating fluidized bed. *Powder technology*, 169(2):61–70, 2006.

Y. Tsuji, T. Kawaguchi, and T. Tanaka. Discrete particle simulation of two-dimensional fluidized bed. *Powder technology*, 77(1):79–87, 1993.

Y. P. Tsuo and D. Gidaspow. Computation of flow patterns in circulating fluidized beds. *AIChE Journal*, 36(6):885–896, 1990.

J. A. Valenzuela and L. R. Glicksman. An experimental study of solids mixing in a freely bubbling two-dimensional fluidized bed. *Powder Technology*, 38(1):63–72, 1984.

A. G. van der Ham, W. Prins, and W. P. M. van Swaaij. A small-scale regularly packed circulating fluidized bed: Part ii: Mass transfer. *Powder technology*, 79(1):29–41, 1994.

M. A. Van der Hoef, M. Van Sint Annaland, N. G. Deen, and J. A. M. Kuipers. Numerical simulation of dense gas-solid fluidized beds: a multiscale modeling strategy. *Annual Review of Fluid Mechanics*, 40:47–70, 2008.

E. Van der Meer, R. Thorpe, and J. Davidson. Flow patterns in the square cross-section riser of a circulating fluidised bed and the effect of riser exit design. *Chemical Engineering Science*, 55(19):4079–4099, 2000.

M. Van Sint Annaland, N. G. Deen, and J. A. M. Kuipers. Numerical simulation of gas–liquid–solid flows using a combined front tracking and discrete particle method. *Chemical Engineering Science*, 60:6188–6198, 2005.

A. C. Varas, E. Peters, and J. Kuipers. Experimental study of full field riser hydrodynamics by piv/dia coupling. *Powder Technology*, 313:402–416, 2017.

J. Wang, M. A. van der Hoef, and J. Kuipers. Why the two-fluid model fails to predict the bed expansion characteristics of geldart a particles in gas-fluidized beds: a tentative answer. *Chemical Engineering Science*, 64(3):622–625, 2009.

124

S. Wang, K. Luo, C. Hu, and J. Fan. Cfd-dem study of the effect of cyclone arrangements on the gas-solid flow dynamics in the full-loop circulating fluidized bed. *Chemical Engineering Science*, 172:199–215, 2017.

X. Wei, J. Yang, and J. Zhu. Experimental analysis of phase segregation in gas-solid circulating fluidized bed riser with direct image calibration. *Chemical Engineering Journal*, 379:122301, 2020.

C. Y. Wen and Y. H. Yu. A generalized method for predicting the minimum fluidization velocity. *AIChE J*, 12:610–612, 1966.

Y. Wu, D. Liu, J. Hu, J. Ma, and X. Chen. Comparative study of two fluid model and dense discrete phase model for simulations of gas–solid hydrodynamics in circulating fluidized beds. *Particuology*, 55:108–117, 2021.

J. Yang and J. Zhu. A novel method based on image processing to visualize clusters in a rectangular circulating fluidized bed riser. *Powder technology*, 254:407–415, 2014.

Z. Yang, Y. Zhang, A. Oloruntoba, and J. Yue. Mp-pic simulation of the effects of spent catalyst distribution and horizontal baffle in an industrial fcc regenerator. part i: Effects on hydrodynamics. *Chemical Engineering Journal*, 412:128634, 2021.

C. E. Yeo and S. W. Kim. Axial holdup distributions of fcc catalysts in a small-diameter riser with abrupt exit in circulating fluidized bed. *Advanced Powder Technology*, 31(5): 1946–1956, 2020.

J. Yerushalmi. High velocity fluidization. *Fluidization*, pages 225–289, 1985.

H. Zhou, G. Flamant, and D. Gauthier. Dem-les of coal combustion in a bubbling fluidized bed. part i: gas-particle turbulent flow structure. *Chemical Engineering Science*, 59(20): 4193–4203, 2004.

Z. Y. Zhou, A. B. Yu, and P. Zulli. Particle scale study of heat transfer in packed and bubbling fluidized beds. *AIChE J.*, 55(4):868–884, 2009.

Z. Y. Zhou, A. B. Yu, and P. Zulli. A new computational method for studying heat transfer in fluid bed reactors. *Powder Technology*, 197:102–110, 2010.

L.-T. Zhu, Y.-N. Yang, D.-T. Pan, and Z.-H. Luo. Capability assessment of coarse-grid simulation of gas-particle riser flow using sub-grid drag closures. *Chemical Engineering Science*, 213:115410, 2020.

List of publications

Journal papers

- L. Mu, K.A. Buist, J.A.M. Kuipers, N.G. Deen, Hydrodynamic and heat transfer study of a fluidized bed by discrete particle simulations. Processes, 8:463, 2020.

- L. Mu, K.A. Buist, J.A.M. Kuipers, N.G. Deen, Scaling Method of CFD-DEM Simulations for Gas-Solid Flows in Risers. Chemical Engineering Science: X, 6:100054, 2020.

- L. Mu, K.A. Buist, J.A.M. Kuipers, N.G. Deen, CFD-DEM Simulations of Riser Geometry Effect and Cluster Phenomena. Advanced Powder Technology, 32:3234-3247, 2021.

- L. Mu, K.A. Buist, J.A.M. Kuipers, N.G. Deen, Scaling Method for CFD-DEM Simulations of Binary Particle System. In preparation.

Conference

- L. Mu, J.A.M. Kuipers, N.G. Deen. (2015) Hydrodynamic Study Of Heat Transfer in a Fluidized Bed by Discrete Particle Simulations. Fluidization XV conference, Quebec, Canada.

Acknowledgements

In October 2014, I started my PhD project at Multiphase Reactors Group in the Department of Chemical Engineering and Chemistry at Eindhoven University of Technology. And now this dissertation presents a milestone in my career. I would like to express my sincere appreciation to many individuals who have made this possible: my family, friends, colleagues and supervisors.

First of all, I would like to thank Hans for offering me the opportunity to work on this project in SMR group. For the past years, he offered his guidance and support without doubt. His kindness, encouragements and comments on my work eased my hesitations and motived me to move forward. Our discussions always have been very insightful and instructive. They helped me very much and have been the bright lighthouse during my project. This work would not have been possible without my two daily supervisors either. Niels, you helped me a lot and generously offered me studying and presenting opportunities. Your unconditional believes in me helped me believe in myself. Your positive life attitude and highly efficient working style are life lessons to me. Kay, it's my lucky to have you joined my project. I express my heartfelt appreciation for you being my daily supervisor. Your professional advices and prompt help always solved my doubts. Your sensitive and patient understanding saved me many times. I couldn't imagine how I could have reach at this final stage of my project, without your participation.

I also sincerely acknowledge the financial support to this project from the Netherlands Center for Multiscale Catalytic Energy Conversion (MCEC). Also I would like to express my gratitude to all the committee members for their valuable time in reviewing this thesis and participating in the defense ceremony. My gratitude also goes to our secretaries Ada and Judith. Especially, I would like to thank Ada for all her work on administrative matters which provided a great support for my work and dealing with the extension of my contracts.

Of course, I would like to thank my SMR colleagues, with whom I shared many positive experiences: Frank, Johan, Maike, Saurish, Rohit, Ivo, Larry, Mohammed, Mariet, Paolo, Max, Solomon, Kai, Luuk, Ramon, Shauvik, Vinay, Giulia, Krushna, Vikrant, Panda, Merve. Special thanks to Alvaro, who introduced me to the complex setup and helped me understand-

Acknowledgements

ing its performance. My special gratitude goes to my paranymphs, Cristina and Morteza, for assisting me on the thesis printing and the organization of the defense ceremony. Espically for Morteza, thank you for being so kind to design the cover of my thesis which really saved me, and help me to remote control my workstation in many times. Besides that, I would like to give my special gratitude to my Chinese colleagues and their families: Yupeng, his wife and their beautiful daughter Xixi, Yali and Yuk Man, Lizzy, Lei, Dang, Jiangtao, Ningning, Gaopan and his wife, Wendy, Tianwei and Kun. There are lots of good memories of having lunch together in the weekdays and gathering in the weekends and holidays, making Chinese food or having group travels.

I also would like to thank my dear friends outside this group. One of my closest friends, Jing Yang have had great support to me when I needed it the most. I really admire your steady state of mind and I will take your lessons with me for the rest of my life. Yang Zhou, twenty-one years ago when we met the first time in the queue, I didn't imagine that would be the starting moment of my most important friendship. Thank you for always by my side even knowing that part of me which I'm not that fond of and keeping telling me it is and will be ok. I would also like to thank Xiaoping Qiu, who never get tired of offering his professional advices, helps and solutions to me when I need. Xiaojing, Haijing, Xiaoxiao and Jingchao, my friends and neighbors, with your company living in Aurora feels more like home.

Most importantly, I would like to take this opportunity to give my thanks and love to my family. 妈妈，谢谢您对我无条件的鼓励、支持、包容和爱，有您做我最坚强的后盾、鞭策我前进，我才能拥有现在这样的人生，有您做我的妈妈是我一生幸运。弟弟，谢谢你对姐姐的关心和照顾，你的陪伴支撑着我在人生路上一直前行。还要谢谢阿姨、舅舅、大伯、姑姑、表兄弟姐妹们，有你们的陪伴我感到很幸福，谢谢你们给我的陪伴和爱。妈妈、爸爸，我爱你们。

Lijing Mu
March, 2022
Beijing, China

130

Curriculum vitae

Lijing Mu was born October 31st, 1989 in Shenzhou, China. She grew up and completed her primary and high school in Shenzhou city. After that, she decided to study Automation at Beijing Technology and Business University in Beijing, China. During her studies, she also had a rich experience of various activities, such as serving in the Student Union, visiting industries and companies. In June 2011 she graduated under supervision of Professor Wang Xiaoyi on the Evaluation of Water Bloom and Quality Group. In the same year, she started her chemical engineering master program in the Institute of Process Engineering, Chinese Academy of Sciences. With the guidance of Professor Wang Wei, she worked on her master dissertation entitled "The Influence of Inlet and Outlet Geometry on Flow and Mass Transfer Behaviour of Circulating Fluidized Beds" in Energy Minimization Multi-Scale Group. The simulation results of this work were published as her first journal paper. In June 2014, she obtained her master degree of Chemical Engineering. Later on, she joined the Multiscale Reactors Group in October, 2014 to start a PhD project under the supervision of Prof. dr.ir. J.A.M. Kuipers, Prof. dr.ir. N.G. Deen and dr.ir. K.A. Buist. The results of this research are presented in this dissertation.